

REGIONE AUTONOMA DELLA SARDEGNA


Universitá degli Studi di Cagliari
Dottorato di Ricerca in Fisica
Ciclo XXVI

Dust Modeling and Evolutionary Implications

Settore scientifico disciplinare di afferenza
FIS/05 - Astronomia e Astrofisica

Presentata da: Alberto Zonca
Coordinatore dottorato: Prof. Paolo Ruggerone
Relatore: Prof. Cesare Cecchi-Pestellini

Esame finale anno accademico 2012/2013

Alberto Zonca: *Dust Modeling and Evolutionary Implications*

Supervisor
Prof. Cesare Cecchi-Pestellini

Abstract

From the beginning of the 20th century astronomers started to move their studies toward that particular component which could be responsible of the reddening and the extinction of stars radiation. They agreed that this component must be represented by a population of microscopic particles named *interstellar dust*, that it must be mixed with the interstellar gas. Later on, in the second half of the century, dust was recognized to play very many important roles in the Milky Way and other galaxies. These findings changed the astronomer's view of the interstellar space, that is now fully considered as an active element in galactic evolution. For this reason to achieve a more reliable understanding of the nature of interstellar dust is necessary to take into account the response of dust to the physical conditions of the regions in which dust grains are embedded.

Over the years astronomers used the variation of extinction respect to wavelength, the interstellar extinction curve, to study cosmic dust. In this thesis I elaborate a physical and chemical model of dust, to investigate the remarkable variety of galactic interstellar extinction curves. In Chapter 1 I introduce the roles of the interstellar dust, its processing in the interstellar medium, and the tools to address the problem of its nature. In Chapter 2 I present the exploited model in a simplified version, and an application to some peculiar lines of sight in our galaxy. In Chapter 3 the complete version of the model is put forward, and, together with its simplified version, applied to a large sample of Milky Way interstellar extinction curves. All different flavours of observed extinction curves, ranging from the average galactic extinction curve to very peculiar profiles, can be described by such a model. I show that a mixture of core–mantle silicate/carbon grains together with a relatively small number (54 species in four charge states) of polycyclic aromatic hydrocarbons can reproduce the features of the extinction curve in the ultraviolet, dismissing an old objection to the contribution of polycyclic aromatic hydrocarbons to the interstellar extinction curve. In Chapter 4 I compare an evolutionary model of the physical properties of carbonaceous grain mantles with their determination through the fitting procedure outlined in Chapter 3. The results of such comparison demonstrates, that in the framework of the adopted dust model, the whole sample of galactic extinction curves are in striking agreement with the proposed evolutionary scenario, requiring physical conditions fully consistent with standard values of density, temperature, radiation field intensity, and average age of diffuse interstellar clouds. The results of this thesis show that the present model is able to reconcile the great variety of observed interstellar extinction curves within an unified evolutionary scenario, without making drastic changes to structural properties of dust grains.

Contents

Chapter 1

Interstellar dust from the beginning

1.1 Introduction

In the eighteenth century astronomers had noticed wide regions in the sky where they could not observe stars. The first astronomer who discussed this evidence was William Herschel: he called *löcher in den himmel* (holes in the sky) these regions apparently without stars. Many years later, Wilhelm Struve realized that starlight suffers absorption in proportion to the distance travelled. In 1930, studying open clusters, Robert J. Trumpler discovered an anomaly in the open clusters size; so he deduced that something was present between the observing astronomer and the open clusters, microscopic solids, later on called *interstellar dust*, could affect the measure of stars distances.

Astronomers measure stellar distances comparing the apparent magnitude with the absolute magnitude, obtained with the spectral classification

$$m_V - M_V = 5 \log d' - 5 \tag{1.1}$$

where m_V and M_V are apparent and absolute visual magnitudes, respectively and d' is the apparent mean cluster distance in parsecs[1]. Knowing d', Trumpler could deduce the linear diameter of each cluster geometrically from the measured angular diameter. He derived a remarkable trend: clusters diameters appeared to increase with distance from the Solar System. To make sure that the cluster diameters were independent of distance, he introduced a distance–dependent correction in the left hand–side of equation (1.1)

$$m_V - M_V - A_V = 5 \log d - 5 \tag{1.2}$$

where d is now the real distance of the cluster and A_V is the correction. To shed light on the nature of the correction, Trumpler studied the colours of stars involved in the measurements, finding that their spectra appeared to be shifted towards the red, or "reddened": clearly A_V should be more efficient for wavelengths shorter than in the visible. In particular, having compared the apparent luminosities of similar stars, Trumpler inferred that A_V was a linear function of the wavenumber, $A_V \propto \lambda^{-1}$. This result indicated that interstellar extinction must be due to the presence of solid particles

[1] This equation is derived by the definition of magnitude m from the brightness F: $m(\lambda) = -2.5 \log F(\lambda) + C$ in which C is a constant dependent by the wavelength. The absolute magnitude is defined like the apparent brightness which a star would have if it were placed at a standard distance of 10 pc away; then exploiting the relation between luminosity and brightness: $L = 4\pi d^2 \cdot F$, in which d is the true distance of the source from the observer, I obtain $M - m = -2.5 \log(4\pi d^2 F / 4\pi 10^2 F) = -5 \log(d/10)$; From this relation the equation 1.1 is readily derived.

with dimensions comparable to visual wavelengths. This was the first determination of a tool that astronomers are now routinely using to describe the interaction of stellar radiation with dust along a particular line of sight: the *extinction curve*, a relation that links the extinction of stellar radiation to the wavenumber.

The knowledge of the existence of dispersed solids in space could have helped those astronomers who, in 1920, had discovered that many stars close to the galactic plane appeared redder then expected on the basis of their spectral types. There was a discrepancy in stellar temperature derived by spectroscopy and photometry. By means of spectral classification star temperatures may be evaluated through the presence and relative intensities of spectral lines in the stellar photosphere. Instead colour indices, like $(m_B - m_V)$[2], are indicators of temperature based on the continuum slope and its equivalent blackbody temperature. Many stars, that showed spectral features of early-type stars, had colour indices more appropriate to late-type stars. Such results are easily explained by the reddening caused by foreground interstellar dust along the line of sight (Whittet, 2002): stellar spectra in a limited range do not change with reddening, instead colour indices depend on temperature and reddening.

Usually the extinction is reliably determined using the pair method, comparing spectrophotometry of two stars of the same spectral class: if one star has negligible foreground dust, while the second star is reddened, comparison of two spectra, with the assumption that extinction goes to zero at very long wavelength, allows to determine the extinction as a function of wavelength (Draine, 2003).

The degree of reddening or selective extinction is quantified through the color excess

$$E_{B-V} = (m_B - m_V) - (m_B - m_V)_0, \tag{1.3}$$

where $m_B - m_V$ and $(m_B - m_V)_0$ are observed and intrinsic values of colour index, respectively. Since the extinction is greater in the B band than in V one, E_{B-V} is a positive quantity for reddened stars and zero for unreddened stars. An important relationship between total extinction and color excess is

$$R_V = \frac{A_V}{E_{B-V}}. \tag{1.4}$$

In equation (1.4) E_{B-V} is directly measurable, whereas A_V is evaluated only if R_V can be determined. As extinction decreases rapidly as wavelength increases, I obtain

$$R_V = -\lim_{\lambda \to \infty} \frac{E_{\lambda - V}}{E_{B-V}}. \tag{1.5}$$

Theoretically, R_V is expected to depend on the composition and size distribution of dust grains. In the low density interstellar medium, R_V is virtually constant

$$R_V \approx 3.05 \tag{1.6}$$

(Fitzpatrick and Massa, 2007).

Prior to the mid-1960's, interstellar extinction was accessible to study mainly in the visible part of the spectrum, where it was known to increase linearly for decreasing wavelength, and was therefore believed to be essentially due to scattering and absorption by some form of small dust particles. With the opening of the UltraViolet (UV)

[2] m_B is the apparent luminosity in blue range of electromagnetic spectrum; the relative extinction at a generic wavelength is expressed as m_λ.

and InfraRed (IR) portions of the spectrum to astronomical observations, Whitford (1948) produced an InterStellar Extinction Curve (ISEC) that showed curvature at the near-UV and IR regions. As pointed out remarkably by Greenberg and Shen (1999) "things were beginning to make some physical sense from the point of view of small particle scattering". Indeed, at that time van de Hulst (1949) put forward the first comprehensive model of interstellar dust, and having a realistic dust model he developed the scattering tools to handle the problem (van de Hulst, 1957). Since then interstellar dust has become one of the subjects in the forefront of astrophysics.

1.2 The many roles of dust in the interstellar medium

Since its discovery, the astronomers regarded the dust as a disturb for the observations of stars, an irritating fog which precluded a clear view of stellar spectrum. For this reason the first studies of interstellar dust were motivated by the desire to correct photometric data for its presence. Nevertheless, as it was later understood, dust has very many important roles to play within the Milky Way Galaxy (MWG) and other galaxies, and it is a crucial component in the evolution of galaxies.

An important role of the dust is the shielding of nebular regions from starlight, favouring the build-up of a complex chemistry. Molecules formed in this chemistry are important because they can be used by astronomers to trace the presence of gas and its physical condition through IR and radio emissions wich are unaffected by dust extinction. Dust grains are the primary repository in the InterStellar Medium (ISM) for many chemical elements, and catalyse the formation of H_2, the most abundant molecule in the ISM. Hydrogen exists predominantly in its $1s$ ground state, and collisions between hydrogen atoms can proceed along two potential energy curves, in which the electronic spins are either parallel (triplet state) or anti-parallel (singlet state). As the atoms are initially unbound, their total energy is positive (the zero of the total energy is taken at the molecular dissociation limit). In order to stabilize, the system must lose energy and its total energy become negative. In the gaseous phase this may occur either by means of three-body collisions, the third body taking away the excess energy, or by means of radiative processes. Three-body collisions are extremely improbable at interstellar densities, and so the only way in which the system can stabilize is through the emission of a photon. Unfortunately, transitions between the triplet and singlet electronic potential energy curves are forbidden to electric dipole radiation as they involve a change in the total spin quantum number. Radiative transitions involving the nuclear degrees of freedom (rotation and vibration) are also forbidden, as the H_2 molecule is homonuclear and does not possess a permanent dipole moment. It is widely accepted that H_2 forms on grain surfaces: H atoms stick to grains and become trapped at surface defects in the grain structure. During the recombination the H_2 binding energy, 4.476 eV, must be partitioned between the rovibrational excitation and translational energy of the nascent molecule and heating of the dust grain (Parneix and Brechignac, 1998). If the internal and translational energies of newly formed molecules are relatively small, then significant grain heating must take place, which may lead to the desorption of volatile molecules from the dust grain surface (Duley and Williams 1993, Roberts et al. 2007). The H_2 internal energy distribution could have a significant impact on the chemistry occurring in the ISM because vibrationally excited H_2 will increase the overall energy budget of gas-phase processes. There have been many theoretical and laboratory studies that predict H_2 to be formed in highly excited rovibrational states

(e.g., Sizun et al. 2010, Martinazzo and Tantardini 2006 and references therein). It is possible that this formation pumping may be observable in the IR spectra of particular astronomical regions (Islam et al., 2010).

Surface reactions may lead to the formation of species heavier than H_2. At the low temperatures of dense molecular clouds gas-phase species condense onto dust grains forming icy mantles. During the process, when species such as e.g., OH and CO freeze-out on dust, they become hydrogenated via surface reactions and form H_2O and methanol. The rate at which these reactions occur increases with the density of the cloud. Icy mantles exposed to shocks or heated nearby a nascent star become sources of complex molecules. Thus, at all level of density, the exchange of material between interstellar gas and grains is important for the chemical composition and evolution of the ISM as a whole.

Dust is involved in the formation and evolution of stars and planetary systems. Indeed stars are born within very dense cloud of dust and gas and the presence of dust, being an efficient radiator of excess heat energy, favours gravitational collapse to form protostars. As protostar contracts, rotation flattens the circumstellar envelope in a disk-like structure. Proto-planetary disks have been detected around young stars through extinction and emission arising from the dust they contain. The effect of the radiation pressure on grains may influence the dynamics of stellar envelope surrounding both young and evolved stars. Grains condensing in the envelopes of late-type giants may drive the outflows of evolved stars, and contribute significantly to the enrichment of the ISM with heavy elements.

Since dust obscures stellar light, it must re-emit at longer wavelengths (Witt and Gordon, 2000). Thus, dust manifests itself through continue emission at $\lambda > 1$ μm. Such emission beyond a few μm and up to 100 μm is mainly due to discrete photon heating of very small dust grains; dust heated by massive stars to temperature larger than 50 K also contribute to the flux in the wavelength region below ~ 50 μm. Beyond $40-70$ μm, the emission is due to dust grains in nearly steady balance with the average heating by starlight. Dust shows also emission and absorption features, that, in the near/mid-IR, include absorption bands such as e.g., those of silicate materials at 9.7 and 18 μm, frozen H_2O and CO_2 at 3.0 and 4.3 μm (Öberg et al., 2011), and the emission bands at 3.3, 6.2, 7.7, 8.6 and 11.3 μm (Tielens, 2013).

In addition to extinction, dust particles produce polarization, mainly linear, of stellar light. To explain interstellar polarization, dust grains are represented as spheroids, describing a rotation about the major axis of an ellipse (prolate spheroid) or the minor axis (oblate spheroid); grain shapes are characterised by the elongation, defined as the ratio between major and minor semi–axes. It is generally found that stellar radiation is polarized by partially aligned spheroidal dust grains which fluctuate and rotate about the axis of greatest moment of inertia. The degree of linear polarization depends on the type of the spheroid, prolate or oblate, its elongation and the alignment efficiency. When detectable, circular polarization can also provide informations on grain shape and elongation.

Finally, dust induces the reddening of extragalactic background light, the cumulative radiative output from all energy sources in the universe since the epoch of recombination. The subsequent emission at IR wavelengths produces the cosmic IR background (Dwek, 2001).

The properties of the dust are quite well known in general terms for the MWG (at least within 2 kpc from the Sun). However, the extinction profile and its absolute value vary with the line of sight, even in directions away from the plane of the MWG.

Since the spectral distribution depends on the composition and geometry of grains, I can conclude that dust grains evolve in response to regional physical conditions, such as e.g., chemical enrichment, dynamics, irradiation, and energy content.

1.3 Interstellar dust life–cycle

From spectral features in extinction, scattering and emission astronomers can infer the chemical composition of dust. Based on such studies carbon and silicon are considered as principal components for interstellar dust grains.

The strongest spectral feature observable in the extinction curve is centered at 4.6 μm^{-1} and it is named *bump* (see figure 1.2). It suggests the presence of carbon in aromatic form, since this feature is attributed to $\pi^* \leftarrow \pi$ absorption. Other features distinctive of aromatic carbon are the emission bands at 3.3, 6.2, 7.7, 8.6, and 11.3 μm, called Aromatic Infrared Bands (AIBs). These emission features are associated to H atoms attached to the edge of a carbon ring skeleton giving rise to the following vibrational modes (Allamandola et al., 1989): i) 3.3 μm C–H stretching mode, ii) 6.2 μm C–C stretching mode, iii) 7.7 μm C–C stretching mode, iv) 8.6 μm C–H in plane bending mode, v) 11.3 μm C–H out of plane bending mode for the case in which there are not H atoms adjacent.

Indeed, the only secure identification of carbon in dust grains is the broad feature at 3.4 μm observable in diffuse atomic regions, and indicative of the C–H stretching mode in aliphatic hydrocarbons.

Silicate minerals generally have strong absorption resonances around 10 μm due to Si–O stretching. The observational evidence of an emission feature near such wavelength observed in outflows from cool oxygen rich stars (where silicate materials would condense) but not in outflows from carbon rich stars (where oxygen should form CO and not silicates) supports the identification of silicates in space. Moreover, a weaker feature at 18 μm is also observed, suggesting the presence of the O–Si–O bending mode in silicates.

Interstellar dust is thought to form around evolved stars (i.e. giant branch stars, asymptotic giant branch stars and supernovae), and then ejected into the surrounding ISM by stellar winds. Here dust grains are subject to violent processing in fast shock waves generated by supernova. Such stars are believed to be responsible for the formation of dust in high redshift galaxies too. Amounts of dust larger than $10^8 M_\odot$ are detected in sub–millimetre galaxies and quasars at high redshift from a number of instruments such as SCUBA, MAMBO, MAMBO-2 and VLA. The age of the Universe at $z > 6$ was less than 1 Gyr, and early star formation took place at redshift ~ 10, approximately 500 Myr after the Big Bang (Greif and Bromm, 2006). The maximum time available to build a similar large dust mass was at most $400 - 500$ Myr. Considering that dust is produced by stars towards the ends of their life, in high redshift galaxies only massive stars have sufficiently short lifetime within the age of the Universe at this redshift, such as high mass asymptotic giant branch stars with masses between $3 - 8$ $M_\odot$ have lifetimes of a few $10^7 - 10^8$ years and they can be potential contributors to dust production in high redshift galaxies. Some features in extinction curves of various objects at high redshift have been attributed to dust of supernova origin as the plateau observed at around $170 - 300$ nm, possibly arising from amorphous carbon and magnetite supernova dust (Maiolino et al., 2004). However, the correspondence with minimum mass of ~ 3 $M_\odot$ are potential dust sources: i) stars with a mass end

of $3 - 8$ $M_{\odot}$ evolve to AGB stars and let out dust through intense mass–loss; ii) stars more massive than 8 $M_{\odot}$ explode as supernova, but to date the correspondence among the star mass, the type of the supernova and the dust mass is not clear yet (Gall et al., 2011). Exploiting the *Herschel* satellite at far-IR wavelengths Matsuura et al. (2011) present the first direct evidence that substantial amounts of dust can be created in supernovae. Matsuura et al. (2011) observations demonstrate the presence of dust in supernova 1987A in a much larger amount than previously known, and inferred that indeed most of the refractory material in the ejecta of the supernova has condensed into dust. Although substantial, the dust production rate appears to be not sufficient to eliminate the need for grain growth in the ISM in the Large Magellanic Cloud (LMC), as well as, for comparison, in our own galaxy (McKee, 2011).

In ISM silicate dust appears to be amorphous due by dust processing of newly formed crystalline silicate grains. The differential acceleration of the gas and dust in supernova shock waves produces high–velocity ion impacts on grains that can sputter atoms of the grains and/or amorphise crystalline materials (Jones, 2004). Prior to the Infrared Space Observatory (ISO) mission all silicates in space were thought to be amorphous as a result of their rapid gas phase formation in low–density circumstellar shells. Observations with ISO, at wavelengths covering the $2.5 - 200$ μm range, revolutionised our thinking of dust in space with the discovery of thermal emission from crystalline silicates in the dust shells around stars in their late stages (Jones, 2009). However, crystalline silicates were identified in dust extracted from the comet 81P/Wild 2 and their presence in other comets has been revealed by IR spectral features (Wooden, 2008). Other samples of crystalline silicates with anomalous signatures that indicate that they formed around evolved stars in pre–solar epoch have been extracted from primitive meteorites. Their isotopic compositions show values very far from the solar system ones. Such isotopic anomalies are characteristics of the nucleosynthetic processes occurring within some stars at particular phases in their evolution (Jones, 2009). The formation process for crystalline silicate is still uncertain, but some speculation was made. Ábrahám et al. (2009), observing the mid-IR spectra of the star EX Lupi (a young Sun–like eruptive star which shows repetitive outburst) in two separate epochs, were able to recognize typical feature for amorphous silicate in the first epoch spectrum (the star was in a quiescent phase), and peaks characteristic of crystalline silicates superimposed on amorphous silicate feature in the second epoch spectrum. These features are very similar to those observed in cometary spectra. A possible interpretation considers crystallinization as produced by thermal annealing in the star's inner disk by outburst. A problem could be represented by the transport of these crystalline silicates to be incorporated into comets as observed, since the comet forming zone is the cold, outer region of the star's disk. A possible answer could be given by the "X–wind" model, in which dust grains are ballistically launched above the disk's mid–plane and transported outward (Shu et al., 1996). This model could have some problems in explaining the observed levels of transport. However, it is also possible that some crystalline silicates are made in situ in cometary comae (Li, 2009). In the ISM $\sim 95\%$ of silicate material is amorphous (Li and Draine, 2002), in some circumstellar disks the crystalline fraction appears to be higher but the bulk of the silicates remains amorphous. On the other hand carbonaceous materials are crystalline in the form of graphite or diamond, or amorphous in the form of Hydrogenated Amorphous Carbon (HAC).

Dust evolves in the ISM through constructive processes, and, during its life–cycle, dust is also subject to destructive/disruptive processes. Dust destruction processes which destroy and change the configuration of dust grains are many. These processes

occur in a variety of interstellar environments, including regions of intense stellar radiation fields (HII regions, γ–ray bursts, ...), in the hot gas behind supernova remnants and in interstellar shock waves. In general term a dust destruction process is any interaction between a grain and another particle that leads to a net baryon loss from the grain (Jones, 2004), with the outcome of the interaction depending by the total energy of the collision and the coupling between the particle and the grain. The importance of these processes are evident from the large variations seen in the ISEC from one sightline to another: these differences are originated by interstellar processes because each sightline is expected to average over the stardust produced by many individual stars. The major particle–grain interactions are the following:

- *Photon–grain interactions*; low energy photons (radio and IR wavelengths) are weakly absorbed by refractory dust materials. On the other hand higher energy photons can be absorbed and scattered leading to the heat of grains and causing thermal emission. Such kind of interactions are not destructive processes. When similar processes occur for more volatile materials, such as ice mantles, the absorption of UV photons becomes an important destruction mechanism (Draine and Salpeter 1979a, Westley et al. 1995a,b). Muñoz Caro et al. (2010), in their experiments, measured CO photodesorption from UV irradiation at 7, 8 and 15 K. They found the photodesorption yield of CO ice is constant during irradiation and independent of the ice thickness. They found also that the photodesorption yield at 15 K ($\sim 3.5 \pm 0.5 \times 10^{-2}$ CO molecules photon $(7.3 - 10.5\mathrm{eV})^{-1}$) is about one order of magnitude higher than the previous estimate. Only high energy photon interactions can result in grain destruction via direct heating (Guhathakurta and Draine, 1989) and via extreme grain charging effects (Draine and Salpeter 1979b, Waxman and Draine 2000, Fruchter et al. 2001). The interaction of grain with UV photons and the grain heating are responsible for the loss of H atoms from the carbonaceous material in the polymeric form (sp^3) and its transition to the graphitic form (sp^3) (Jones et al., 1990). Because of irradiation, in carbon materials exposed to above– and near–bandgap radiation the absorption coefficient over a broad range of frequencies increases. The amount of increase depends on the wavelength and the intensity of the inducing radiation, and the duration of the exposure, leading to a shift of the optical absorption edge to lower energy and an increase in the band tail absorption. The physical and chemical transformation is complex, involving selective photo–dissociation of chemical bonds, selective sputtering which reduces the relative H, N, and O content, restructuring of chemical bonds to form increasingly large aromatic platelets (see e.g. Jones 2012a,b). However, the net apparent effect is a change in colour of the processed carbonaceous material, with a progressive darkening, i. e. from transparent to "yellow stuff" and to "brown stuff" (Greenberg, 1984). Such a process is called *photo-darkening*.

- *Electron–grain interactions*; generally this kind of interactions are not important destructive processes. These interactions produce electron sticking leading to negative grain charging. According to Draine and Salpeter (1979b) positive grain charging is also possible when energetic electrons impacts cause the emission of secondary electrons.

- *Particle–grain interactions*; these are important destruction mechanisms and we can distinguish interactions at high energy from interactions at lower energy.

When the particle energy is $\geq$ MeV it is classified as cosmic ray and the interaction regards essentially Coulomb interactions between cosmic rays and charged dust grains. The effect decreases with the increasing relative speed between the grain and the charged particle. The scattering frequency ν_0 of this interaction can be approximated as the product of the Rutherford cross–section, proportional to v_{cr}^{-4} (v_{cr} is the speed of the cosmic ray) with the density of scatterers and the speed of cosmic ray; the scattering frequency results $\nu_0 \propto v_{cr}^{-3}$. It is clear that these interactions have a relevant role if there is a large energy density in low energy ($\leq$ 100 MeV) cosmic rays (Byleveld et al., 1993). These interactions can produce grain heating, charging and ionization effects; regarding this last effect cosmic–rays which pass through the dust grain may be more important than Coulomb interactions, due to the net effect of all cosmic rays that pass within a Debye length[3] (of order hundreds of meters) of the dust grain. Unfortunately, low energy cosmic rays cannot be observed into the solar system because solar cosmic rays dominate the cosmic ray spectrum at energies lower than 100 MeV, so currently we have scarce information about the abundance and energy spectrum of galactic cosmic-rays. Instead at lower energies interactions can produce different effects. For energies $>$ 10 eV per nucleon these interactions can produce sputtering of atoms from the grain. This process occurs in shock waves generated by supernovae explosions; it clearly depends by the incident atom/ion energy and different sputtering yields are obtained with different energies. The sputtering yield, in addition to the kinetic energy of the incident atom/ion, depends upon the angle of incidence according the rate given by Draine and Salpeter (1979b). If the sputtering efficiency is less than unity (it can happen for refractory materials) atom/ion sputtering also produces an implantation into the grain increasing the grain mass. Hence, there is a destruction process that is accompanied by a grain growth process.

- *Grain–grain interactions*; low energy grain–grain collisions with velocities lower than 0.02 km/s, produce grain sticking and coagulation of grains into aggregates, resulting in a net increase in the average grain size (Chokshi et al., 1993). At velocities of the order of 1 km/s grain fragmentation or destruction can occur: i) for solid homogeneous particles this process consists in the shattering of the solid particle in a multitude of smaller fragments, ii) for aggregates of particles the process results in the disaggregation of the grain into its component sub–grains (Dominik and Tielens, 1997). Finally at high velocities ($v \geq 20$ km/s) grain–grain collision produces the partial or total vaporization of the colliding grains.

Supernova shock waves have a fundamental role in dust processing and dust destruction, through sputtering, vaporization, shattering and disaggregation, if the shock wave velocity at the point of interaction is fast enough ($>$ 50 km/s). Following the discussion of McKee (1989), the timescale for supernova shock waves to destroy all dust in the galactic ISM is

$$t_{\rm d} = \frac{9.7 \times 10^7}{\int \epsilon(v_{s7}) v_{s7}^{-3} dv_{s7}} \ {\rm yr}, \tag{1.7}$$

where v_{s7} is the shock velocity in units of 10^7 cm/s and $\epsilon(v_{s7})$ is the grain destruction efficiency for a shock wave with velocity v_{s7}. Jones et al. (1996), considering grain

[3]The Debye length is the measure of a charge carrier's electrostatic effect and how far those electrostatic effects persist.

shattering effects on grain–grain collisions (this process allows the redistribution of grain mass through the fragmentation of large grains into small grains), found a lifetime of the order 4×10^8 years for silicate grains and 6×10^8 years for carbon grains. This lifetime may be shorter by about an order of magnitude in the case of large grains ($a \geq 100$ nm). Comparing this lifetime with the formation rate I obtain $t_{\rm f} \approx 3 \times 10^9$ yr, assuming a dust to gas ratio is 0.01, typical supernova mass injection of heavy elements into ISM $\sim 4 M_{\odot}$, dust formation efficiency of 50% in which it is incorporated 25% of the available O into silicates or oxides, and a supernova rate of 1/(30 yr) (Jones and Tielens, 1994). Clearly dust destruction seems to be faster than dust formation by about an order of magnitude. Thus, to explain the presence of dust in the ISM, I need to assume that dust can be re–accreted and re–condensed in the ISM as suggested by Dwek (1998) and Weingartner and Draine (1999). Considering the average residence time of an atom in a grain, the total mass of ISM and the star formation rate for the MWG, one expects that only 20% of Si atoms would be found in the original stardust particle. On the other side, astronomers infer that the 90% of Si is missing from gas–phase. Therefore, most of the Si atoms in interstellar grains should be incorporated into dust in the ISM: most of interstellar dust is not of stellar origin but it is formed from physical processes in the ISM (Draine, 2003).

For galaxies like the MWG a possible interstellar formation process is accretion. Elaborating a particular galaxy evolution model taking into account the metallicity and age dependence on the various dust sources, Asano et al. (2013) found that the accretion time-scale depends by the gas metallicity. If metallicity exceeds a given critical value the dust mass growth becomes active, with dust grains rapidly increasing their masses until metals are depleted from the ISM. This critical metallicity changes with the star formation timescale: it is larger for a fast star formation rate (see figure 1.1). Then the dust mass growth in the ISM could be the dominant source of dust in galaxies like the MWG.

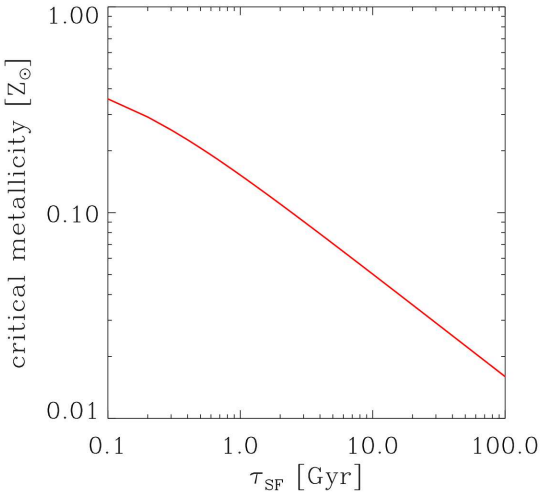

Figure 1.1: Plot of the critical metallicity (in unit of solar metallicity $Z_{\odot}$ versus star formation timescale according Asano et al. (2013)

An important form of dust mass accretion is the formation of carbonaceous mantles onto silicate cores. Silicate materials are refractory and then more long lived than carbonaceous materials. In hydrogen/carbon rich, low temperature environments solid carbon can be deposited on the surfaces of silicate cores with the following rate of increase for the dust grain mass

$$\frac{\mathrm{d}m_\mathrm{d}}{\mathrm{d}t} = \xi\pi a^2 n_\mathrm{C}(2.5kT_\mathrm{k}m_\mathrm{C})^{\frac{1}{2}} \tag{1.8}$$

in which m_d is the mass of the grain, ξ is the sticking coefficient, a is the grain size, n_C is the numerical density for accreting carbon particles, m_C is the atomic carbon mass and T_k is the kinetic temperature of the gas. Then if the mantle has a density ρ the rate of growth of grain is given by

$$\frac{\mathrm{d}a}{\mathrm{d}t} = \frac{1}{4\pi a^2\rho}\frac{\mathrm{d}m_\mathrm{d}}{\mathrm{d}t} = 0.4\xi n_\mathrm{C}\rho^{-1}(kT_\mathrm{k}m_\mathrm{C})^{\frac{1}{2}}. \tag{1.9}$$

The equation 1.9 shows that the mantle growth is independent by the value of the grain size; in a time interval Δt mantles with the same width are formed over all grains. Other factors can influence the mantle formation: i) mantle can desorb more rapidly from smallest grains if a significant UV radiation field is present; ii) coagulation may operate together with the mantle growth. The condition and the mechanism of deposition suggest that carbon which form the mantle is in the HAC polymeric form (Jones et al., 1990). From considerations based on the *Random Covalent Network* model and the *Constraint Counting Method* Jones et al. (1990) obtained the sp^3/sp^2 ratio for carbonaceous materials composed by carbon with this bonds and hydrogen in atomic fraction f_H

$$\frac{n_{sp^3}}{n_{sp^2}} = \frac{6f_{\mathrm{H}-1}}{8-13f_\mathrm{H}}. \tag{1.10}$$

where n_{sp^2} and n_{sp^3} are the densities of sp^2 and sp^3 bonding sites, respectively.

The hydrogen fractional abundance is thus in the range $1/6 < f_\mathrm{H} < 8/13$, which in percentage results between 17% and 62%. From equation 1.10 I can infer that decreasing the hydrogen fractional abundance increase the quantity of carbon hybridized sp^2 and increasing the hydrogen abundance increase the quantity of carbon hybridized sp^3. It is known that in the hydrogen/carbon rich and low temperature environment of the ISM solid carbon will be deposited on grains core. At low temperatures, the interactions of H atoms with solid carbon produce H_2 and the mechanism by means the carbon is deposited is the chemical mechanism of carbon insertion, particularly efficient at low temperature for both C atoms and C^+ ions facilitating the grow of hydrogenated carbon chains. Therefore when HAC material is deposited on the grain surface it is hydrogen–rich and, from the equation (1.10), it is essentially sp^3 bonded. Due to thermal annealing or exposure to UV radiation hydrogen atoms may desorbe from the mantle, leading to an increase in the sp^2 bond density. The net result is the formation of a double layer of carbonaceous materials: an outer freshly deposited sp^3 layer embedding an internal sp^2 zone. Clearly, during the grain lifetime, the inverse process is also possible, in which the graphitized material absorbs (hot) hydrogen atoms in its matrix and sp^3 bonds increase (Mennella et al., 2001).

The model exploited in this thesis is inspired by this scenario in which the carbon is deposited in the aliphatic (sp^3 bonded) form and it is processed by annealing an radiation UV in the aromatic (sp^2 bonded) form at the *photodarkening rate*.

1.4 The problem of cosmic abundances

An important and open question in our understanding of the ISM is the amount of metals incorporated into dust grains, a quantity that cannot be derived directly from observations. The chemical composition of the dust is found by comparing the abundances of the various elements in the gas phase alone derived from highly sensitive, high-resolution UV absorption measurements with an IS reference abundance set (e. g., Miller et al. 2007). Additional information comes from X-ray absorption and scattering measurements (Valencic and Smith, 2013), analysis of components of interplanetary dust particles (Bradley et al., 1999), and, in dense clouds, from IR observations of solid-state absorption bands (Öberg et al., 2011). The derived dust metal abundances are, however, very uncertain, because such inference relies on the assumed composition of the total, gas + dust, abundances in the ISM.

Hydrogen and helium constitute about 98% of the matter in the Universe. The elements that are mostly locked in dust grains are C, O, N, Mg, Si and Fe. The determination of their reference abundances has a long history. Because the Sun is the closest star, its chemical abundances can be determined with high accuracy. Moreover, the chemical composition of the Sun was thought to be typical for our Galaxy, and, indeed, solar composition represents a good reference for several astrophysics studies as Galactic chemical evolution of older star populations and solar-type stars. About 30 years ago, Greenberg (1974) published a remarkable paper entitled in part *where have those atoms gone?*: this was the first critical look at the problem of chemical abundances in the ISM. Greenberg pointed out that, on the base of the *Copernicus* satellite data, the abundances of elements such as carbon, oxygen, and nitrogen, much more was missing from the gas that could be incorporated into dust under any reasonable models. Twenty years later Snow and Witt (1996) gave an answer to the Greenberg's question: *the unaccountable atoms were never missing after all.* In other words, solar abundances are not a proxie for the ISM. Basically, the crucial problem is to understand to what extent the local ISM is chemically homogeneous, and the types of stars to be used as proxies for ISM abundances: the Sun, young hot stars or young cool stars? All of these stars have been exploited but the derived abundances often disagree, and moreover, they are rather erratic (Sofia, 2004). From the paper put forward by Snow and Witt (1995), cosmic abundances posed severe constraints on dust models: the was no longer any need to find hidden reservoirs of interstellar C, N, and O. Moreover, the former surplus of raw materials for the interstellar dust was turned into a shortage. Snow and Witt (1995) determined a carbon abundance in the ISM of 225 ± 50 ppM, against a current value (at that time) of 335 ppM for carbon abundance in solar environment (Grevesse et al., 1994). This problem opened the so–called *carbon crisis*, in which existing models of cosmic dust needed to be modified taking into account the rather limited elemental budget available.

Now, the elemental abundances represent an additional constraint to introduce in models reproducing interstellar extinction. The very tight limits imposed by the Snow and Witt (1995) observations were fortunately soon dismissed. From newer observations, it was discovered that it was quite hard to define a standard reference for interstellar abundances, with observations towards stars of different types showing different amounts of metals incorporated into dust (Zubko et al., 2004). The concentrations of the elements change significantly along different lines of sight, with a wide dispersion. Such a constraint has became dependent on the specific line of sight.

The most common method to determine abundances of the elements in the dust

phase is the indirect procedure, that is, to measure the gas–phase abundance and subtract this from the total (gas+dust) abundance. In the solar neighbourhood, chemical abundances can be inferred from absorption line studies of cold and warm ISM or from emission line spectroscopy along the Orion nebula. Over large distances, even in other galaxies, region HII can be considered good sites for the determination of chemical abundances; but the composition of ionized gas presents important complications due to the dependence of the derived abundances on the indicators used in the analysis (Simón-Díaz and Stasińska, 2011), to the ionization corrector factors and to large systematic errors from temperature fluctuations in the nebula (Mathis, 1995). A good alternative to find a reference for the chemical composition of ISM is represented by unenvolved early B type stars. These stars have a mass about $8 - 18\,M_{\odot}$ and they can be observed in the solar neighbourhood and also at larger distances in the MWG and in other galaxies. Their life is very short, so they have not the necessary time to travel far away from their birth site and spectroscopic studies of early B type stars are simple because their photosphere is not affected by stellar winds. But despite this simple physics, spectral analyses of main sequence B type stars produced unclear results, summarized in a tendency towards a metal poor composition in comparison with older stars like the Sun and a large range in elemental abundances. According to some studies B stars cannot be considered an accurate indicator of ISM abundances, because element stratification due to diffusion is common in these stars (Hempel and Holweger, 2003). Thus, the abundances measured at their surfaces do not necessarily reflect the abundances of the clouds from which they are formed. The latest works on B star abundances seem to ease differences between them and solar values (Nieva and Simón-Díaz 2011, Nieva and Przybilla 2012). Recently, studying nearby B stars, Nieva and Przybilla (2012) found an high degree of chemical homogeneity of the stars in the sample, so they could define a Cosmic Abundance Standard (CAS) for the actual chemical composition of the cosmic matter in the solar neighbourhood. In the Table 1.1 it is highlighted the reduced CAS metallicity, $Z = 0.014$ obtained with respect to the canonical solar one, $Z_{\odot} = 0.02$ (Anders and Grevesse, 1989).

	Hydrogen	**Helium**	**Metals**
Mass fraction	0.710	0.276	0.014

Table 1.1: Mass fractions for hydrogen, helium and metals according to Nieva and Przybilla (2012).

In the table (1.2) abundances, derived observing along different type of stars, are displayed- The gas–phase component of the local ISM is well known because determined by many UV–optical absorption studies. Such component appears independent by the line of sight towards the assumed reference star and it suggests that there is a standard local ISM abundance. Particularly young stars should provide a good reference since little chemical evolution as occurred since their formation. For this reason B stars and young later type stars (as F and G stars) are popular proxies for the ISM composition. In the table (1.2) to infer the abundances available for elements locked in grains it is sufficient to make the difference between the typical chemical composition of the star and the ISM gas–phase abundances. Nieva and Przybilla (2012) obtained their abundances analysing 29 B stars with sophisticated models, inferring a silicate rich and relatively poor carbon nature of the local ISM dust. Other studies seem to consider that B stars could be good indicators of abundances in the local ISM (e.g., Valencic and Smith, 2013). Before the increasing in the accuracy in the study of B star abundances, only

	Carbon	Nitrogen	Oxygen	Magnesium	Silicon	Iron
Gas – phase[a]	91 ± 6	62 ± 4	389 ± 9	1.5 ± 0.1	2.2 ± 0.3	0.2 ± 0.0
	B stars					
Total[b]	214 ± 20	62 ± 6	575 ± 66	36.3 ± 4.2	31.6 ± 3.6	33.1 ± 2.3
Dust	123 ± 23	0 ± 7	186 ± 67	34.8 ± 4.2	29.4 ± 3.6	32.9 ± 2.3
	F* & *G stars					
Total[c]	358 ± 82	–	445 ± 156	42.7 ± 17.2	39.9 ± 13.1	27.9 ± 7.7
Dust	267	–	56	41.2	37.7	27.7
	Sun					
Total[d]	269 ± 31	68 ± 8	490 ± 56	39.8 ± 3.7	32.4 ± 2.2	31.6 ± 2.9
Dust	178	6	101	38.3	30.2	31.4

Table 1.2: Observed, gas-phase, and inferred, dust-phase, abundances in the diffuse ISM per millions of hydrogen nuclei.
(a) Sofia et al. (2011) for C, Meyer et al. (1997) for N, Cartledge et al. (2004) for O, Cartledge et al. (2006) for Mg, Si, Fe.
(b) Nieva and Przybilla (2012).
(c) Sofia and Meyer (2001) obtained as averages from the surveys by Edvardsson et al. (1993) and Tomkin et al. (1995).
(d) Asplund et al. (2009).

F and G stars were considered good candidate as an proxies for the ISM abundances (Sofia and Meyer, 2001). Abundances for these stars provide reasonable values for all elements, but the nitrogen (see tab. 1.2).

A particular problem is represented by the oxygen depletion into the ISM. A recent study of Jenkins (2009) presented an extensive re–analysis of archival data for 17 elements. In this work is underlined that oxygen is being depleted from diffuse interstellar gas at a rate that exceeds by far that at which it can be incorporated into silicates and metallic oxides particles. Studying a wide range of environments, from tenuous intercloud gas and diffuse clouds to dense clouds where ice mantles and gaseous CO are important reservoirs of O, Whittet (2010) tried to understand what could be the potential carrier. He concludes that the most plausible reservoir can be a form of O–bearing carbonaceous matter similar to the organic matter found in cometary particles returned by the Stardust mission (van Dishoeck, 2008). Further studies are necessary to assess if this class of materials is present in quantities sufficient to account for a significant fraction of the unaccounted depleted oxygen.

1.5 Dust in our galaxy

In spiral galaxies like the MWG, dust resides mainly in the galactic disc, suggesting its association with the relatively stellar disc population. Within the disc, most of the material is confined to the spiral arms. In our galaxy dust represents only 1% of the ISM mass (Williams, 2000).

The distribution of interstellar matter in the disc of our galaxy is extremely uneven with inhomogeneities on all size scales from 10^{-4} to 10^{3} pc. The general tendency of the extinction to increase with the distance, due to the increase of traversed column density, is not linear with the distance. Usually clumps with a density of dust above the galactic average and with size over 1 pc are called *clouds* and a classification can be made following their dust density:

- *diffuse clouds* – are the most transparent clouds, they are composed mainly by atomic gas, although a strikingly molecular inventory has been detected (Liszt et al., 2008); the density is in the range $n_{\rm H} \sim 100 - 500\,{\rm cm}^{-3}$, while gas temperatures are $30 - 100$ K (Snow and McCall, 2006). Usually these clouds have an extinction $A_V \leq 2$ mag;

- *translucent clouds* – these objects are denser than diffuse clouds; they have an extinction of $2 \leq A_V \leq 5$ and they can be in the phase of gravitational contraction which is the prelude to star formation;

- *dense clouds* – they are the densest gas condensations ($10^3 - 10^6\,{\rm cm}^{-3}$); kinetic temperatures ranges between 10 and 50 K; they are mainly composed by molecular gas and, due to their high extinctions obscure background stars.

Our Solar System resides in a relatively transparent intercloud region near the edge of the Orion Arm of the MWG with little reddening, $E_{B-V} \leq 0.03$, for stars within a distance of 100 pc. On average, in a distance of 1 kpc a reddening of $E_{B-V} \approx 0.6$ occurs. Then, exploiting the equations (1.4) and (1.6) I obtain the average ratio of the visual extinction to path length

$$\langle \frac{A_V}{L} \rangle \approx 1.8\,{\rm mag\,kpc}^{-1}. \tag{1.11}$$

This estimate is valid only for distances up to a few kiloparsecs from the Sun, and for lines of sight which are close to the plane of the MWG. At greater distances it is very hard to determine this ratio because even the most luminous stars become too faint; e.g., the magnitude of a supergiant, 6.5 kpc far away, is about 20 mag for an average reddening. The extinction toward the IR cluster at the galactic center is estimated to be $A_V \approx 30$ mag for a path of ~ 8 kpc (Roche, 1988). For similar large distances IR photometry could be useful and informations about visual extinction could be inferred from assumptions regarding the wavelength dependence of the interstellar extinction. In general observations that extend beyond 3 kpc are based on long wavelength astronomy. For some lines of sight extinction is oddly low, making possible to extend studies at visible wavelengths up to distances of ~ 10 kpc.

Correlation of dust with gas was calculated using UV absorption–line spectroscopy of reddened stars within 1 kpc of the Sun. (Snow and McCall, 2006) found the following relation

$$\frac{N_{\rm H}}{E_{B-V}} = 5.9 \times 10^{21}\,{\rm cm}^{-2}{\rm mag}^{-1} \tag{1.12}$$

to be representative of dust in diffuse regions (Gudennavar et al. 2012, collecting absorption line data toward 3008 stars, update this value to $6.12 \times 10^{21}\,{\rm cm}^{-2}{\rm mag}^{-1}$). In this relation N_H is considered as the sum of molecular and atomic hydrogen

$$N_{\rm H} = N({\rm HI}) + 2N({\rm H}_2) \tag{1.13}$$

with the factor two allows for the fact that H_2 contains two protons. Exploiting the equations (1.4) and (1.6) I can convert reddening E_{B-V} in extinction in the visual wavelength A_V

$$\frac{N_{\rm H}}{A_V} = 1.93 \times 10^{21}\,{\rm cm}^{-2}{\rm mag}^{-1}. \tag{1.14}$$

This equation is representative of dust in diffuse clouds. Combining the equation (1.14) with the equation (1.11), I can eliminate A_V and write the average hydrogen number density

$$\langle n_{\rm H} \rangle = \langle \frac{N_{\rm H}}{L} \rangle \approx 1.04\,{\rm cm}^{-3} \tag{1.15}$$

This is the average density of ISM in the disc of our galaxy, but substantial deviations (also of orders of magnitude) can be found for individual regions cause the matter tends to be distributed into clumps with $n_{\rm H} >> \langle n_{\rm H} \rangle$ and interclump gas with $n_{\rm H} << \langle n_{\rm H} \rangle$. Using the equation (1.15) to determine the mass density and an height scale of 100 pc for the ISM I can also find the surface mass density: $\langle \sigma_{\rm H} \rangle = 5.3\,{\rm M}_\odot {\rm pc}^{-2}$.

Away from the galactic disc the extinction is generally low, but its entity is important to study intrinsic properties of external galaxies. Because the low density of dust in the halo of our galaxy, the reddening of stars which are observed in high latitude ($|b| > 20°$) is independent from the distance. Considering the disc as a flat, uniform slab with the solar system in the central plane I can infer a dependence of extinction from the latitude b

$$A_V(b) = A_{\rm P}\,{\rm cosec}|b|. \tag{1.16}$$

This dependence follows a cosecant law and $A_{\rm P}$ is the visual extinction at the galactic poles[4]. Clearly this formulation must be considered just as an approximation because the dust distribution is very inhomogeneous, and it can not be represented on small scales by a smoothly varying function; indeed some clouds situated at high latitudes are dense enough to contain a molecular phase and to produce significant extinction: $A_V \sim 1$ (Penprase, 1992). Many of these dense clouds are extensions of local dark cloud complexes, but other clouds appear to be isolated. Then for lines of sight which pass through these clouds the equation (1.16) will predict a lower extinction than the effectively observable one.

In the MWG ISECs show a great variety of features and shapes for different lines of sight. In figure (1.2) are plotted three galactic ISECs observed along three different lines of sight. Broadly characteristics of a typical ISEC can be summarized in this way: i) a linear trend in the visible portion of electromagnetic spectrum; ii) the *bump* at 4.6 $\mu{\rm m}^{-1}$ (to explain the presence of this prominent feature many hypothesis about its nature were been elaborated over the years); iii) a non linear rise in the Far UltraViolet (FUV) range of the electromagnetic spectrum.

Cardelli et al. (1989) elaborated an analytic formula which allows to derive an extinction law depending only from one parameter: R_V. This work started by the consideration that dust grains must suffered the same chemical processes for the whole dimensional distribution, that is chemical and physical processes must not be selective and they acted without distinction on the whole dust grains population.

Fitzpatrick and Massa (2007) presented an extensive set of 328 Galactic extinction curves that show a remarkable variety of shapes and features. These curves have been described in the UV ($\lambda^{-1} \geq 3.7\,\mu{\rm m}^{-1}$) by means of a 7–parameter description. The common features in the Fitzpatrick and Massa (2007) sample are a Drude profile, a non–linear rise in the FUV, and a linear baseline

$$\frac{E(\lambda - V)}{E(B - V)} = \begin{cases} c_1 + c_2 x + c_3 D(x, x_0, x_1), & x \leq c_5, \\ c_1 + c_2 x + c_3 D(x, x_0, x_1) + c_4 (x - c_5)^2, & x > c_5, \end{cases} \tag{1.17}$$

[4]The correct value of $A_{\rm P}$ is quite uncertain: de Vaucouleurs and Buta (1983) deduce $A_{\rm P} \approx 0.2$ from galaxy counts and reddening.

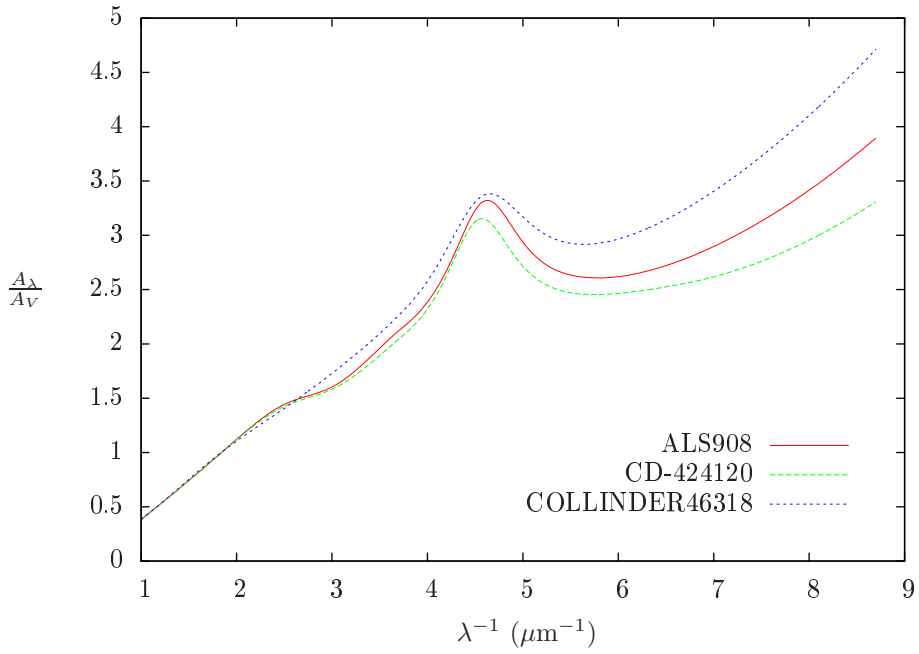

Figure 1.2: ISECs observed along three galactic different lines of sigth: ALS908, CD-424120 and COLLINDER46318.

where $x \equiv \lambda^{-1}$ in μm^{-1} and

$$D(x, x_0, x_1) = \frac{x^2}{(x^2 - x_0^2)^2 + x^2 x_1^2}. \tag{1.18}$$

These authors produced an estimate of the typical or average wavelength dependence of interstellar extinction. While the derivation is straightforward, the extent to which the properties of the average ISEC reflect the average properties of the Galactic extinction is problematic to define. As a consequence, it is difficult to derive a standard for Galactic dust. In turn this means that, in the same way, it is very hard to quantify how peculiar the nature of dust is along a line of sight whose extinction differs significantly from the average ISEC. Indeed, the shapes of the ISECs may simply reflect manifestations of dust grains in which particular physical/chemical properties are emphasised, leaving relatively unmodified the underlying global picture.

1.6 Dust in external galaxies

An important discovery in extragalactic astronomy was the identification of luminous IR galaxies: galaxies which emit more energy in the mid and far IR than all other wavelengths. The source of such emission is heated dust. The presence of dust in galaxies removes half or more of the stellar energy from the UV–optical range coming from the observed Universe and influences our understanding of galactic evolution. Using the IR Astronomical Satellite (IRAS) data, Soifer et al. (1987) showed that most

galaxies in the nearby Universe contain dust. More than one third of the bolometric luminosity of local galaxies is transferred by dust in IR. The fraction of stellar radiation reprocessed into the IRAS 8-120 μm window is around 25%–30%; including bolometric corrections from the IRAS window to the full IR range, the IR energy fraction becomes 35%–40% of the total bolometric energy within $\sim$ 100 Mpc. This average value could be subject to large variations between galaxies, depending on luminosity, morphological type and activity level (Calzetti, 2001).

Dust limits astronomers ability to know the local and distant Universe posing serious problems problems in the interpretation of the spectral energy distribution. Any accurate determinations of fundamental parameters, such as age, stellar population mix, star formation rates, and stellar Initial Mass Function are prevented. Moreover young stellar populations are more deeply embedded in dusty clouds than older stars, implying that a poor knowledge of the star formation history in galaxies. Finally, measuring the fraction of metals locked into dust at different epochs is is possible to trace chemical evolution of galaxies. The dust content of galaxies is proportional to both metallicity and gas content; as stellar population evolves in time and more gas is locked into stars, the metallicity of a galaxy increases while its gas contents decreases. Galaxies in the local Universe are only moderately opaque, and extreme values of the opacity are only found in the statistically non–dominant more active systems.

From multi–wavelength optical and near–IR imaging of edge–on or nearly edge–on systems indicate that the scale height of the dust is about half that of the stars, which means that the dust is more concentrated near the plane of the disk, and it appears more radially extended than the stellar distribution; the dust mass is found to be about an order of magnitude more than previously measured using the IRAS fluxes, indicating the existence of a cold dust component. The gas to dust mass ratio is close to the value derived for our Galaxy (Xilouris et al., 1999). IRAS 100 μm (Nelson et al., 1998) and ISO long wavelength maps (Radovich et al., 2001) confirm that cold dust emission extends beyond the limits of the optical disks along the radial direction, with scales that are $\sim$ 40% larger than those of B–band emitting stars, but still well within the HI disks.

Irregular galaxies have a lower metallicity than spiral galaxies: in irregular galaxies the mass in interstellar metals per unit L_B[5] is roughly 3 times smaller than in spiral galaxies.

Among local galaxies there is a special group of galaxies: starburst galaxies. The average UV and IR luminosities per unit comoving volume increase with redshift by roughly an order of magnitude up to z $\sim$ 1-2. Despite the heterogeneous set that UV-selected starbursts form, their dust reddening and obscuration properties are uniform. In these systems, the geometry of dust that best describes the reddening of the ionized gas emission is that of a foreground–like distribution. In starbursts region, internal dust doesn't appear to be present in large amounts, and the little present is likely to be in compact clumps (Calzetti et al., 1995) and the principal source of opacity appears to be given by dust that is external, or mostly external, to the starburst region, but still internal to the host galaxy, similar to a clumpy dust shell surrounding a central starburst.

We have some informations about the nature of dust in the nearest galaxies belonging to the local cluster. The local cluster includes $\sim$ 70 galaxies. The two most massive members of the cluster, the MWG and the Andromeda Galaxy (M31) have a system of satellite galaxies. Among the others are found the Small and Large Magellanic Clouds

[5] L_B is the luminosity in the blue filter.

(MCs), satellites of our own galaxy. The MCs and the M31 are the only external galaxies where so far it has been possible to study the extinction along lines of sight to individual stars.

- *Large Magellanic Cloud (LMC):* this galaxy is located at a distance of 50 kpc and it has an almost face–on viewing angle. It has metallicity at level 0.5 of the Milky Way ISM (Welty et al., 2001), and a dust to gas ratio is reduced by a factor 4 (Fitzpatrick, 1986). The total average star formation rate is relatively low as 0.26 $M_{\odot}yr^{-1}$ (Kennicutt et al., 1995), while the one of the MWG is $0.68-1.45\,M_{\odot}yr^{-1}$ (Robitaille and Whitney, 2010). These physical conditions are very similar to those of the early evolution of high redshift and metal poor galaxies. Stars more than ~ 500 pc away from the 30 Doradus region, a starburst region of LMC, show $R_V \approx 3.2$ with an extinction law resembling the MWG diffuse cloud extinction law (Misselt et al., 1999). In the 30 Doradus region the extinction law shows very different properties compared to the galactic average one. Indeed, as the figure (1.3) shows, the feature at 4.6 μm^{-1} is weakened and in the FUV a stronger rise than that common in the MWG is observable (Cartledge et al., 2005).

- *Small Magellanic Cloud (SMC):* this galaxy is located at 61 kpc away from the MWG and it is seen almost face–on from our galaxy. It has a dust to gas ratio reduced by a factor 10 with respect to the MWG (Bouchet et al., 1985). Its metallicity is 0.2× the MWG metallicity (Bernard et al., 2008). Observed ISECs for this galaxy are very different from the average curve for the MWG (see figure 1.3), indeed Gordon et al. (1997) discovered that UV extinction in SMC is very similar to that observed in starburst galaxies which have been detected from low to high ($z > 2.5$) redshifts. The *bump* strength is further diminished than ISECs for LMC or absent, as in AzV 18, and the rise in the FUV is further steep.

- *Andromeda Galaxy:* this is a spiral galaxy located at a distance of 750 kpc from the MWG and it has a metallicity very similar to that of our galaxy (Blair and Kirshner, 1985). For this galaxy we have poor informations but observed ISECs are more similar to the Galactic average one than typical interstellar curves of SMC and LMC; an important difference is that the *bump* strength is weaker in M31 than in MWG (Bianchi et al., 1996).

Accurate measurements of extinction curves are almost exclusively limited to the Galaxy, the LMC, and the SMC, because at greater distances it becomes impossible to obtain the photometry or spectroscopy of individual stars needed for extinction determinations. In the last decade observers have discovered huge quantities of interstellar dust near the most distant quasars in the very young universe, only 700 million years after primordial nucleosynthesis. Such studies (e.g., Jiang et al. 2006) indicate that high redshift quasar systems have been already enriched with dust up to a level comparable to nearby dusty galaxies. There is a vigorous debate and two distinct scenarios for the origin of dust at high redshifts, in which supernovae and lower-mass asymptotic giant branch stars are involved (see Section 1.3). What ever the case may be, dust exists at the highest redshifts probed so far ($z \sim 6$).

About two decades ago, quasars with damped Lyα systems in the foreground have been studied by Pei et al. (1991) and were found to be on average redder than those without. These authors found that the extinction curves in their sample of five quasars are not consistent with the Galactic extinction law, marginally compatible with the LMC

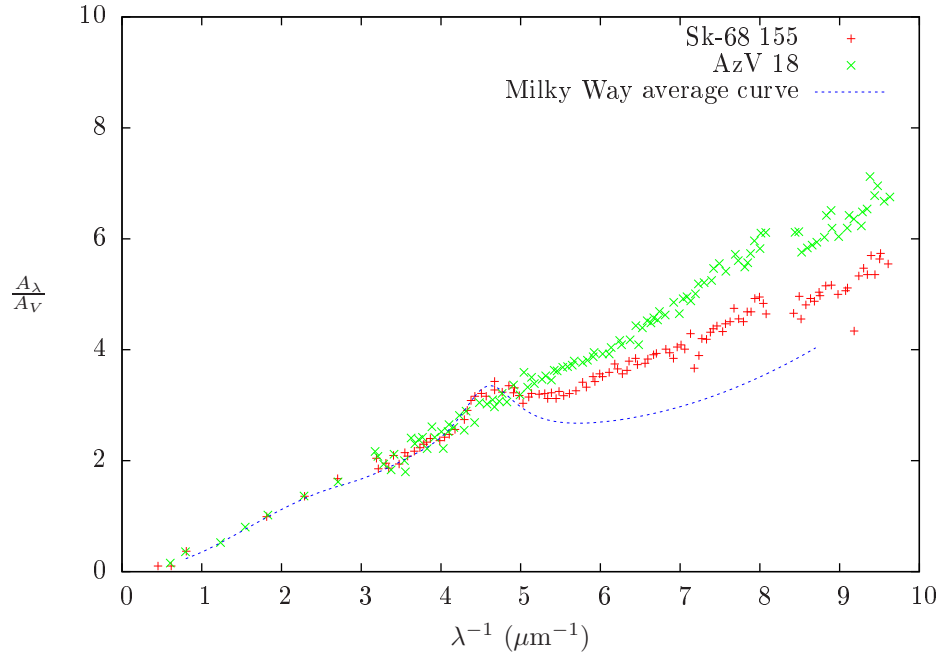

Figure 1.3: Average ISEC for the MWG (Fitzpatrick and Massa, 2007) compared to an ISEC observed in LMC near the 30 Doradus region (Sk-68 155) (Cartledge et al., 2005) and an interstellar extintion curve observed in SMC (AzV 18) (Cartledge et al., 2005).

extinction, and fully compatible with SMC extinction. Such findings were questioned by Murphy and Liske (2004) that found no trace of extinction. York et al. (2006) found no evidence of the 217.5 nm bump, and extinction curves similar to SMC extinction in a sample of quasars of the Sloan Digital Sky Survey. Extinction curves that differ from the SMC, LMC, and MWG have been obtained in the case of Active Galactic Nuclei (AGNs), although mildly reddened quasars appear to follow an SMC-like dust-reddening law (e.g., Hopkins et al. 2004). In the case of star-forming galaxies extinction curves are difficult to infer due to the crowding of dust with emitting sources. Starburst galaxies can be characterised by the lacking of the 217.5 nm absorption feature, like the SMC, and a steep far-UV rise, intermediate between those in the SMC and the MWG extinction curves. However, for UV luminous galaxies, the extinction curves range between those typical of the SMC and LMC, with some of them exhibiting weak bumps as in LMC (Noll and Pierini, 2005). In general, a significant 217.5 nm bump is observed in the spectra of star-forming galaxies at $z \sim 2$, indicating an LMC-like extinction curve (Noll et al., 2007). Chen et al. (2006) analysed the extinction curve for 10 Gamma Ray Burst (GRB) host galaxies, finding relatively flat and gray profiles, together with others displaying a close resemblance with MWG, but with no bump. Such inventory could be much longer, testifying a great variety of galactic environmental conditions.

1.7 Dust models

After first observations which highlighted the presence of interstellar dust in our galaxy, astronomers begin to develop interstellar dust models taking the cue from the observed interstellar extinction and the elemental depletions in the ISM. Current dust models trace their ancestry to the model of Mathis et al. (1977) (MRN from initials of authors' surname). Those authors assumed the existence of two distinct types of interstellar dust, graphite grains and silicate grains. All grains were assumed to be spherical and to have a continuous distribution of radii, a, from 5 nm to 250 nm, with the number of grains with radii in the range $a \rightarrow a + \mathrm{d}a$ being proportional to $a^{-3.5}$; i.e., there are very many more small grains than large. The calculations were performed using Mie theory (1908) and this model was successful in reproducing very well the average ISEC in the optical and UV. Many of the distinctive features of the Mathis et al. model are retained in more sophisticated models. There are too many models discussed in the recent literature for us to be comprehensive, so I shall focus on two examples of models that have some similarities and some differences.

1.7.1 Draine's model

Draine and his many collaborators have made the most comprehensive, consistent, and impressive developments of the MRN picture, and have applied their model to the widest range of observational tests with considerable success. Draine and Lee (1984) introduced optical functions for "astronomical silicate", derived for the olivine family of silicates from laboratory data in different wavelength regimes, pieced together in a manner consistent with the Kramers-Kronig relations but omitting any feature not observed in interstellar dust spectra. This approach has been widely adopted by others. The work of Draine and Lee (1984) was revised and also extended into the X-ray regime for both graphite and astronomical silicate by Draine (2003). Where the model is for spherical grains of uniform material the calculations were carried out by Mie theory.

A significant change to the MRN picture has been the assumption by many modellers that PAH molecules form an important additional component in the ISM, equivalent in some respects to very small grains. The potential importance of the PAH contribution to dust-related phenomena has been explored by Li and Draine (2001b), Weingartner and Draine (2001), Zubko et al. (2004), and more recently by Draine and Li (2007). The evidence supporting the inclusion of a PAH component is the widespread observation (especially by the *Spitzer* IR space mission) of the Unidentified Infrared Bands (so-called UIBs) between 3.3 and 12 μm. Many different models now incorporate a PAH component (using laboratory and theoretical opacities) whose abundance is adjusted to reproduce the observed strength of the UIBs. If they are present at this level, then PAHs will also contribute significantly to the "bump" and to the far UV extinction. Weingartner and Draine (2001) find that a trimodal carbonaceous grain size distribution is needed to match extinction curve, the UIBs, and IR emission - thus departing significantly from the simple power law distribution of the MRN model.

The model by Draine and collaborators has been applied to extinction in the MWG and other galaxies (Draine and Li, 2007), to IR emission including the dust-correlated microwave emission observed by COBE (Draine and Lazarian, 1998), and to polarization in the far-IR and submillimetre Draine and Fraisse (2009), and X-ray scattering (Draine and Tan, 2003). Calculations for non-spherical grains were made using the transition matrix method (Waterman, 1971) by Mishchenko and collaborators (Mishchenko and

Travis 1994, Mishchenko et al. 1997). The model does, however, appear to require excessive amounts of Mg, Si, and Fe, and also strains the abundance of carbon, leaving little available for the gas-phase carbon-bearing species C^+, C, and CO.

1.7.2 The Messina/Cagliari model

A model with significant differences from that of Draine and collaborators has been developed by researchers at Messina and Cagliari. The components of this model include "astronomical silicates", solid carbon, and PAHs, as in the Draine model; however, the carbon is assumed to be hydrogenated amorphous carbon containing both sp^2 (H-poor graphitic) and sp^3 (H-rich polymeric). A cavity is allowed to be present in the silicate cores, to mimic possible porosity and to relieve abundance constraints on silicon. Fifty types of PAHs are also included, and these are in neutral, cation, dication and anion forms, with opacities computed *ab initio* by Malloci et al. (2007). The most significant difference is that the carbon (other than the PAHs) is assumed to be deposited on the silicate cores, rather than as separate carbon grains. This description is suggested by the work of Jones et al. (1990) who argued that there is a cycle of carbon in the ISM; carbon is deposited on grains as H-rich sp^3 (polymeric) carbon, annealed to sp^2 (graphitic) carbon by the interstellar radiation field, and ultimately removed in shocks. A further difference from other models is that small and large grains are distinct sets rather than continuous; however, the $a^{-3.5}$ distribution applies to both small and large grains. This model can fit a wide variety of extreme MWG extinction curves, and also some unusual extinction curves from external galaxies. The differences between different lines of sight require changes to carbon layer, rather than to the underlying (refractory) silicates; thus they may be regarded as evolutionary changes. The model is thus very flexible without making drastic changes to fundamental parameters in the model.

Chapter 2

The model and its first application

2.1 The model in its simplified version

The model adopted in this thesis is the Cagliari/Messina core-mantle model (Iatì et al., 2008, Cecchi-Pestellini et al., 2008) presented in Section (1.7.2). Hereafter, such model will be termed [CM]^2. It is a bimodal model composed by a classical component, represented by a distribution of hollow silicatic core covered by double layered carbonaceous mantle, and by a molecular component, represented by a population of PAHs. The model has two versions differing only in the description of the molecular component: *i*) a superposition of two Lorentzians constructed to match the average spectral properties of PAHs (simplified version), *ii*) a linear combination of the PAH *ab initio* cross–sections (detailed version). In this chapter the simplified model is exploited, while the detailed version will be in introduced in Chapter 3.

The solid component is constructed assembling four concentric components (see figure 2.1): (*i*) a cavity, whose volume is in fixed proportion f_v for all core sizes, (*ii*) a silicate shell of radius a, (*iii*) a layer of HAC in graphitic form dominated by sp^2 bonding of thickness $f_{sp^2}w$, w being the mantle linear size, and (*iv*) the sp^3 layer of thickness $f_{sp^3}w = (1 - f_{sp^2})w$. The cavity and the silicate shell constitute the grain core, while the contiguous sp^2 and sp^3 layers the mantle.

The evolution of this model follows the prescription of Jones et al. (1990) (see Section 1.7.2): carbon atoms and ions are assumed to be deposited on dust grains, partially hydrogenated and retained on the surface. The newly deposited hydrogen–rich carbon is dominated by sp^3 bonding. Under the influence of the interstellar radiation field, this aliphatic carbon loses hydrogen and becomes more graphitic and aromatic, and is dominated by sp^2 bonding. Dust grains follow a MRN–like power law distribution: $(a + w)^{-q}$; the mantle width w is constant in the distribution and it is independent by the radius a of the grain (see Section 1.3).

As underlined above, in addition to the classic component we consider a population of PAHs. These molecules are carriers of the *bump* at 4.6 μm^{-1} and to the FUV rise of ISEC. In the simplified version of the model we describe PAHs contribution to the extinction in a similar way to Li and Draine (2001b): a double Lorentzian profile with the first lorentzian (centered at lower energy) which reproduces the $\pi^* \leftarrow \pi$ transition for PAHs and the second lorentzian reproduces the $\sigma^* \leftarrow \sigma$ resonance whose low energy tail contributes to the FUV rise.

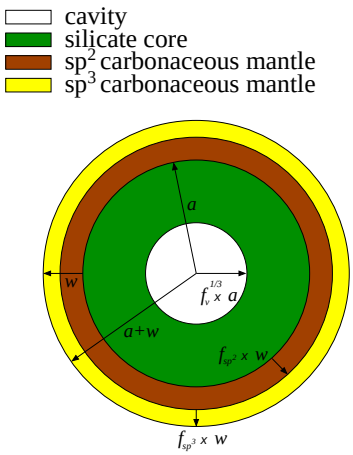

Figure 2.1: Grain representation according to our model: the hollow silicatic core is covered with a double layered carbonaceous mantle. The radius of the core and the thickness of the mantle are a and w, respectively. The radius of the cavity scales with the radius of the silicate shell according to the product $a \times f_v^{1/3}$, i.e. the cavity volume is in fixed proportions f_v with respect to the core volume for all core sizes. The widths of the sp^2 and sp^3 layers are $f_{sp^2} w$, and $f_{sp^3} w$, with the condition $f_{sp^2} + f_{sp^3} = 1$.

2.1.1 Classic component

To calculate optical properties of stratified grains composed by homogeneous layers with different refractive indices we use the extension of Mie theory 1908 to radially non–homogeneous spheres put forward by Wyatt (1962) as modified by Borghese et al. (1987) exploiting the T–matrix approach (Waterman, 1971). In the region external to the sphere the field is the superposition of incident and scattered fields. Both fields are expanded in a series of spherical vector multipole fields (Rose, 1957). The expansion of the incident field has to be regular at the origin, while the expansion of the scattered field has to satisfy the appropriate radiation conditions at the infinity (Jackson, 1975). We introduce a thin transition zone of width Δr at the interface between two contiguous layers, of refractive indexes n_i and n_{i+1}, in order to preserve the continuity of the refractive index and its radial derivative $n^2(\delta r) = n_i^2 + \left(3s^2 - 2s^3\right) \times \left(n_{i+1}^2 - n_i^2\right)$, with $s = \delta r / \Delta r$. Moreover, such a description accounts for the fact that the upper layer is actually formed by successive deposition of carbon atoms. Deposited atoms are initially adsorbed at the surface of the internal layer giving origin to a smooth transition from the properties of the internal layer to those of the external layer in formation. Optical constants used in the model are: Draine (1985) for silicatic core, Rouleau and Martin (1991), Be1 sample, for the sp^2 amorphous carbon, and Ashok et al. (1991) for the sp^3 polymeric carbon.

The grain size distribution follows the MRN model, but, in addition, the [CM]^2 model provides the possibility to divide the dimensional spectrum in two populations: *i*) a population of small grains and *ii*) another population of large grains. Both these two populations follow the same power law, and there is no qualitative difference between the two populations, whose components have the same structure described by the same parameters. Each population is characterised by lower and upper size limits in the distribution

Summing up, the parameters of the dust grain component of the extinction model are the following:

a_- lower limit of the "small" grain component

a_+ upper limit of the "small" grain component

b_- lower limit of the "big" grain component

b_+ upper limit of the "big" grain component

q exponent of the MRN power law size distribution

f_v vacuum fraction of silicate core

w total carbonaceous mantle thickness

f_{sp^2} fraction of sp^2 material of the carbonaceous mantle width

N_d normalisation factor of the size distribution, proportional to the total amount of dust grains.

In reality, N_d is not a true free parameter: because of the normalization to the visual extinction N_d is proportional to the inverse of the average (over the size distribution) extinction cross-section computed at $\lambda = \lambda_V$ (equation 2.15). The above parameters are subject to a number of physical constraints, namely: $5\,\mathrm{nm} \leq a_- \leq a_+ \leq b_- \leq b_+ \leq 1000\,\mathrm{nm}$, $0 \leq f_v \leq 1$, $0 \leq f_{sp^2} \leq 1, 0\,\mathrm{nm} \leq w \leq 3\,\mathrm{nm}$, and $N_d \geq 0\,\mathrm{nm}^{(q-3)}$. We impose an upper limit $w \leq 3$ nm on the mantle thickness in order to avoid an unreasonable amount of carbon atoms locked in dust mantles[1].

The present dust model, including only spherically symmetric particles, does not account for polarization effects, which require some kind of anisotropy. However, our purpose is to consider accurately the effect of layers with different optical properties on a grain, and to consider such effect in the description of observed ISECs. We might also apply some kind of correction, e. g., to arbitrarily assume that dust grains are approximately oblate spheroids (Mathis, 1996). Still, the shape of dust grains is unknown, except to the extent that it departs from a sphere. Thus, adding any correction for non–spherical particles would imply some additional arbitrary choice, while adding little in the way of our scope, i. e. modelling extinction curves and relating their variations to physical quantities in a uniform way. We therefore choose to stick to spherical symmetry for classical dust grains.

Figure (2.2) shows extinction efficiencies calculated for single particles with different size: $a = 5$, 100, 500 and 1000 nm varying mantle width, void fraction and sp^2 fraction. The extinction efficiency depends on the optical cross–section σ and the geometrical cross–section with the following law:

$$Q_{ext}(\lambda^{-1}, a) = \frac{\sigma(\lambda^{-1}, a)}{\pi(a + w)^2} \tag{2.1}$$

[1] As we see in the next Chapters, such artificial limit is useless and will be relaxed in subsequent calculations. We find that the maximum mantle thickness is approximately 6 nm, see equation (4.5)

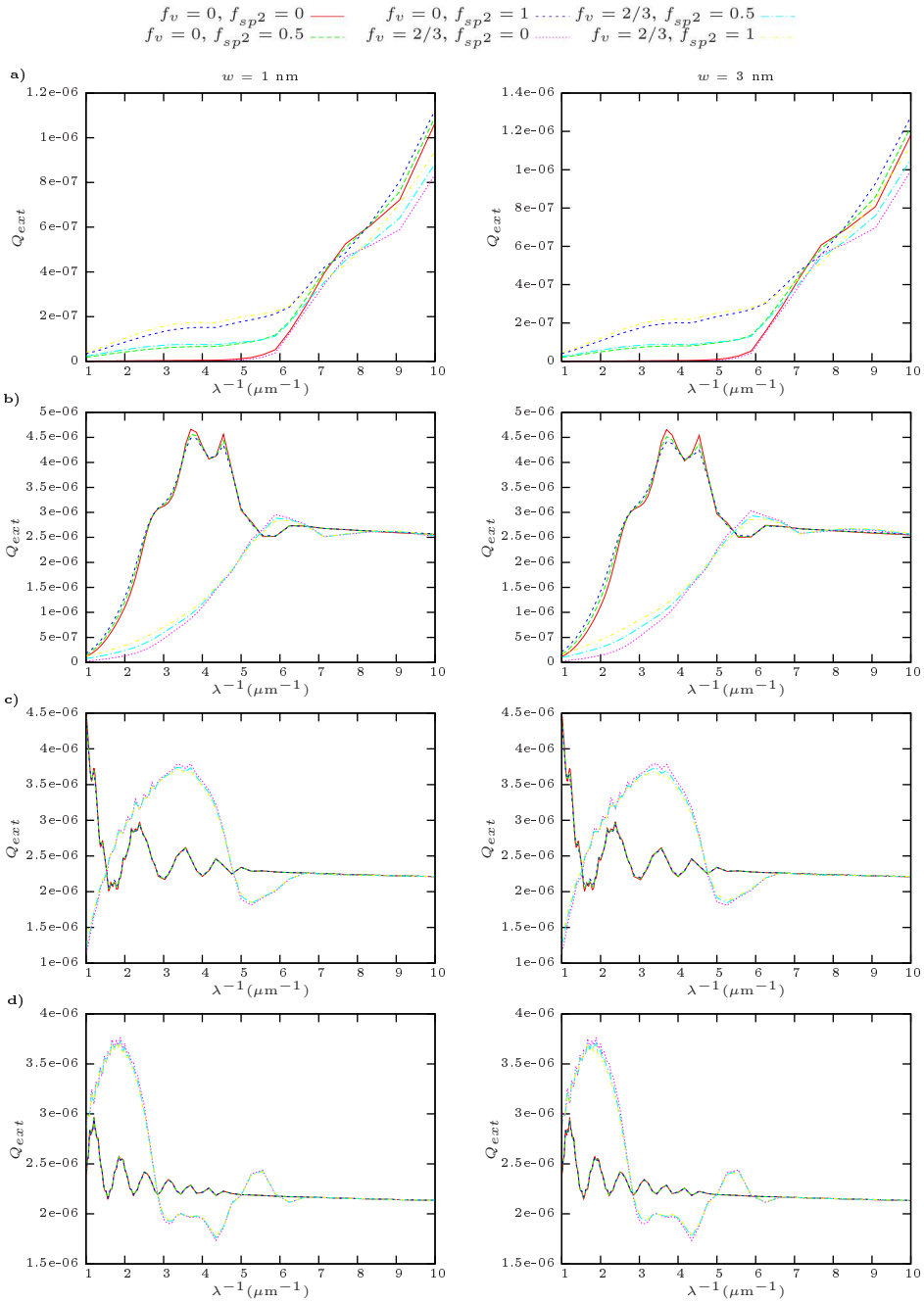

Figure 2.2: Extinction efficiency vs wavenumber for different particle sizes, mantle width $w = 1$ nm (left panel) and $w = 3$ nm (right panel) varying void fraction f_v and linear fraction sp^2 material f_{sp^2} on the mantle width. Letters indicate different particle size: two figures with **a)** show extinction efficiency for particles with radius $a = 5$ nm, **b)** for radius $a = 100$ nm, **c)** for radius $a = 500$ nm and **d)** for radius $a = 1000$ nm

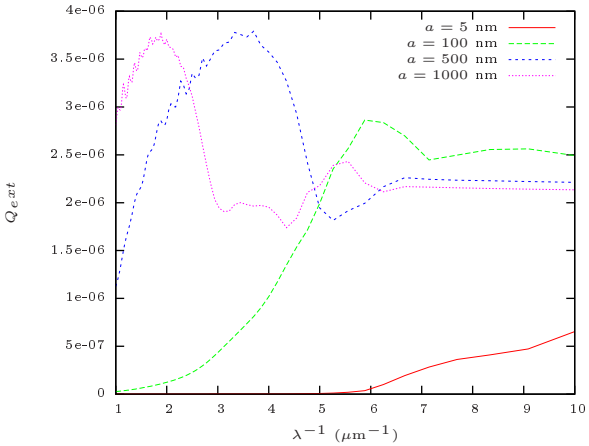

Figure 2.3: Extinction efficiencies for bare silicate grains. The void fraction is 2/3.

Particle without mantle (silicate only) are considered in figure (2.3) which highlights as the extinction is higher at wavelength similar to the size of extinguishing particle: for $a = 5$ nm extinction efficiency rises for higher wavenumber and the maximum is outside the plot, instead the maximum of extinction efficiency is visible in figure (2.3) for particles with size $a = 100$, 500 and 1000 nm, at smaller wavenumber for larger grain size.

In figure (2.4) for different particle sizes is showed, the albedo is defined as the ratio between scattering efficiency and extinction efficiency:

$$\omega = \frac{Q_{sca}}{Q_{ext}}. \tag{2.2}$$

Usually ω varies between 0 and 1; in figure (2.4) albedo is minor 1, so dust scatters and also absorbs stellar radiation.

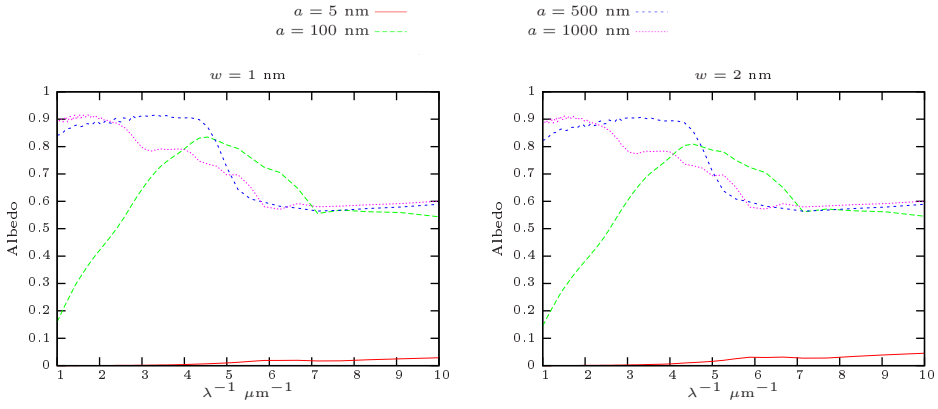

Figure 2.4: Albedo vs wavenumber for different particle sizes. The mantle width $w = 1$ nm (left panel) $w = 2$ nm (right panel), void fraction $f_v = 2/3$, and sp^2 fraction $f_{sp^2} = 1/2$.

To understand as extinction varies with the size distribution we consider an MRN profile ($a^{-3.5}$) and we calculate the average cross–section normalized to its value in the visible:

$$\frac{\langle\sigma(\lambda^{-1})\rangle}{\langle\sigma_V\rangle} = \frac{\int_{\Delta a}\sigma(\lambda^{-1},a)a^{-3.5}\mathrm{d}a}{\int_{\Delta a}\sigma_V(a)a^{-3.5}\mathrm{d}a} \tag{2.3}$$

where δa is the integration range. Figure (2.5) shows average normalized cross–sections for continue dimensional distributions with limits $5-1000$ nm, $5-500$ nm and $500-1000$ nm, fixed void fraction and sp^2 fraction, varying the mantle width. Figure (2.5) highlights that the distribution with the higher low limit, $a = 500$ nm, shows cross–sections with a very different trend compared to other distributions plotted on figure (2.5). This fact is due by the presence of only large grains which extinguish preferentially in the range of small wavenumber. We can also see that, for this kind of distribution, cross–section does not depend by the mantle width as we expect because $w \ll a$ for all sizes.

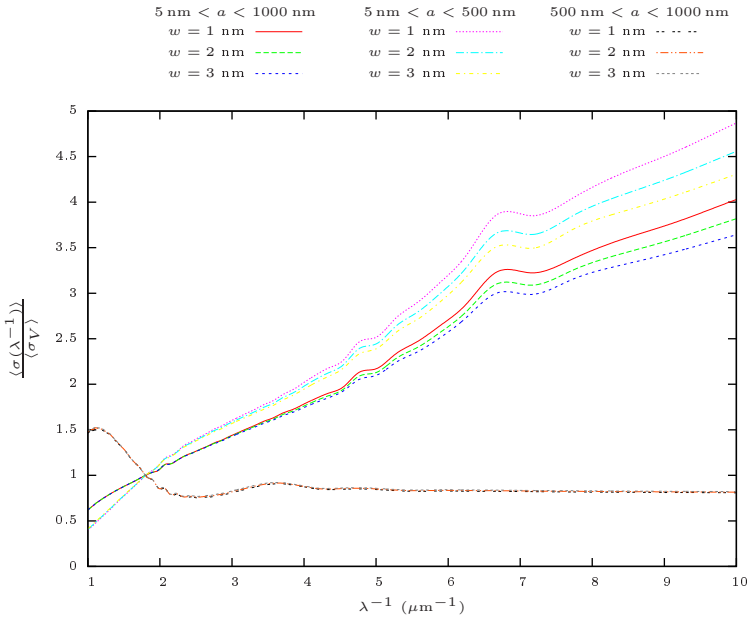

Figure 2.5: Average cross–sections for different distributions of classical particles normalized to their value in the visible. These cross–sections are calculated for dimensional distributions: $5-1000$ nm, $5-500$ nm and $500-1000$ nm; for different values of mantle width w and with void fraction f_v and sp^2 mantle fraction f_{sp^2} fixed respectively to 1/3 and 1/2.

2.1.2 PAHs

The presence of a molecule–sized component of carbonaceous dust was inferred as far back as the first observations of the 3.3 μm emission band became available. Sellgren (1984) showed that this emission would require unrealistically large temperatures, if arising from dust in thermal equilibrium[2]. Soon afterwards, Leger and Puget (1984) and

[2] see, however, Duley and Williams (2011) for a different interpretation.

Allamandola et al. (1985) discovered that the whole group of correlated emission bands at 3.3, 6.2, 7.7, 8.6, and 11.3 μm (see Section 1.3) matched the main IR bands of the family of PAHs. These molecules are known to efficiently convert electronic excitation, due to the absorption of UV–visible photons, into vibrational excitation, and then IR emission, and are very photo–stable. Their contribution to extinction is energetically consistent with the observed emission in the above set of IR bands: AIBs. Nonetheless, to date no specific PAH has been identified with certainty. AIBs are highly non–specific, being essentially due to vibrations of functional groups inside the molecules. Far–IR features involving vibrations of the whole molecule can distinguish individual species, but none were detected so far in Herschel data. Similarly, $\pi^\star \leftarrow \pi$ electronic transitions of neutral PAHs can be narrow and specific enough to permit an identification, but none were detected despite targeted observations (see e. g., Clayton et al., 2003). They could be also the carriers for the observed Diffuse Interstellar Bands (DIBS)[3]. The constraints that PAHs as a family must be abundant enough to produce the observed AIBs intensities (containing at least $\sim$10% of the available interstellar carbon atoms), and that no single one be abundant enough for its weak individual spectral signature to stand out, were interpreted to point to very large chemical diversity, with (at least) hundreds of different PAH species in the interstellar mixture.

In this work we consider a population of PAHs as a possible candidate to be the carrier of the observed *bump* at 4.6 μm^{-1} and of the FUV rise in the ISEC. Figure (2.6) shows the structure for two molecules of PAHs: pyrene and coronene. The coronene was considered as possible candidate for DIBs (Duley 2006a,b).

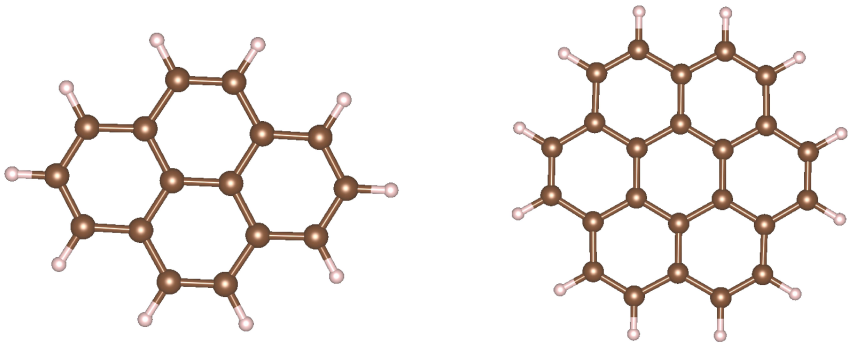

Figure 2.6: Two PAHs: in the left panel the structure of the ground state for the pyrene molecule, in the right panel the structure for the coronene molecule.

PAHs extinction reads as follows

$$\sigma_{PAH}(\lambda^{-1}) = \sigma_0 \times \left[L_\pi(\lambda^{-1}, \lambda^{-1}_{\rm peak}, \gamma) + \mathcal{R} L_\sigma(\lambda^{-1}, \lambda^{-1}_{\rm peak}, \gamma) \right] \tag{2.4}$$

where

$$L(\lambda^{-1}, \lambda^{-1}_{\rm peak}, \gamma) = \frac{\sqrt{b_2}}{(\lambda^{-1} - b_1)^2 + b_2}, \quad \gamma = 2\sqrt{b_2}, \quad \lambda^{-1}_{\rm peak} = b_1, \tag{2.5}$$

[3]DIBs are molecular absorption profiles observed in the visible range along lines of sight through diffuse clouds whose carriers are not yet well identified.

γ is the Lorentzian Full Width Half Maximum (FWHM), $\mathcal{R}$ is the ratio between the intensity of L_σ and L_π, and

$$\sigma_0 = \int \sigma_{\rm PAH}(\lambda^{-1})\mathrm{d}(\lambda^{-1}) / \left[\frac{\pi}{2} \times (1+\mathcal{R})\right]. \tag{2.6}$$

To obtain the formula of PAHs extinction approximated with a double lorentzian profile, we must start from the optical depth of a PAHs mixture:

$$\tau_{\rm PAH}(\lambda^{-1}) = \int_{\delta L} \sigma_{\rm PAH}(\lambda^{-1}) n_{\rm PAH}(s)\mathrm{d}s \tag{2.7}$$

where δL is the PAHs absorption path along the line of sight, and $n_{\rm PAH}(s)$ is their volume density at a location s in the line of sight. Then equation (2.7) becomes:

$$\tau_{\rm PAH}(\lambda^{-1}) = \sigma_{\rm PAH}(\lambda^{-1}) N_{\rm PAH}, \quad N_{\rm PAH} = \int_{\Delta L} n_{\rm PAH}(s)\mathrm{d}s \tag{2.8}$$

where $N_{\rm PAH}$ is the PAHs column density in the line of sight. Exploiting the relation between optical depth and extinction $A(\lambda^{-1}) = 1.086\,\tau(\lambda^{-1})$ (Whittet, 2002)

$$A_{\rm PAH}(\lambda^{-1}) = 1.086 \sigma_0 N_{\rm PAH} \times \left[L_\pi(\lambda^{-1}, \lambda^{-1}_{\rm peak}, \gamma) + \mathcal{R} L_\sigma(\lambda^{-1}, \lambda^{-1}_{\rm peak}, \gamma)\right] \tag{2.9}$$

The relationship between A_V and the hydrogen column density is given in the equation (1.12) and the equation (2.9) becomes:

$$\left[\frac{A(\lambda^{-1})}{A_V}\right]_{\rm PAH} = \frac{6.41 \times 10^{21} \sigma_{\rm PAH}(\lambda^{-1}) N_{\rm PAH}}{R_V N_{\rm H}} = \frac{6410}{R_V}\left(\frac{N_{\rm PAH}}{N_{\rm H}}\right)\left[\frac{\sigma_{\rm PAH}(\lambda^{-1})}{\rm Mb}\right]. \tag{2.10}$$

Defining the PAHs fractional abundance as $f_{\rm PAH} = N_{\rm PAH}/N_{\rm H}$, the equation (2.10) can be written in this form:

$$\left[\frac{A(\lambda^{-1})}{A_V}\right]_{\rm PAH} = \frac{6410}{R_V} f_{\rm PAH}\left(\frac{\sigma_0}{\rm Mb}\right) \times \left[\frac{\sqrt{b_2^\pi}}{(\lambda^{-1} - b_1^\pi)^2 + b_2^\pi} + \mathcal{R}\frac{\sqrt{b_2^\sigma}}{(\lambda^{-1} - b_1^\sigma)^2 - b_2^\sigma}\right]. \tag{2.11}$$

This is the PAHs contribution to the extinction as considered in the simplified version of the [CM]^2 model. To validate this approximation we fitted such semi–empirical cross–section with the average cross–section of 54 PAHs obtained averaging on the carbon atoms number which each of 54 PAHs contains. These cross–sections were calculated by Malloci et al. (2007). Further details are given in Section (3.3). Figure (2.7) shows these fits for PAHs in different charge states: anions, neutrals, cations and dications. To obtain these fits we need to introduce an exponential cut–off in the low energy tail of L_σ: $e^{-(\frac{\Lambda}{\lambda^{-1}})}$. The result is a damping in the low energy tail of L_σ from $\lambda^{-1} \simeq 10\ \mu\mathrm{m}^{-1}$. In the Chapter 3 we slightly change this exponential damping factor to $1/\{1 + \exp[(C_1 - \lambda^{-1})/C_2]\}$ (see Section 3.2)

The parametrization of Fitzpatrick and Massa (2007) (see Section 1.5) includes a quadratic function of λ^{-1} with a threshold at $5-7\ \mu\mathrm{m}^{-1}$, varying with the observed line of sight, to reproduce the FUV rise of the ISEC. For minor wavenumber the component which causes the FUV rise has no effects. At $\lambda^{-1} \simeq 6\ \mu\mathrm{m}^{-1}$ the damping factor produces A decrease of about one order of magnitude compared to the natural value of

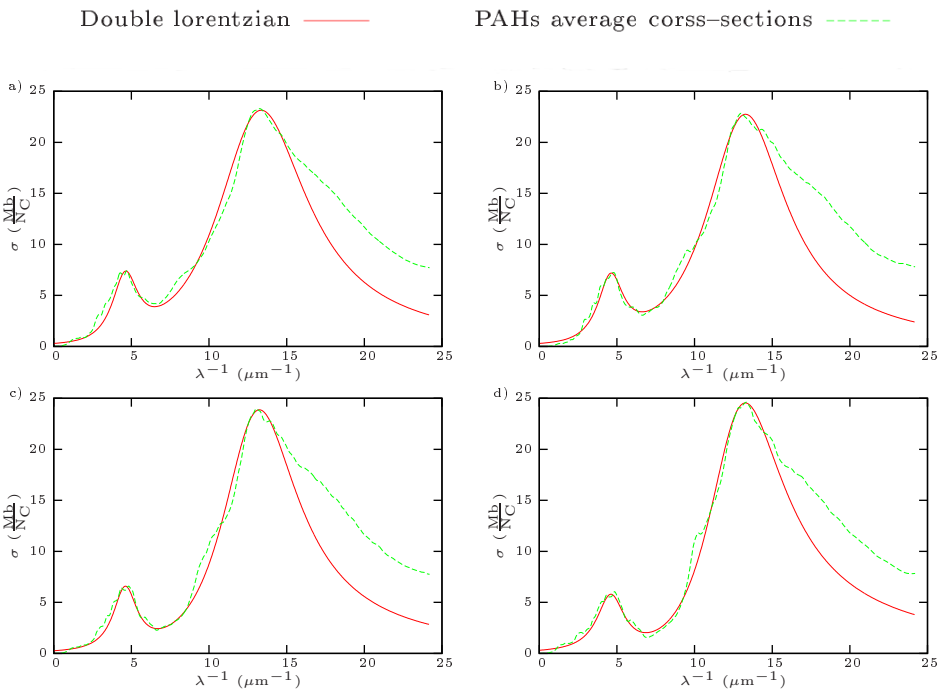

Figure 2.7: Comparison between average cross–sections of 54 PAHs per carbon atoms number and double lorentzian with variable parameters (see table 2.1). a) is the plot for anions, b) for neutral, c) for cations and d) for dications.

L_σ, proving that PAHs photo–absorption cross–sections have a trend which differs from a unadulterated lorentzian profile in the FUV. This trend is consistent with the observed one in the ISEC in this spectral range. Although the cut–off fluctuates for different lines of sight the peak position and width of the bump do not suffer great variations. Thus, changes in the FUV must affect moderately the region around 4.6 μm^{-1}. The presence of the cut–off in L_σ mimics the intrinsic behaviour of PAHs poto–absorption cross–sections. In table (2.1) are reported the parameters derived fitting PAH average cross–sections shown in figure (2.7). From this figure it is evident that the high energy tail of L_σ does not reproduce the exact trend of real cross–sections. Luckily, this range is not important because of the lack of appreciable interstellar radiation fields beyond the Lyman continuum.

Summarizing, parameters of the simplified molecular component are:

b_1^π peak wavenumber of the first Lorentzian

b_2^π Full Width at Half Maximum (FWHM) of the first Lorentzian

b_1^σ peak wavenumber of the second Lorentzian

b_2^σ FWHM of the second Lorentzian

λ cut–off scale.

	Anions	**Neutral**	**Cations**	**Dications**
b_1^π	4.6	4.6	4.6	4.6
b_2^π	1	1	0.9	1.2
b_1^σ	13	13	12.8	12.6
b_2^σ	13	10	9	9
Λ	10	10	17	25
σ_0	6.5	6.5	4.7	6.3
$\mathcal{R}$	98.4	74.6	138.6	221.9

Table 2.1: Parameters used in double lorentzians to fit average cross–sections computed by Malloci et al. (2007). b_1^π, b_1^σ and Λ are expressed in μm^{-1}, b_2^π and b_2^σ are expressed in μm^{-2}, σ_0 is the average cross–section in Mb μm^{-1} per carbon atom and $\mathcal{R}$ is the scaling factor of L_σ and it is dimensionless.

$\mathcal{R}$ the L_σ scaling factor

These parameters also are constrained to be physically sensible, i. e. $b_2^\pi \geq 0\,\mu^{-1}$, $b_2^\sigma \geq 0\,\mu^{-1}$,$b_1^\pi \leq b_1^\sigma$, $\lambda \geq 0\,\mu^{-1}$, $\mathcal{R} \geq 0$.

2.2 The sample selection

Our intention is to investigate those ISECs, parametrized by Fitzpatrick and Massa (2007) (Section 1.5), "the farthest possible" from the average ISEC, in order to derive, in the framework of the present dust model, dust morphology and chemical compositions, and compare them with the ones characteristic of the average ISEC. To select such curves we define an euclidean distance in the 8–dimensional space generated by the 7 parameter description of Fitzpatrick and Massa (2007) in the UV, and by R_V, the ratio of total–to–selective extinction, that we consider to be a "measure" of an extinction curve in the VIS/IR. Point coordinates in this space are defined by taking the difference δ_k between the $k-$th parameter ($k = 1, \cdots, 8$) of an ISEC and the corresponding one of the average ISEC. δ_k's are then ordered on a discrete (natural) scale depending on their values. In other words, for a given line of sight each δ_k is given a value ranging from 1 to 328, according to its placement in the ranking of increasing distance of the k^{th} parameter from the reference value in the average Galactic curve. In this representation, the ISEC nearest to the average ISEC is BD+58 2292, while the farthest is HD37130 (cf Fitzpatrick and Massa 2007 for the data).

From the resulting ordering, suitable curves are extracted to obtain a set as variegated as possible, in which particular characteristics are highlighted, such as e.g., a low bump or a very steep UV rise. Eventually, we selected a sample of 15 curves. The list is reported in table (2.2), in order of increasing distance from the average ISEC. From the selection procedure are, however, excluded ISECs that appear to be pathological. For example, VCT 10 shows an unphysical dip between 2 and 4 μm^{-1} (Fitzpatrick and Massa, 2007), hinting calibration problems in the data might be present.

2.3 Results

In the [CM]^2 model the extinction curve along a particular line of sight is given by the relation (subscript c indicates classical dust)

$$\frac{A(\lambda^{-1})}{A_V} = \frac{A_c(\lambda^{-1})}{A_V} + \frac{A_{\rm PAH}(\lambda^{-1})}{A_V}, \tag{2.12}$$

For classical dust grains we obtain (cf. Draine and Lee 1984)

$$\frac{A_c(\lambda^{-1})}{A_V} = \frac{6.41\times10^{21}}{R_V}\left(\frac{\mathcal{K}}{n_{\rm H}}\right) I_f(\lambda^{-1}), \tag{2.13}$$

$n_{\rm H}$ is the hydrogen number density, and $\mathcal{K}$ a normalization constant such that $\langle n_c\rangle$ is the classical dust number density averaged over the dust size distribution $f(a+w)$

$$\langle n_c\rangle = \mathcal{K}\int_{a_-}^{a_+} f(a+w)\,{\rm d}a \tag{2.14}$$

where a_- and a_+ are the lower and upper values in the size distribution of the classical dust. The wavelength–dependent factor, proportional to to the average extinction cross–section of the classical dust, is given by

$$I_f(\lambda^{-1}) = \int_{a_-}^{a_+} \sigma_c(a+w, f_v, f_{sp^2}, f_{sp^3}, \lambda^{-1})\, f(a+w)\,{\rm d}a, \tag{2.15}$$

where $\sigma_c(a+w, f_v, f_{sp^2}, f_{sp^3}, \lambda^{-1})$ is the extinction cross–section of classical grains, computed with the methods described in Iatì et al. (2008).

line of sight	model	$R_V^{(a)}$	$\mathcal{C}_c$ nm$^{q-3(c)}$	$\mathcal{C}_{\rm PAH}$ μm^{-1}	$\delta^{(b)}$
CPD-59 2574	1	3.70	0.70	0.369	0.534
HD21483	2	2.83	1.35	0.660	0.547
BD+56 518	3	2.58	0.71	0.713	0.594
CPD-59 4549	4	3.23	1.25	0.575	0.645
HD13659	5	2.49	0.68	0.564	0.767
HD197512	6	2.43	1.15	0.830	0.769
HD99872	7	2.97	2.50	0.847	0.791
HD29647	8	3.46	0.90	0.620	0.795
HD151346	9	3.81	1.18	0.796	0.888
HD62542	10	2.74	0.38	0.756	0.898
HD294264	11	5.48	1.12	0.320	0.899
HD180968	12	2.90	0.70	0.889	0.909
HD197702	13	4.40	1.01	0.690	0.939
HD23512	14	3.20	3.19	0.749	0.942
HD37130	15	5.50	1.10	0.147	1.000

(a) Fitzpatrick and Massa (2007); (b) normalized to its maximum value; (c) q is reported in table (2.3).

Table 2.2: Fitting scaling parameters from eq.(2.20).

The total PAH extinction cross–section is given by the superposition of L_π and L_σ with an exponential damping factor on the low energy side of L_σ

$$\frac{A_{\rm PAH}(\lambda^{-1})}{A_V} = \frac{3.81\times10^4\, f_{\rm PAH}\mathcal{N}_{\rm C}}{R_V}\left[L_\pi + \mathcal{R}{\rm e}^{-(\Lambda/\lambda^{-1})}L_\sigma\right] \tag{2.16}$$

$\mathcal{N}_{\rm C}$ is the average number of carbon atoms per PAH molecule. Similar representations have been put forward by e.g., Li and Draine (2001a) and Duley (2006a). A possible interpretation in terms of properties of specific PAHs is given in Duley (2006a).

Finally, we derive the mass balance in terms of the number of silicon and carbon atoms (parts per million, ppm) locked in grains and PAHs. We first consider the classical component. The silicate cores have a mass per unit volume given by

$$n_{\rm Si}\, m_{\rm Si} = \frac{4\pi\rho_{\rm Si}}{3} \times \mathcal{K}\, J_f^{(1)}\ (1-f_v)\,, \tag{2.17}$$

where $n_{\rm Si}$ is the number density of silicon atoms, $m_{\rm Si}$ the mass of a silicate molecule, $\rho_{\rm Si}$ the mass density of the astronomical silicate, and

$$J_f^{(1)} = \int_{\Delta a} a^3 f(a+w)\,{\rm d}a. \tag{2.18}$$

Evaluating eq.(2.13) for $\lambda^{-1}=\lambda_V^{-1}$ we derive

$$\frac{\mathcal{K}}{n_{\rm H}} = \frac{r_c R_V}{6.41\times10^{21}\, I_f(\lambda_V^{-1})}, \tag{2.19}$$

where r_c is the fractional contribution to visual extinction of classical dust. The fraction r_c can be derived through the fitting procedure

$$\left[\frac{A(\lambda^{-1})}{A_V}\right]_{\rm obs} = \mathcal{C}_c \times I_f(\lambda^{-1}) + \\ + \mathcal{C}_{\rm PAH} \times \left[L_\pi + \mathcal{R}{\rm e}^{-(\Lambda/\lambda^{-1})}L_\sigma\right]. \tag{2.20}$$

Substituting eq.(2.19) into eq.(2.17) we find

$$\left(\frac{n_{\rm Si}}{n_{\rm H}}\right)\ {\rm ppm} = 6.53\times10^{-16}\,\frac{\rho_{\rm Si}}{m_{\rm Si}}\frac{r_c\, R_V\, J_f^{(1)}}{I_f(\lambda_V^{-1})}\ (1-f_v)\,. \tag{2.21}$$

In a similar way the number of carbon atoms locked in classical grains results

$$\left(\frac{n_{\rm C}}{n_{\rm H}}\right)_g\ {\rm ppm} = 6.53\times10^{-16}\,\frac{r_c\, R_V\ \left(\rho_3 J_f^{(3)} + \rho_2 J_f^{(2)}\right)}{m_{\rm C}\, I_f(\lambda_V^{-1})}, \tag{2.22}$$

where the geometrical factors $J_f^{(2)}$ and $J_f^{(3)}$ read as

$$J_f^{(2)} = \int_{\Delta a}\left(a + f_{sp^2} w\right)^3 f(a+w)\,{\rm d}a - J_f^{(1)}, \tag{2.23}$$

$$J_f^{(3)} = \int_{\Delta a}(a+w)^3\, f(a+w)\,{\rm d}a - J_f^{(2)} + J_f^{(1)}, \tag{2.24}$$

$m_{\rm C}$ is the mass of a carbon atom, and ρ_2 and ρ_3 are the mass densities of the sp^2 and sp^3 mantle components, respectively.

model	core/mantle particles								(Si/H)	(C/H)		PAHs						(C/H)
	small		large							small	large	$\pi - \pi^\star$		$\sigma - \sigma^\star$				
	a_-	a_+	a_-	a_+	w	q	f_v	$f_{sp}2$				b_1^π	$\sqrt{b_2^\pi}$	b_1^σ	$\sqrt{b_2^\sigma}$	Λ	$\mathcal{R}$	
	nm								ppm			$\mu\mathrm{m}^{-1}$						ppm
$0^{(a)}$	5	13	80	440	1.2	3.53	0.50	0.97	34	23	12	4.58	0.41	16.0	1.22	1.6	266	37
$1^{(b)}$			80	450	1.0	3.53	0.10	0.00	37		3	4.59	0.47	15.8	3.46	2.1	211	36
2			80	250	2.5	3.60	0.00	0.75	23		1	4.65	0.66	16.0	3.32	2.5	148	49
3	5	11	120	300	1.0	3.70	0.35	1.00	5	6	< 1	4.58	0.51	24.7	6.20	2.1	350	49
4	5	15	80	600	2.5	3.53	0.54	1.00	36	41	25	4.59	0.42	16.0	5.11	2.1	48	49
5			88	300	3.0	3.50	0.00	1.00	19		11	4.65	0.59	19.4	1.00	3.5	1522	37
6	5	12	44	260	1.3	3.53	0.01	0.94	37	12	16	4.56	0.50	16.9	2.00	4.0	190	53
7			120	275	1.0	3.65	0.09	0.80	25		4	4.59	0.52	17.0	4.00	2.0	77	66
8			80	330	< 1	3.56	0.01		31		< 1	4.75	1.10	15.2	3.20	2.0	107	57
9			80	350	2.6	3.57	0.07	0.97	40		19	4.57	0.74	14.0	1.34	2.4	123	80
10			80	310	< 1	3.43	0.08		18		< 1	4.75	1.10	12.8	2.86	2.0	88	55
11			120	500	1.3	3.53	0.10	1.00	77		17	4.59	0.69	30.5	4.47	3.0	441	46
12			180	420	3.0	3.50	0.25	0.00	16		3	4.67	0.66	25.6	1.24	3.0	1432	67
13			180	460	2.8	3.50	0.18	1.00	43		16	4.62	0.60	25.5	0.95	3.3	1615	80
14			180	300	2.9	3.56	0.40	1.00	26		17	4.55	0.77	14.7	1.00	3.0	333	63
15			120	500	2.7	3.53	0.30	1.00	60		32	4.75	0.71	20.5	2.98	1.5	475	20

(a) average ISEC from Cecchi-Pestellini et al. (2010); (b) see table (2.2).

Table 2.3: Parameters and derived silicon and carbon masses from the fitting procedure for the ISECs reported in table (2.2).

The number of carbon atoms incorporated in PAHs can be derived by combining eqs.(2.20) and (2.16)

$$f_{\rm PAH}\,\mathcal{N}_{\rm C} = \frac{R_V\,\mathcal{C}_{\rm PAH}}{3.81\times10^4}, \tag{2.25}$$

leading to

$$\left(\frac{n_{\rm C}}{n_{\rm H}}\right)_{\rm PAH}\ {\rm ppm} = 26\,R_V\,\mathcal{C}_{\rm PAH}. \tag{2.26}$$

The mass budget has been derived assuming that dust and gas are well–mixed, with the density of dust proportional to the density of gas, i.e equation (1.12) applies.

We assume also the mass densities, $\rho_{\rm Si} = 3.3$ g cm^{-3} (Laor and Draine, 1993), $\rho_2 = 2.26$ g cm^{-3} (Laor and Draine, 1993), and the $\rho_3 = 0.901$ g cm^{-3} (polyethylene density). Silicate cores have radii in the range $5 - 1000$ nm, while the carbon mantle thickness is limited to be $w \leq 3$ nm.

The results of the non–linear fitting procedure have been reported in tables (2.2) and (2.3), while in figure (2.8) are shown the resulting synthetic extinction curves compared with the observational data.

The fits to the ISECs in our sample by the adopted model are excellent. This is partly due to the intrinsic shapes of the PAH extinction cross–sections, as they appear to be naturally fitted to reproduce the experimental values (see e.g., Joblin et al. 1992 and Malloci et al. 2007). The model adopted, despite the apparently large number of free parameters, is far from being infinitely flexible. Indeed, the present representation would be totally unable to match the data if, e.g., extinction curves would decrease in the far–UV, because many parameters are controlling the extinction properties of the mixture within a "stiff" class of morphological profiles. The visible part of the extinction curve is mainly produced by the large size part of the dust distribution, while the UV rise is due to the contribution of small grains and PAHs floating on top of the flat, saturated, extinction of the large ones.

When present, small grains contribute with a non–linear profile to the FUV rise. As in the case of the average ISEC, large grain sizes are mostly in the range $80 - 500$ nm. The upper size limit is poorly unconstrained by the fit, since synthetic extinction curves are almost insensitive to the large end tail of the dust size distribution in the wavelength range covered by Fitzpatrick and Massa (2007). The parameter value obtained in the fit thus means that particles at least up to that size are necessary, but still larger ones are not excluded. A better determination of this parameter requires additional observational constraints. The required vacuum fraction of the core volume is $f_v \leq 0.5$. In two cases, models 8 and 10, the mantle widths and their chemical compositions are not well determined, because the mantle thicknesses result lower than 1 nm. For such small values classical electromagnetic calculations became unreliable. There is, however, in general a moderate insensitivity of the fits to mantle thickness and, consequently to mantle chemical composition, because of the large values required for the grain sizes. Thus, $a \gg w$, and the extinction cross–sections are largely dominated by the optical properties of silicate cores. The reverse is true for the small grain component (e.g., Iatì et al. 2008).

In figure (2.9) we report the carbon and silicon abundances (ppm), together with mass constraints in the ISM. In most of the cases the required silicon budget is consistent with Si solar abundance, (Si/H) = 32.4 ppm (Asplund et al., 2009), as well as with values derived by Miller et al. (2007) along translucent lines of sight, and towards F and G stars (cf. Zubko et al. 2004). For two lines of sight (models 11 and 15) the minimization procedure derives very large Si abundances. This is due to large values

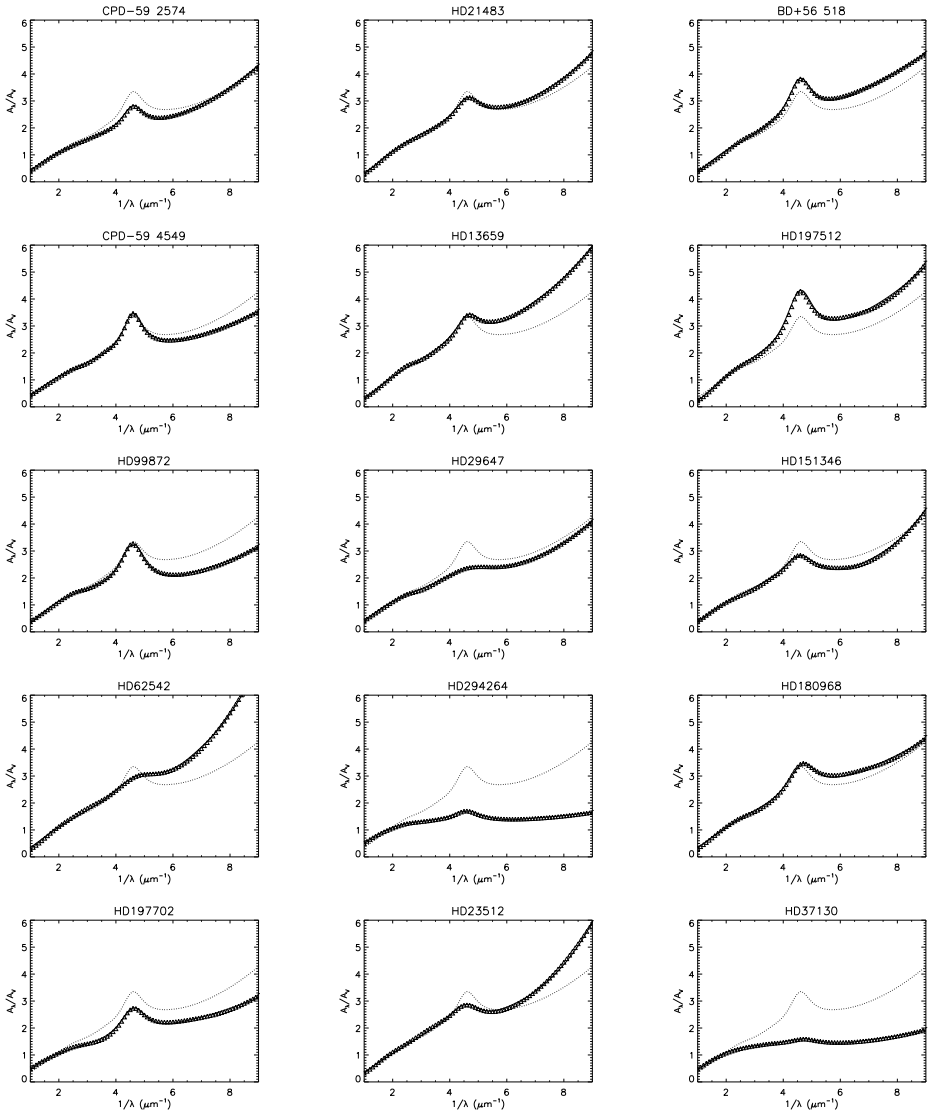

Figure 2.8: Synthetic extinction curves (solid lines) compared to observational data (triangles) from the samples of Fitzpatrick and Massa (2007). The label on the top of each panel indicates the line of sight (see table 2.2). For comparison we report the average Galactic curve (dotted line).

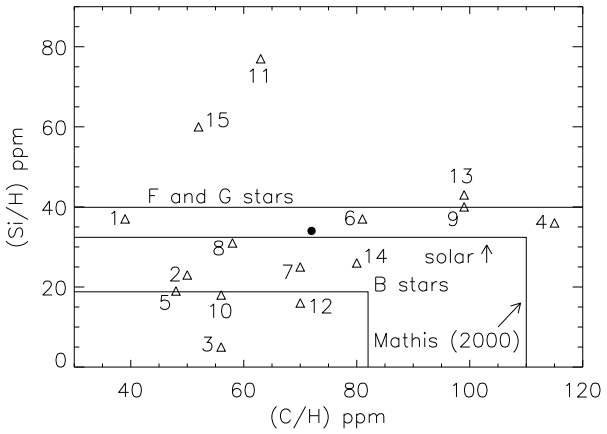

Figure 2.9: Numbers of carbon and silicon atoms (ppm) for the 15 lines of sight reported in table (2.2). The black dot represents the average ISEC.

for $R_V \geq 5$, as the silicon and carbon concentrations scale with it, equations (2.21) and (2.22). However, at such high R_V values, the validity of equation (1.12) is questionable, and the derived dust mass budgets might be unreliable. Carbon abundances are much lower than the F and G star abundances, (C/H) = 250 ppm, with only model 4 slightly exceeding the Mathis (2000) estimate, (C/H) = 110 ppm. The carbon mass balance is in most cases driven by PAHs. Models 4, in which small grains lock a number of carbon atoms similar to the one in PAHs, and 15 have more carbon atoms in classical dust than in molecules.

The lines of sight of the present sample seem to be characterized by the lack of small grains, that are present in only 3 models out of 15. Data in table (2.3) are not very suggestive, as they do not show any evident trend. We report in figure (2.10) the observational ratios between the extinction at the bump peak wavelength with the extinction at 6 μm^{-1}, A_{bump}/A_6, and between the extinction at 9 μm^{-1}, A_9, and A_6. Extinction values at these three wave numbers partly reflect the Fitzpatrick and Massa (2007) UV parametrization. To enlarge the extinction sample we include in figure also the lines of sight considered by Cecchi-Pestellini et al. (2008), i.e. we compare the present results, derived for ISECs "far" from the average curve, with models to extinction profiles, whose morphologies are more similar to the mean properties of the Galactic dust. The plot in figure (2.10) shows the tendency of those extinction curves, whose models require the presence of small grains ($a \leq 15$ nm), to lie close to the average ISEC. Of course, due to the low number of cases, this result is devoided of any statistical significance. Nevertheless, such conclusion is not either unrealistic or unexpected, since extinction by such small grains is effective only in the UV spectral domain, in which an ISEC can show significant departures from the average Galactic curve.

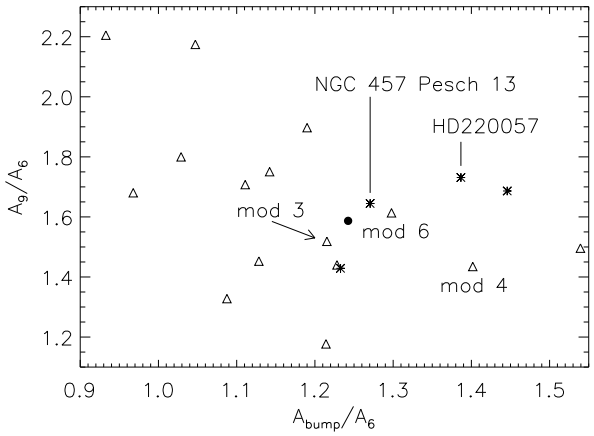

Figure 2.10: $A_{\rm bump}/A_6$ vs A_9/A_6 for the lines of sight in table (2.2) (triangles), and for the ISECs modelled by Cecchi-Pestellini et al. (2008) (asterisks). The black dot represents the average ISEC. Labels indicate models that include a small grain component.

2.4 Discussion

About 40 yr ago Greenberg (1973) showed that observational criteria could be found, implying that the onset of the rapid increase in the UV is due to dust grains with typical sizes approximately smaller than 20 nm, while larger particles dominating the extinction at longer wavelengths contribute with a saturated baseline relatively independent of the particular grain material. This conclusion is actually embedded in the Fitzpatrick and Massa (2007) data, and a possible interpretation is given through the present model.

The composition, structure, and size distribution of interstellar grains are the result of injection of dust from stellar outflows into the interstellar medium, followed by destruction, growth, coagulation, and photo–processing of interstellar grains. Along a line a sight an extinction curve is generated by the balance among these processes, and eventually a wide dispersion of ISECs is produced. Our model may handle cases, in which there are extreme variations in the shape of the extinction curve, such as e.g., the HD62542 or HD37130, by simply assuming a different ratio of PAHs to classical dust. However, any physical characterization would imply the knowledge of PAH evolution and their relation with solid dust grains, a measure of the activity of the ISM (e.g., in terms of the passage of shocks), that is currently poorly understood. Nevertheless, it is encouraging that a dust model consisting of a bimodal dust population fits any ISEC very well, with a mass budget close to the interstellar abundance constraints, without invoking particular dust size distributions, or *ad hoc* configurations.

Some lines of sight exhibit extinction profiles where the 217.5 nm bump is weak or even totally missing, while showing a marked FUV rise. Such lines of sight are located in the upper left part of figure (2.10). Setting an (arbitrary) threshold $A_{\rm bump}/A_6 < 1.1$, we select models 5, 8, 10, 14, and 15. Models 5 and 14 show an appreciable bump, while model 15 requires a very small amount of carbon in PAHs. Although the fitting procedure may provide synthetic profiles for the two remaining lines of sight (HD29647 and HD62542) in remarkable agreement with the observed extinction curves, such cases

are impossible to interpret in terms of the photo–absorption properties of free–flying PAHs (Malloci et al., 2007). These curves resemble the extinction profiles in the MCs (cf. figure 1.3 in Section 1.6).

When extinction curves are very steep (e.g, HD62542), Fitzpatrick (2004) suggests that the weakness of the bump may be apparent, being an artifact of the normalization. However, such suggestion may fail in explaining the weakening of the bump in the flattest (highest R_V) extinction curves (Fitzpatrick, 2004), such as HD29647. Whatever the case may be, suppression of the $\pi-$plasmon resonance in small carbon particles can be obtained increasing the density of sp^3 bonds (e.g., Jones et al. 1990, Duley 2006a). This may hint super–hydrogenation (Hecht, 1986) or the presence of a significant fraction of carbon in nanodiamonds (e.g., Rai and Rastogi, 2010).

Whittet et al. (2004) infer that HD29647 might be located in the diffuse intraclump region of the Taurus molecular cloud immediately behind TMC-1, and may, therefore, show combined features of diffuse and dense regimes. Indeed, such a line of sight displays a weak ice feature (Goebel, 1983). Even the line of sight toward HD62542 appears to be associated to a region that is denser than the average diffuse ISM (Gredel et al., 1993), i.e. the core of a diffuse cloud. The original cloud has apparently been stripped of the lower density outer layers by stellar winds and radiation pressure (Cardelli et al., 1990). Therefore, some specific mechanism in dense environments, such as coagulation, may lead to broadening and suppression of the bump. However, the extinction curve towards HD62542 presents an UV extinction very high and steep, implying a great abundance of very small grains. If hydrogenation is the dominant factor in the weakening of the bump, evidence for this is expected in the IR, in the form of 3.4 μm absorption arising from surface C–H bonds.

Both models 8 and 10 have, if any, very thin carbon mantles. Hydrogenation is therefore consistent with the dust description adopted in this work: carbon layers are indeed expected to be abruptly removed by occasional shocks from the silicate cores, and then slowly re–deposited (Cecchi-Pestellini et al., 2010). In the dynamical scenario outlined above, mantle fragments heated in a hydrogen plasma re–arrange their carbon skeletons from sp^2 to sp^3 bondings in HAC (e.g., Landstrass and Ravi 1989, Furton and Witt 1993). This "mesoscopic" component, whose optical properties cannot be described in terms of a superposition of PAH cross–sections, may constitute the "low mass" tail of the classical grain size distribution, and provide an efficient extinction in the FUV without the bump at 217.5 nm. In their study of the line of sight towards HD204827, an extinction curve with a very steep UV profile and little or no 217.5 nm bump, Valencic et al. (2003) find that shocks due to a supernova may have led to a substantial processing of the dust. They also suggest that the environment of the HD204827 cloud dust may be similar to the dust associated with HD62542, which lies on the edge of a stellar wind bubble and is also dense and rich in molecules. Interestingly, the 3.4 μm feature indicating a C–H rich grain mantle is present in the dust toward HD204827.

In conclusion we model successfully a number of Galactic extinction curves, whose shapes are extremely different from the average ISEC, and we find that these so–called peculiar curves do not need exotic properties of dust grains to be accurately described. We are thus tempted to conclude that the wide dispersion in the ISEC morphology may merely reflect the grain size distributions and the chemical response of dust materials to the environmental conditions along their sightlines, whithin the general circulation of matter into and out of clouds and stars.

Chapter 3

Modeling galactic extinction

3.1 Introduction

In the previous chapter the simplified version of the $[CM]^2$ model has been exploited to successfully model a number of Galactic extinction curves, whose shapes are extremely different from the average ISEC. The main result of such analysis is that the so–called peculiar curves do not need exotic properties of dust grains to be accurately described. It means that the wide dispersion in the ISEC morphology may merely reflect the grain size distributions and the chemical response of dust materials to the environmental conditions along their sightlines. This conclusion is implicitly embedded in the general observational result that ISECs can be phenomenologically described by means of a very limited number of empirical parameters (Cardelli et al. 1989, Valencic et al. 2004, Fitzpatrick and Massa 2007). Fitzpatrick and Massa (2007), and previous works referenced therein, showed that all ISECs can be accurately described by a 6–parameters empirical representation. Cardelli et al. (1989) showed that (with few notable exceptions) these 6 parameters can be expressed as (empirically determined) functions of a single free one.

The next step, performed in this chapter, is the upgrade of the $[CM]^2$ model, replacing the simplified description of the molecular component as a double lorentzian profile with a collection of "real" PAH cross–sections, and to systematically fit the *whole* sample of galactic extinctions provided by Fitzpatrick and Massa (2007). We do not mean to assess whether this model is better than other current alternatives, which might equally well reproduce the same data. This work aims at reconciling all the observed variety of ISECs within a unified model of interstellar dust, to unfold the synthetic description of dust into physically well–grounded properties. This is not a trivial task since, given the complexity of the underlying physics and chemistry, *any* physical dust model requires a relatively large number of parameters, typically not fewer than $\sim$12 even despite drastic simplifying assumptions. To try to understand how and why the physical parameters defining the populations of interstellar dust and macromolecules may respond to a smaller number of parameters defining the environmental conditions, one must begin by determining the former ones on a large statistical sample of observations, so that further analysis becomes possible. And one must do so in a way that is

- homogeneous: using the same model and assumptions, so that variations between lines of sight are less masked by systematic effects;
- realistic: using a model simplified enough to be tractable, yet still containing

enough physical information to be worth the effort;

- validated: meaning that it can match all observations within observational errors.

This work represents a first step in this direction. We associate a set of well–defined *physical* dust parameters to each line of sight in a statistically relevant sample of different ISECs, with a solid analysis of how tightly constrained (or not) they are by the fit. This makes the search for trends and correlations with other possibly related observable quantities possible.

3.2 The new simplified version of the $[\mathrm{CM}]^2$ model

At first we applied a slightly modified version of the $[\mathrm{CM}]^2$ model to fit the full sample of 328 galactic ISECs. Guided by quantum–chemical calculations performed by Malloci et al. (2007), we slightly change the exponential damping factor to $1/\{1+\exp[(C_1 - \lambda^{-1})/C_2]\}$, in order to remove any contribution of the electronic photo–absorption by the molecular component to the extinction longward of visual wavelengths. The free parameters of the modified simplified molecular component are therefore:

Li_1 integral of the first Lorentzian

Lp_1 peak wavenumber of the first Lorentzian

Lw_1 Full Width at Half Maximum (FWHM) of the first Lorentzian

Li_2 integral of the second Lorentzian

Lp_2 peak wavenumber of the second Lorentzian

Lw_2 FWHM of the second Lorentzian

C_1 center of the exponential cut–off

C_2 width of the exponential cut–off

As in the previous version these parameters also are constrained to be physically sensible, i. e. $Li_1 \geq 0$, $Li_2 \geq 0$, $Lw_1 \geq 0\,\mu\mathrm{m}^{-1}$, $Lw_2 \geq 0\,\mu\mathrm{m}^{-1}$,$Lp_1 \leq Lp_2$, $C_2 \geq 0\,\mu\mathrm{m}^{-1}$.

3.3 The detailed version of the $[\mathrm{CM}]^2$ model

In the detailed version of the extinction model, the molecular component, instead of being represented by two Lorentzian profiles parametrised to fit the average of the *ab initio* photo–absorption cross–sections of a sample of 54 PAHs in 4 charge states, is represented by a straightforward linear combination of the same cross–sections. In this case, therefore, the formal free parameters become the 216 individual column densities of each PAH in each charge state considered, each of them subject to the obvious physical constraint of being non–negative. This is a more demanding constraint than it might appear at first sight: from a mathematical point of view, it reduces the available space for these parameters by a factor 2^{216}; from a physical point of view, it means that it is impossible to "subtract away" an unobserved absorption band of a molecule with a negative amount of other molecules.

These photo–absorption cross–sections were calculated by means of the Density Functional Theory and its time dependent extension Time Dependent Density Functional Theory (Malloci et al., 2007). Figure (3.1) shows the accuracy of the computational method comparing neutral anthracene computed cross–section with its observed absorption profile. Figure (3.2) shows cross–section for coronene in the principal charge states (left panel), and a blow–up of the same plot in the region where ISECs are studied (right panel).

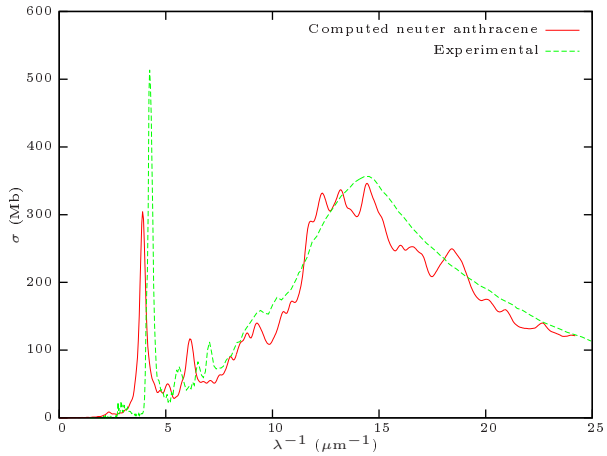

Figure 3.1: Comparison between computed photo–absorption cross–section for the neutral anthracene $C_{14}H_{10}$ and the corresponding observed absorption spectra (Malloci et al., 2004).

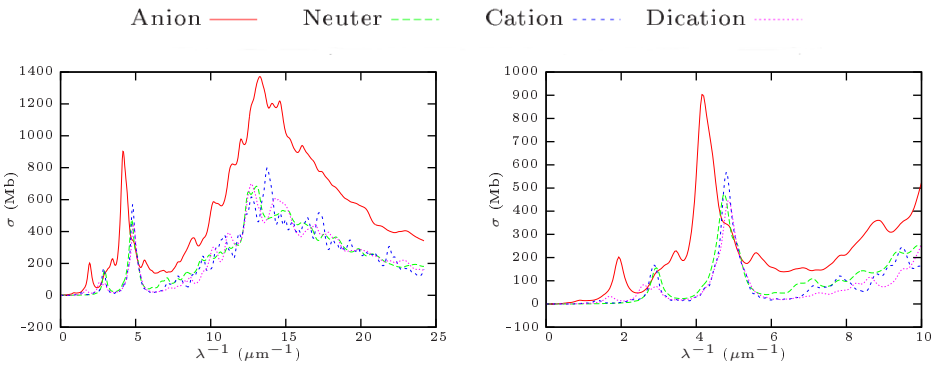

Figure 3.2: Photo–absorption cross–section for coronene in four different charge states. In the right panel the same plot is represented but in the range for which ISECs are plotted.

Figure (3.3) displays cross–section for a PAHs mixture, obtained by a linear combination of 54 PAHs cross–sections normalized on the carbon atoms number. Then the result is a cross–section per carbon atom. The cross–section variation with the charge state is visible and this variation is particularly clear in the region of the first maximum, then in the region correspondent at the interstellar *bump*. Moreover both

profiles, correspondent to the resonance $\pi^* \leftarrow \pi$ and $\sigma^* \leftarrow \sigma$, and the depth of the minimum in the link region between these two resonances have an intensity dependent by the charge state. Then the PAHs charge state may be linked to the morphological properties of the ISEC and variations in the intensity and in the non linear rise slope in the FUV observed by Fitzpatrick and Massa (2007) may give some informations about the relative intensity and the position of $\pi^* \leftarrow \pi$ and $\sigma^* \leftarrow \sigma$ resonances.

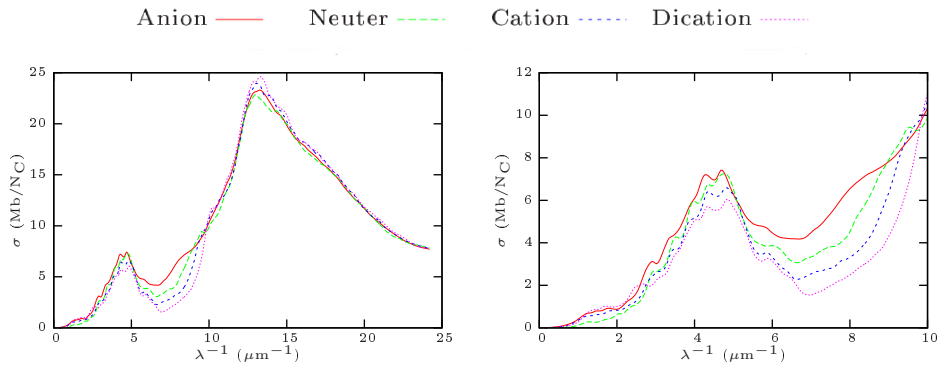

Figure 3.3: Photo–absorption cross–section per carbon atoms number for a mixture of 54 PAHs in four charged states. In the right panel the same plot is represented but in the range for which ISECs are plotted.

3.4 Fitting details

The data to be fitted are taken from the published data of Fitzpatrick and Massa (2007). Such data consist of tabulated extinction curves, expressed in units of normalised color excess $E_{\lambda-V}/E_{B-V}$, and the corresponding tabulated errors. Since the extinction model used here is expressed in units of normalised total extinction A_λ/A_V, we first convert all tabulated data to these units, using the $R_V = A_V/E_{B-V}$ values given in the same work.

We then use a slightly modified version of the C MPFIT[1] implementation of the Levemberg–Marquardt non–linear least squares algorithm to actually perform the fits, both with the simplified and with the detailed version of the extinction model. The iterative fit procedure seeks to minimise the numerical χ^2 starting from a given (hopefully sensible) first guess of the free parameters, making sure all parameter constraints are respected. The apparent drawback of this kind of procedure is that the algorithm will fall in the nearest minimum which it can reach by descending the χ^2 hypersurface in the free parameters from the starting point. If the hypersurface is ill–behaved enough, the algorithm may get stuck on a local minimum, with a much larger χ^2 than the global one, or even on a saddle point. The curvature of the χ^2 hypersurface at the minimum can be used, in principle, to yield information on the covariance matrix of the parameter values derived from the fit. This evaluation of the covariance is indeed returned as one of the results by the MPFIT function. However, this is a good approximation only if

[1] http://www.physics.wisc.edu/∼craigm/idl/cmpfit.html

the second order Taylor expansion of the χ^2 hypersurface around its minimum $\chi^2_{\rm min}$ is accurate for all the region around the minimum in which the $\chi^2 \leq \chi^2_{\rm min} + 1$.

Since this is not necessarily true, and indeed the covariance values returned by MPFIT are sometimes clearly not sensible in our case, we use another strategy, which is useful both to provide a robust evaluation of the covariance matrix of the fitted parameters, and to get out of local minima and saddle points. After performing a successful fit on one of the original data samples, we perturb it by a random gaussian noise proportional to the errors, also taken from Fitzpatrick and Massa (2007), and repeated the fit on the perturbed data. The procedure is iterated to obtain some synthetic statistics. In some cases, the fit to the perturbed data is a better match even for the unperturbed data, meaning that the first fit had ended on a local minimum or saddle point. In that case, the whole procedure is restarted using the new "best guess" as initial point. The synthetic statistics on the fitting parameters are then used to directly estimate their covariance matrix. In some cases, some of the parameters are constrained by the fit so much more tightly than others (i. e. the derivative of χ^2 with respect to some parameter was much smaller than that with respect to another) that the formal variance of the better constrained parameter results to be zero, i. e. the fit converged on the same value of that parameter in all perturbed fits, within numerical accuracy. This does not mean that this parameter is really determined with infinite accuracy, but merely that its error is below the capability of the algorithm to evaluate it. The random error we introduce in perturbed fits is completely uncorrelated, i. e. adjacent pixels have the same probability of being perturbed in the same as in opposite directions. This implies that our error estimation cannot account for any possible *systematic* observational error in some observed extinction curve, whereby e. g., the whole visible part of the ISEC was overestimated. Therefore, in such cases, we would somewhat underestimate the errors in the fitted parameters.

Fits using the detailed extinction model pose an additional problem, which required a slight modification of the MPFIT implementation. As detailed in appendix A, the Levemberg–Marquardt method proceeds by linearising the non–linear least squares problem around the previous guess of the parameter values. It builds and solves a system of linear equations (with some clever modifications to ensure robust and rapid convergence) to obtain the next improved guess of the fitting parameters. If the linear system is quasi–singular[2], its solution is numerically unstable, and the iterative step may produce useless results with the standard MPFIT implementation. Such a behaviour reflects a real problem, i. e. the fit is strongly underconstrained when the detailed extinction model is used. The implication is not that the fit is without solution, but rather that the solution is far from unique. In particular, there is a large subspace of the parameter space that fits each extinction curve being fitted. In other words, there is not a unique mixture of the PAHs in our sample which best fits a given extinction curve, but a *family* of PAH mixtures that all fit it very nearly equally well. This entails two problems: first, the practical, numerical, one of finding one representative of this family of solutions, overcoming the instability of the standard Levemberg–Marquardt implementation in MPFIT. This is addressed by solving the linear problem in each iteration via Singular Value Decomposition (SVD), and discarding "singular" values at, or below, the level of numerical noise before inverting the matrix to solve the linear problem. In such a way we provide a robust method to converge on *one* solution of the family. The results are remarkably insensitive to the precise threshold one chooses to accept or discard

[2]It cannot be *really* singular due to the way the Levemberg–Marquardt method builds it, but it can be *very* close to singular.

singular values. The minimum number of singular values that must be retained without adversely affecting the quality of the fit is between 20 and 30: keeping many more that 30 includes some that are just noise, keeping less than 20 discards too much real information. Synthetic statistics then provide a way to obtain a *sample* of the family of solutions, since each perturbed fit converges to a different individual solution.

The second problem is related to the physical interpretation of the results: while it is impossible to constrain the precise composition of PAHs using only the extinction curve, we can instead hope to constrain rather precisely some of the PAH properties as a group (e. g., total amount of C atoms in PAHs, charge per C atom, and so on). In a way, the minimum of the χ^2 hypersurface looks like a trough in the PAH parameters, which is shallow or flat in many directions (representing PAH properties poorly constrained by the fit), but steep in some (representing, on the contrary, properties of the PAH family strongly constrained by the fit). A hint about the number of global parameters well–constrained by the fit can be obtained from the minimum number of Singular Values in the SVD that need to be retained (i. e. 20 to 30). The 9 parameters of classical dust grains are all rather well constrained by the fit, so this leaves ≤ 15 parameters defining the PAH mixture (out of the 216 column densities). So, while on the one hand this clearly exposes that the information one can hope to attain by such a huge and cumbersome fit is limited, on the other hand the fact that it can constrain some *global* properties of the PAH mixtures fitting the extinction lends credibility to these results, making them far less dependent on the specific species used for the fit. Indeed, very nearly the same results are obtained even if one uses half of the 54 PAHs chosen randomly or worse (see discussion in Sect. 3.5.4). In any case, the physical problem now becomes that of linking these relatively few global PAH parameters to meaningful physical/chemical properties characterising the mixtures fitting the extinction. This is a task that simplified descriptions of PAHs are unable to address, since molecular properties and electronic structures are smeared out into an homogeneous mixture.

3.5 Results

Figure (3.4) shows a small, representative sample of the extinction curves and their fits using the detailed model. They are chosen to represent all different "flavours" of observed extinction curves, ranging from what is considered the "average" galactic extinction curve to virtually "bumpless" ones, similar to the ones frequently observed in galaxies at high red–shifts, or in parts of the MCs. Moreover, the eight lines of sight in figure (3.4) present widely varying relative intensities of the different components of the Fitzpatrick and Massa (2007) parametrization, as well as different bump widths. Indeed, we chose by and large the most extreme cases we could find. The observed extinction curves are represented in figure (3.4) by the dotted lines, the fitted curves obtained with our model (detailed version) are the continuous lines, the error range reported by Fitzpatrick and Massa (2007) is the lightly shaded area in each plot. In the same plots, the dashed lines show the contribution of the classical dust component in our model, the dash–dotted lines the contribution by the mixture of PAHs.

In all cases the fitted extinction curve is virtually undistinguishable from the observed one. The fitted extinction curves are also remarkably "smooth", with no detectable fine structure. While only eight lines of sight are shown here, this is the rule for *all* cases, with no exception (see left panel in online figures 2.1 to 2.329 of Mulas et al. 2013). This unambiguously proves that a mixture of a relatively small number of

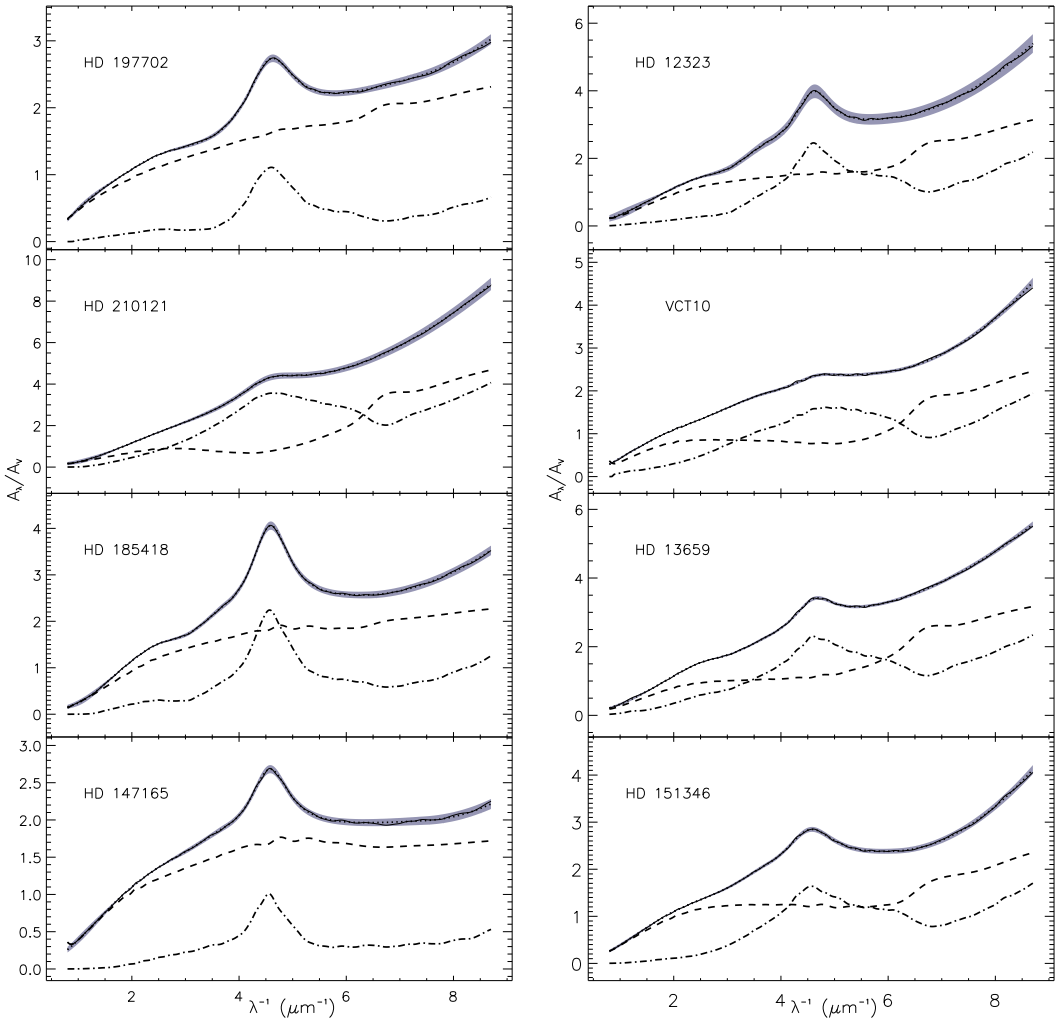

Figure 3.4: Fits to the normalized extinction curves for eight lines of sight chosen to be representative of the features carried by the Galactic curves. Solid lines: fit; dashed lines: classical dust contribution; dot–dashed lines: PAHs. The lightly shaded areas are the observational error ranges given in Fitzpatrick and Massa (2007).

PAHs *can* reproduce the features of the extinction curve in the UV, putting to rest an old objection to the contribution of PAHs to the ISEC. While PAHs are not the *unique* solution to represent UV extinction features (and we do not claim they are) they are proven to be a viable one.

Table (3.1) is an excerpt of the online table (4) of Mulas et al. (2013). For each line of sight we report the fitted values of the parameters of the classical dust component, resulting both from the simplified and detailed versions.

3.5.1 Classical dust distribution parameters

Some of the parameters determining the distribution of classical dust grains appear to be remarkably constant across the whole sample of lines of sight. This is the case for the q exponent in the power law size distribution, which is almost always very close to 3.45, with few exceptions. Also the lower limit a_- of the "small" grain sizes is very nearly always fixed on a limit value of 5 nm. This is the minimum size included in our model, and indeed the fit, if unconstrained, would in most cases try to move further down to smaller sizes. The upper limit b_+ of the "big" grain sizes appears to show relatively little variation as well. In this case, this is because the modelled extinction curve (in the interval considered) is remarkably insensitive to the population of dust grains on the bigger end of the size distribution. Arbitrarily setting this limit to extend to pebble–sized grains would not be visible in the modelled extinction curves here. The values of b_+ that we obtain should therefore be regarded as lower limits. Such upper size limit would be better constrained by extending the fit to IR portions of ISECs (e. g., Fitzpatrick and Massa 2009), and including silicate absorption features at 10 and 18 μm.

The fraction of vacuum f_v in the classical dust grains appears to cluster rather tightly around $\sim 0.4 \pm 0.15$. We therefore obtain relatively hollow particles. Silicate porosity may be a relevant parameter when we study the optical behaviour of large grains, because it strongly affects the strength and the shape of silicate absorption features (e. g., Iatì et al. 2001, 2011 and Voshchinnikov and Henning 2008).

Carbonaceous mantles appear to be mostly ~ 1 nm thick (parameter w), more tightly so in the detailed models and with more scatter in the simplified models. In a non–negligible number of lines of sight we obtain vanishing mantle thickness, but only with the simplified model, whereas this essentially never happens with the detailed one. This might pose some problems if the lines of sight with negligible w also have a non–negligible population of very small grains: if naked, they would be expected to emit in the silicate bands, when transiently heated by the absorption of energetic photons, and such emission is not observed. This does not happen for the size limits adopted here, since even the smallest grains, with a 5 nm radius, would have relatively small temperature fluctuations. It might become a problem if one wants to allow silicate cores to reach sizes around ~ 1 nm (or smaller). Also, a small but non–negligible number of lines of sight show w values of 3 nm. This was adopted as an upper limit in the fit, to avoid using an unphysically large amount of Carbon in grain mantles. If left free, these fits would have converged to somewhat larger values of w. The other parameter defining the carbonaceous mantles is f_{sp^2}, the fraction of sp^2 carbon. This parameter is less tightly determined by the fit, but in most cases is close to 1, with only few cases of mostly aliphatic (polymeric) carbonaceous material.

The parameters a_+ and b_- give a "hole" in the size distribution of classical dust grains. a_+ shows a systematic difference between the simplified ($a_+ \sim 13$ nm) and

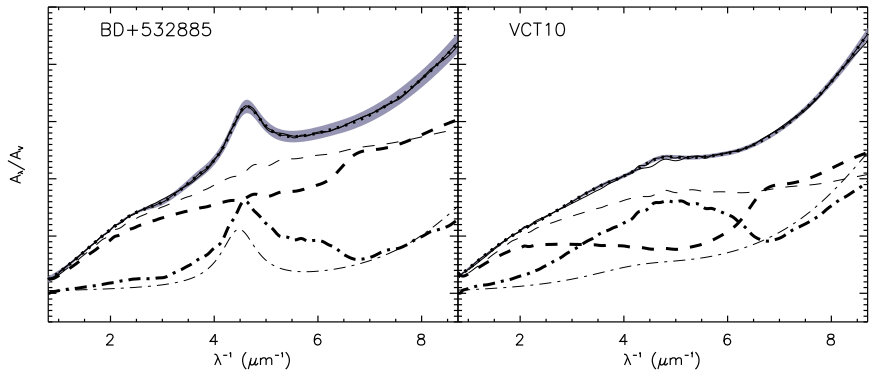

Figure 3.5: Comparison of synthetic ISECs obtained with simplified (thin lines) and detailed (thick lines) models for the lines of sight towards BD+532885 and VCT10. Solid lines: fit; dashed lines: classical dust contribution; dot–dashed lines: PAHs. The lightly shaded areas are the observational error ranges given in Fitzpatrick and Massa (2007).

detailed ($a_+ \sim 25$ nm) models. In both cases there are relatively large scatters around these averages, going from ~ 5 nm (no small grains, since 5 nm $\leq a_- \leq a_+$) to twice the average. The values of b_- cluster around $\sim$70 nm, again with very considerable scatters, ranging from half to $2-3$ times the average. This range is larger for the detailed model, which requires larger gaps in the size distribution to account for some peculiar cases (see Sections 3.5.2 and 3.5.3).

3.5.2 Comparison between simplified and detailed model results

The simplified model (Iatì et al., 2008) was derived from, and calibrated on, the same PAH photo–absorption cross–sections which are explicitly included in the detailed model. The two models are therefore expected to produce very similar results, both in the PAH abundances and even more so in the classical part, which is exactly the same in both models. Still, some differences remain, and should be taken as a lower bound to the systematic uncertainty in our model–derived quantities, since they stem from different model choices. Much of this difference results from the very different "flexibility" of the two representations of PAH extinction. In the simplified model, the two Lorentzians representing the $\pi^\star \leftarrow \pi$ and the $\sigma^\star \leftarrow \sigma$ broad resonances have complete freedom to vary their relative intensities, while being restricted to be strictly Lorentzian in shape. Conversely, in the detailed model the intensity ratio between the $\pi^\star \leftarrow \pi$ and the $\sigma^\star \leftarrow \sigma$ resonances can have limited variability, mainly due to charge effects, whereas the $\pi^\star \leftarrow \pi$ resonance can change its shape more freely depending on the specific species included in the mixture, since the exact positions of $\pi^\star \leftarrow \pi$ transitions are rather variable in individual species.

When fitting the same extinction curve, especially if it is a relatively non–standard one, the extinction component due to classical dust has to compensate these differences, resulting in the observed difference in classical dust distributions between the two models (see figure 3.5).

LoS	N_d (μm$^{(q-3)}$)	f_v	w (nm)	f_{sp^2}	a_- (nm)	a_+ (nm)	b_- (nm)	b_+ (nm)	q	χ^2_{red}
Average ISEC	1.013 (0.016)	0.45 (0.02)	1.3 (0.5)	0.98 (0.05)	5.10 (0.24)	11.9 (2.6)	63.3 (2.3)	491 (12)	3.469 (0.002)	$< \varepsilon_4$
	0.999711 ($< \varepsilon_1$)	0.45 ($< \varepsilon_2$)	0.97 ($< \varepsilon_2$)	0.92 ($< \varepsilon_2$)	5.00 ($< \varepsilon_2$)	27.00 ($< \varepsilon_2$)	70.40 ($< \varepsilon_2$)	493.06 ($< \varepsilon_2$)	3.4727 ($< \varepsilon_3$)	$< \varepsilon_4$
HD12323	1.152 (0.011)	0.44 (0.01)	0.95 (0.23)	0.5 (0.3)	5.00 ($< \varepsilon_2$)	13.2 (1.3)	56.8 (2.8)	465 (6)	3.4487 (0.0013)	$< \varepsilon_4$
	1.128 (0.022)	0.48 (0.03)	0.75 (0.13)	0.67 (0.13)	5.00 ($< \varepsilon_2$)	42 (6)	133 (28)	492 (11)	3.48 (0.01)	$< \varepsilon_4$
HD13659	0.966 (0.004)	0.47 (0.01)	0.67 (0.06)	0.87 (0.06)	5.00 ($< \varepsilon_2$)	14.45 (0.08)	55.2 (1.2)	479.2 (2.7)	3.4664 (0.0004)	0.4
	1.0246 (0.0018)	0.36 ($< \varepsilon_2$)	0.51 ($< \varepsilon_2$)	0.00 ($< \varepsilon_2$)	5.00 ($< \varepsilon_2$)	55.5 (0.4)	129.4 (1.8)	485.99 (0.24)	3.4945 (0.0005)	0.2
HD147165	0.9978 (0.0022)	0.32 ($< \varepsilon_2$)	3.00 ($< \varepsilon_2$)	1.00 (0.01)	5.05 (0.05)	13.05 (0.23)	67.96 (0.19)	517.5 (1.3)	3.4714 (0.0004)	0.1
	0.998617 ($< \varepsilon_1$)	0.37 ($< \varepsilon_2$)	3.00 ($< \varepsilon_2$)	0.78 ($< \varepsilon_2$)	6.37 ($< \varepsilon_2$)	13.65 ($< \varepsilon_2$)	65.00 ($< \varepsilon_2$)	566.37 ($< \varepsilon_2$)	3.4717 ($< \varepsilon_3$)	0.2
HD151346	1.024 (0.007)	0.35 (0.01)	1.55 (0.14)	1.00 ($< \varepsilon_2$)	5.38 (0.05)	7.8 (0.4)	69.4 (0.8)	515.0 (3.0)	3.4659 (0.0007)	0.1
	0.969 (0.004)	0.27 (0.01)	0.98 (0.04)	0.91 (0.01)	5.00 ($< \varepsilon_2$)	26.1 (0.7)	107.7 (1.5)	492.2 (1.0)	3.4874 (0.0015)	0.1
HD185418	0.968582 ($< \varepsilon_1$)	0.50 ($< \varepsilon_2$)	1.00 ($< \varepsilon_2$)	0.50 ($< \varepsilon_2$)	8.00 ($< \varepsilon_2$)	20.00 ($< \varepsilon_2$)	70.00 ($< \varepsilon_2$)	459.00 ($< \varepsilon_2$)	3.3948 ($< \varepsilon_3$)	0.9
	0.933621 ($< \varepsilon_1$)	0.52 ($< \varepsilon_2$)	3.00 ($< \varepsilon_2$)	0.07 ($< \varepsilon_2$)	5.00 ($< \varepsilon_2$)	24.97 ($< \varepsilon_2$)	85.87 ($< \varepsilon_2$)	470.13 ($< \varepsilon_2$)	3.3957 ($< \varepsilon_3$)	0.1
HD197702	0.852 (0.007)	0.39 (0.02)	3.00 ($< \varepsilon_2$)	1.00 ($< \varepsilon_2$)	5.00 ($< \varepsilon_2$)	17.1 (0.4)	55.7 (1.7)	523.8 (2.7)	3.4930 (0.0011)	0.8
	0.864020 ($< \varepsilon_1$)	0.09 ($< \varepsilon_2$)	3.00 ($< \varepsilon_2$)	1.00 ($< \varepsilon_2$)	5.10 ($< \varepsilon_2$)	28.00 ($< \varepsilon_2$)	45.41 ($< \varepsilon_2$)	567.33 ($< \varepsilon_2$)	3.5098 ($< \varepsilon_3$)	0.1
HD210121	1.198 (0.011)	0.43 (0.03)	0.00 ($< \varepsilon_2$)	1.00 ($< \varepsilon_2$)	5.01 (0.02)	11.7 (0.7)	65.1 (0.9)	400 (10)	3.4420 (0.0026)	0.1
	1.860 (0.009)	0.46 (0.03)	0.61 (0.06)	0.21 (0.12)	5.00 ($< \varepsilon_2$)	47.2 (1.1)	252.6 (2.4)	386.8 (2.4)	3.4501 (0.0009)	$< \varepsilon_4$
VCT10	0.970 (0.029)	0.44 (0.04)	1.24 (0.27)	0.94 (0.07)	5.00 ($< \varepsilon_2$)	13.3 (1.2)	74 (6)	600 (60)	3.487 (0.007)	1.4
	0.9854 (0.0016)	0.33 (0.01)	0.45 (0.02)	0.66 (0.02)	5.00 ($< \varepsilon_2$)	36.34 (0.17)	160 (4)	561.1 (1.3)	3.5054 (0.0015)	0.4

Table 3.1: Classical dust component parameters, obtained from the simplified and the detailed models, for the average ISEC and for the lines of sight plotted in figure (3.4). We adopt $\varepsilon_1 = 0.000001$, $\varepsilon_2 = 0.01$, $\varepsilon_3 = 0.0001$, $\varepsilon_4 = 0.1$. Note that this table is an excerpt of the of the online table (4) of Mulas et al. (2013).

LoS	Si/H (ppM)			C/H (ppM)			
	Small grains	Large grains	Total	Small grains	Large grains	PAHs	Total
Average ISEC	1.9 (0.7)	40.6 (1.2)	42.5 (1.7)	9.8 (3.9)	8.8 (3.2)	126.9 (9.3)	145.5 (12.2)
	6.0 ($<\varepsilon$)	39.0 ($<\varepsilon$)	45.0 ($<\varepsilon$)	14.5 ($<\varepsilon$)	5.7 ($<\varepsilon$)	64.3 (2.3)	84.5 (2.3)
HD12323	2.6 (0.3)	44.2 (2.1)	46.8 (2.2)	7.3 (3.3)	5.6 (2.3)	141.0 (6.9)	153.9 (7.3)
	8.6 (1.1)	27.2 (3.2)	35.8 (2.2)	10.3 (1.9)	1.9 (0.5)	281.1 (46.1)	293.2 (46.0)
HD13659	2.6 ($<\varepsilon$)	33.6 (0.7)	36.2 (0.7)	5.8 (0.7)	3.8 (0.6)	85.1 (1.1)	94.7 (2.3)
	11.4 ($<\varepsilon$)	26.0 (0.3)	37.5 (0.2)	4.1 ($<\varepsilon$)	0.6 ($<\varepsilon$)	70.5 (0.5)	75.2 (0.5)
HD147165	1.9 (0.1)	59.3 (0.1)	61.2 (0.1)	27.3 (0.4)	27.7 (0.2)	82.8 (1.4)	137.8 (1.6)
	1.9 (0.1)	59.3 ($<\varepsilon$)	61.1 (0.1)	21.7 (1.1)	23.3 ($<\varepsilon$)	40.2 (0.6)	85.3 (1.3)
HD151346	1.0 (0.2)	62.6 (0.7)	63.6 (0.6)	9.4 (1.0)	15.0 (1.4)	119.0 (3.4)	143.4 (3.8)
	9.4 (0.3)	52.3 (0.4)	61.7 (0.3)	23.3 (1.0)	6.2 (0.3)	71.7 (1.8)	101.3 (2.5)
HD185418	3.9 (0.2)	42.1 ($<\varepsilon$)	46.0 (0.2)	8.2 (0.7)	4.7 ($<\varepsilon$)	154.2 ($<\varepsilon$)	167.1 (0.7)
	3.1 ($<\varepsilon$)	37.6 ($<\varepsilon$)	40.8 ($<\varepsilon$)	11.8 ($<\varepsilon$)	7.1 ($<\varepsilon$)	78.6 (0.9)	97.5 (0.9)
HD197702	3.1 (0.2)	61.5 (1.7)	64.6 (1.9)	36.8 (1.7)	31.7 (1.5)	158.8 (1.8)	227.3 (4.9)
	8.7 ($<\varepsilon$)	91.8 ($<\varepsilon$)	100.5 ($<\varepsilon$)	72.1 (0.2)	50.4 ($<\varepsilon$)	46.4 (0.6)	168.8 (0.6)
HD210121	2.3 (0.3)	27.7 (0.5)	30.0 (0.8)	0.0 ($<\varepsilon$)	0.0 ($<\varepsilon$)	87.0 (5.7)	87.0 (5.7)
	7.7 (0.3)	8.2 (0.2)	15.9 (0.5)	4.6 (0.5)	0.2 ($<\varepsilon$)	257.3 (6.4)	262.1 (6.2)
VCT30	2.1 (0.6)	73.4 (2.7)	75.6 (2.3)	31.0 (7.1)	34.7 (2.4)	45.4 (5.8)	111.1 (9.2)
	12.4 (0.3)	73.4 (0.9)	85.7 (0.8)	22.1 (0.7)	7.0 (0.2)	34.9 (7.6)	64.1 (7.9)

Table 3.2: Si and C abundances resulting from the simple and detailed models for the average ISEC and for the lines of sight plotted in figure (3.4). All the abundances are expressed in ppM. We adopt $\varepsilon = 0.1$. This table is an excerpt of the online table (5) of Mulas et al. (2013).

Figure (3.6), compares the fitted values for omologous parameters obtained with the two models. These parameter values can be straightforwardly translated into abundances for the Si and C locked into classical dust grains. These are listed in the online table (5) of Mulas et al. (2013), of which table (3.2) is an excerpt. The same table lists the abundance of C locked in PAHs resulting from the simplified and detailed models and the total abundance of C.

On average, the simplified model seems to require a bit more C in PAHs. Again, figures (3.7) and (3.8) compare Si and C abundances resulting from the simple and detailed models for the whole set of lines of sight.

With our statistically large sample we find that abundances of elements locked in the classical dust component obtained with the simplified model are within a factor of ~ 2 of the ones derived using the detailed description. In particular, the simplified model yields Si abundance in dust almost always very close to 50 ppM, whereas this is more variable in the detailed model, ranging mostly between $\sim$20 and 70 ppM. The abundance of C locked in classical dust mantles shows larger variations in the statistical sample, but still the simplified versus detailed values are within a factor of ~ 2 of each other. In cases in which such accuracy (a factor of 2) is acceptable, it is therefore safe to use the simplified model to determine such parameters.

The abundance of C in PAHs is calibrated in the simplified model as proportional to the coefficient of the first Lorentzian (i. e. the bump). They are here also determined from the population of PAHs in the detailed model fits, and figure (3.9) shows the comparison, with superimposed the best–fitting straight line. That calibration relied solely on the integrated area of the first Lorentzian, disregarding the second Lorentzian and the cutoff at low energies (assumed because PAHs mostly do not absorb at wavelengths longer than the visible). It may be closer to physics to correlate the abundance of C in PAHs to their *integrated* absorption in the whole modelled range. We therefore computed this integral between 1 and 8.7 $\mu\mathrm{m}^{-1}$ (the observational range), and plotted it against the abundance of C in PAHs obtained from the detailed model in figure (3.10), along with the best fitting straight line. Indeed, points in figure (3.10) are more closely packed to the regression line with respect to figure (3.9). The regression line results to have a coefficient ~ 12 ppM μm mag^{-1}.

Abundances of C in PAHs obtained from the simplified model using only the fitted coefficient and the integral of both Lorentzians including cut–off are respectively within a factor of ~ 4 and ~ 2 of the ones obtained with the detailed one, across the statistical sample. Again, if such additional systematic uncertainty is acceptable, one can safely choose the simplified model over the detailed one for this purpose. In this case, however, we recommend to use the calibration on the integral of the simplified PAH absorption (including both Lorentzian and cut–off functions) instead of just the coefficient of the first Lorentzian, since this is both more accurate and unbiased, whereas using only the first Lorentzian will systematically overestimate C abundance in PAHs.

3.5.3 The charge of PAH mixture

Cecchi-Pestellini et al. (2008), first introducing the detailed model and applying it to a few lines of sight, obtained that whereas the detailed PAH composition is poorly constrained by the fit, some global properties of the mixture result to be relatively strongly constrained. This is most remarkably true for the total abundance of C atoms in PAHs, and for the average charge per carbon atom. We here go further, and try to understand whether, in each line of sight, PAHs appear to concentrate only in the

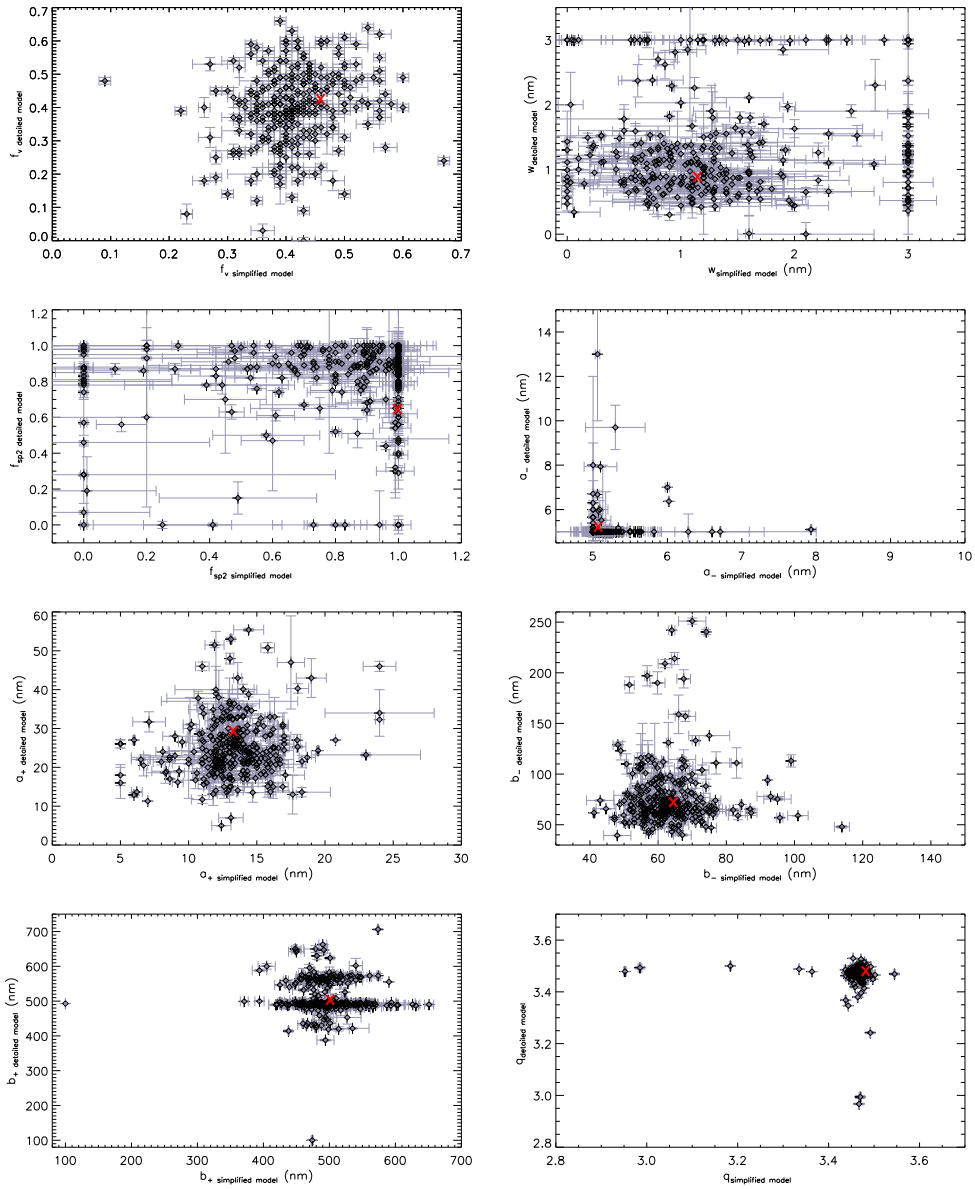

Figure 3.6: Comparison between homologous parameters obtained with the simplified and the detailed models. Values for the average ISEC are overplotted with a red "x".

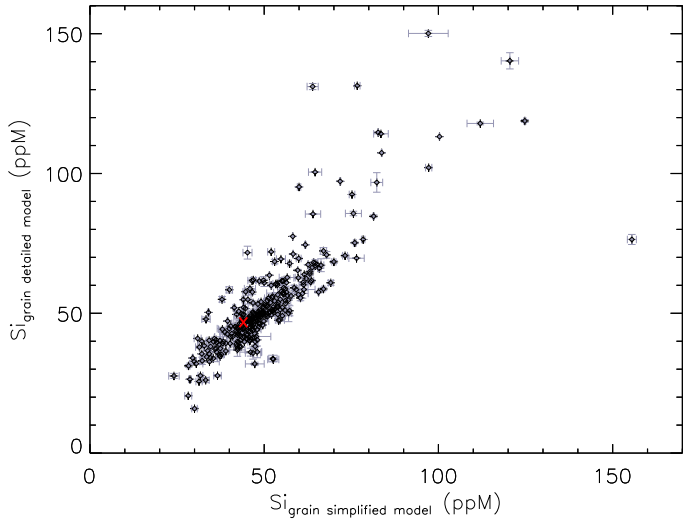

Figure 3.7: Comparison between Si abundances locked into classical dust grain obtained from the simplified and the detailed models. Values for the average ISEC are overplotted with a red "x".

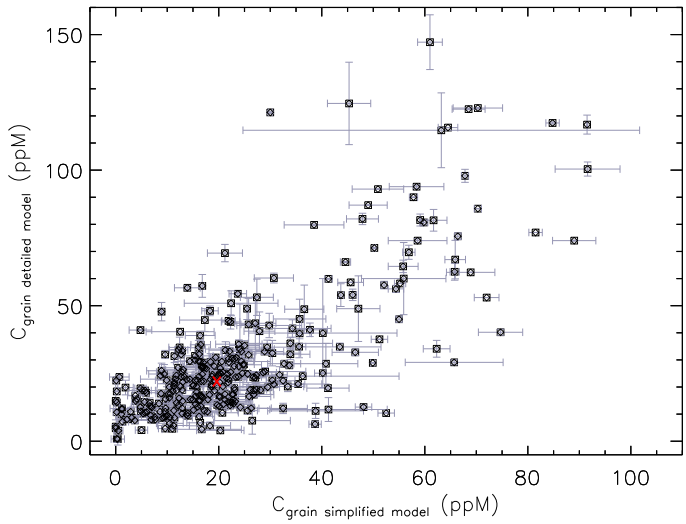

Figure 3.8: Comparison between C abundances locked into classical dust grain obtained from the simplified and the detailed models. Values for the average ISEC are overplotted with a red "x".

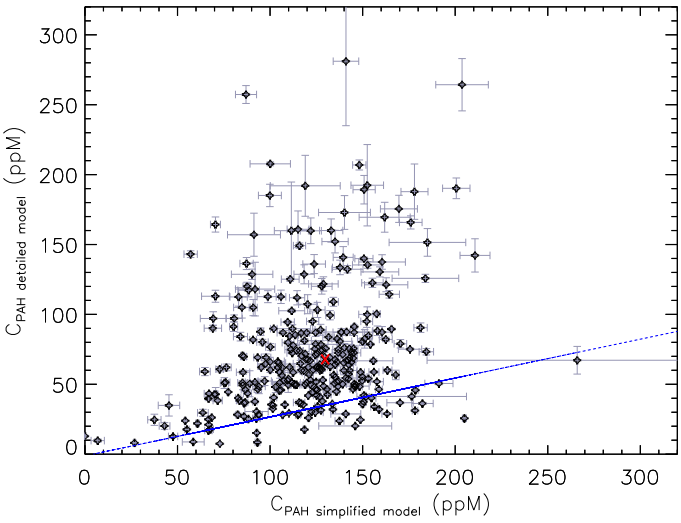

Figure 3.9: Comparison between C abundances locked into PAHs obtained from the simplified and detailed models. In the simplified version carbon abundances are proportional to Lp_1. Values for the average ISEC are overplotted with a red "x". Solid line: best fitting straight line.

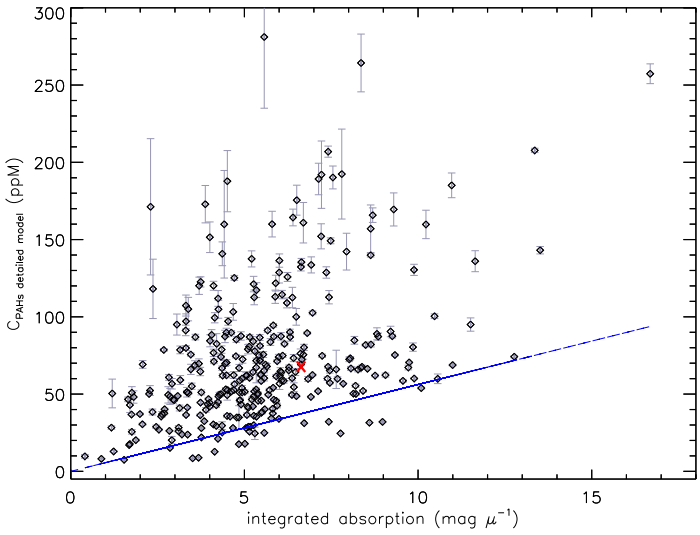

Figure 3.10: Comparison between C abundances locked into PAHs obtained from the detailed models and the integral of the "PAH" component of the simplified modes throughout the extinction curve, namely between 1 and 8.7 μm^{-1}. Values for the average ISEC are overplotted with a red "x". Solid line: best fitting straight line.

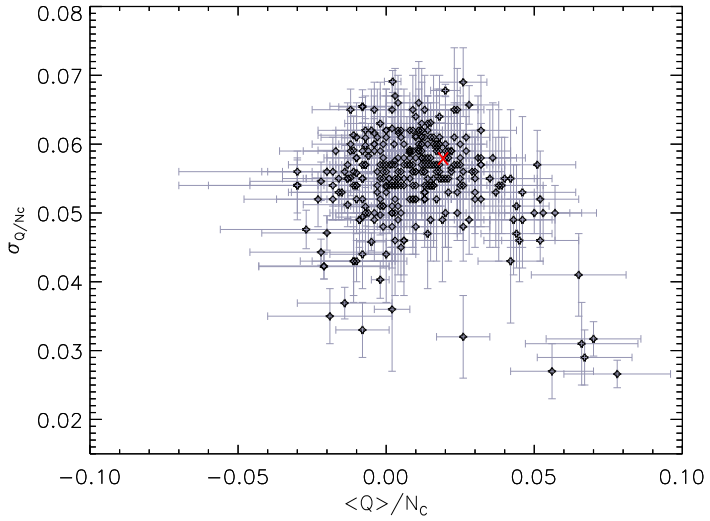

Figure 3.11: Average charge per C atom versus its RMS dispersion. Values for the average ISEC are overplotted with a red "x".

charge state closest to the average charge per C atom, or instead they spread over all charge states. To study this, for each line of sight we computed the RMS dispersion of the distribution of the charge per carbon atom. The obtained values are reported for the full set of lines of sight in the online table (6) of Mulas et al. (2013) of which table (3.3) is an excerpt.

Figure (3.11) plots the average charge per C atom versus its RMS dispersion. The RMS dispersion is mostly clustered around $\sim 0.6\ e^-/\mathrm{N_C}$, whereas the average charge ranges from ~ -0.5 to $\sim 0.9\ e^-/\mathrm{N_C}$. Since the PAHs in our mixture range in size from 10 to 66 C atoms, this corresponds to any fitted mixture to always include a little more than two charge states, with the average charge changes between lines of sight being significant with respect to its intrinsic dispersion.

LoS	$< Q > /N_C$	σ_{Q/N_C}
Average ISEC	0.017(0.012)	0.06(0.01)
HD12323	0.010(0.013)	0.06(0.01)
HD13659	-0.008(0.008)	0.0654(0.0014)
HD147165	0.028(0.007)	0.049(0.005)
HD151346	0.020(0.006)	0.060(0.007)
HD185418	0.032(0.008)	0.057(0.006)
HD197702	0.032(0.008)	0.057(0.003)
HD210121	-0.007(0.008)	0.0655442
VCT10	0.004(0.002)	0.0616(0.0014)

Table 3.3: Average charges per C atoms and RMS dispersions obtained with the detailed model for the average ISEC and for the lines of sight plotted in figure (3.4). This table is an excerpt of of the online table (6) of Mulas et al. (2013).

Cecchi-Pestellini et al. (2008) noted that on their small set of lines of sight the average charge per C atom appeared to correlate with the ratio c_4/c_3 of the c_4 and c_3 parameters of the Fitzpatrick and Massa (2007) parametrisation. In this parametrisation, the c_3 parameter is the bump intensity, while c_4 is the intensity of the non–linear FUV rise. The ratio c_4/c_3 is therefore highest for lines of sight with a bumpless extinction and large non–linear FUV rise (e. g., VCT10), whereas it is low for lines of sight with the reverse behaviour (e. g., HD 185418). Indeed, it is a known systematic spectroscopic trend that PAHs, with increasing positive ionisation, have a larger gap between the $\pi^\star \leftarrow \pi$ and the $\sigma^\star \leftarrow \sigma$ resonances (Cecchi-Pestellini et al., 2008). This trend has been found to become weaker for larger and larger PAHs (Steglich et al., 2011), because predictably one more or less electron makes less and less difference for a very big molecule with hundreds of electrons; however, this is balanced if one normalises charge to the number of C atoms in the molecule, as we do here.

Figure (3.12) shows the relation between the average charge per C atom and c_4/c_3 for all lines of sight. Lines of sight in different intervals of R_V are shown with different symbols and colours. Even simple visual inspection of figure (3.12) shows that there is *some* positive correlation, and that this changes somewhat with R_V. It is also apparent that there is a quite real scatter, which cannot be dismissed as just due to measurement and fitting errors. This tells us that PAH charge *does* play a role in determining the ratio between bump and FUV non–linear rise intensities, but it also tells us that it does not *solely* determine it. Indeed, it is instructive to examine the lines of sight with very weak bumps but steep FUV extinction in figure (3.4), and look in detail at the fitted PAH and classical dust contributions. One might naïvely expect to find a vanishing contribution from PAHs in these cases, which indeed are fitted, in the simplified model, by a vanishing first Lorentzian and a simultaneously large second one. Exploiting the full PAH representation, it is impossible to achieve such extreme ratios between the $\sigma^\star \leftarrow \sigma$ and $\pi^\star \leftarrow \pi$ resonances, which have only limited variability due to charge effects. Thus, even in bumpless extinction curves the PAH component is well present, but the $\pi^\star \leftarrow \pi$ PAH resonance is masked by the weak underlying classical extinction. Along bumpless lines of sight, in going from small to high energies, the extinction due to dust flattens under the bump region, and resumes its linear rise at higher energies, when extinction due to small particles kicks in. This happens because there is a wavenumber range in which extinction due to big grains saturates to its optical limit, and small particles do not contribute much yet.

This is consistent with observations showing sometimes quite non–negligible PAH *emission* from regions with bumpless extinction curves (see e. g. Paradis et al., 2011, Sandstrom et al., 2012). We conclude that there is an interplay between PAH charge state and classical dust size distributions in determining the observed c_4/c_3 ratios. This also explains the differences in figure (3.12) between subsets of lines of sight in different R_V intervals, since larger R_V values roughly translate into larger average grain sizes. From an observational point of view, bumpless extinction curves typically correspond to regions with harsher irradiation conditions. From a physical standpoint, this is expected to affect PAH charge state and dust size distributions. A large UV radiation density may destroy smaller dust particles, thus increasing R_V and the size gap between small and large dust grains. At the same time, an increase in the UV radiation density tends to move average PAH charge towards more positive values. However, in this case such effect can be balanced and/or masked by other environmental conditions, e. g., electron density and selective destruction of smaller PAHs (thereby decreasing the absolute value of average charge per C atom). It is therefore not surprising that it is not possible to find

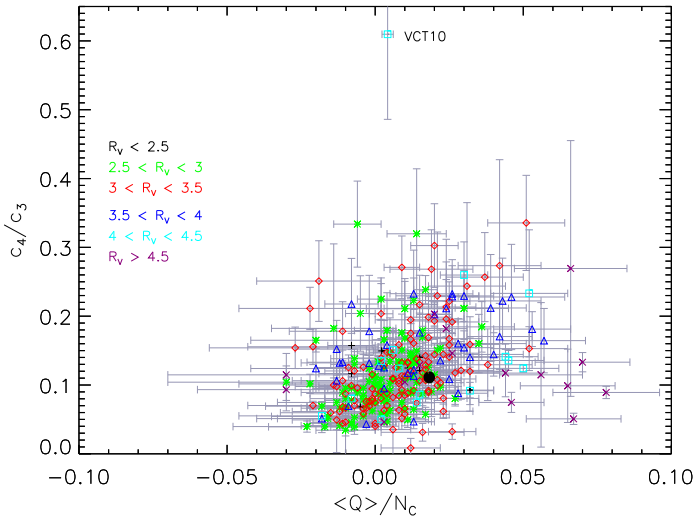

Figure 3.12: Relation between the average charge per C atom and c_4/c_3 for all lines of sight. Different symbols and colors refer to different intervals of R_V. Values for the average ISEC are overplotted with a black circle.

simple, perfect correlations relating individual Fitzpatrick and Massa (2007) empirical parameters and the more physical (albeit model–dependent) results from our fits.

As an example, figure (3.13) shows a 3–D plot with average PAH charge per C atom, gap of the dust size distribution, and c_4/c_3, seen from two different viewing angles. The points clearly do not occupy all space, but all three quantities relate together in an interdependent way.

A thorough analysis of the complex relations relating observational, empirical and "physical" (fitted) parameters requires applying appropriate statistical multivariate analysis techniques. This is definitely out of the scope of our work at this stage, and will be a starting point for next works discussions.

3.5.4 Detailed PAH composition: unconstrained

In the online figures from 2.1 to 2.329 of our paper: Mulas et al. (2013), the right panel shows an histogram with the average distribution of C among the PAHs we include in our model, in all four charge states, for each line of sight, along with the individual fits in left panel. An example is given in figure (3.14).

These kinds of histograms can be useful to explore trends among different PAH subgroups, for specific lines of sight. However, one should be well aware that *individual* PAH abundances are very poorly (if at all) determined by the extinction curve alone. This is clear if one inspects the covariance matrices of the C abundance in individual PAHs for an individual line of sight (all available as online material of the paper Mulas et al. 2013). To make this visually apparent, figure (3.15) shows one typical individual extinction curve (dotted line), along with its best fit (blue line), and the fit obtained by removing from the PAH mixture the species determined to be most abundant in the best fit, including $\sim$ 98% of the C in PAHs in the best fit. The left panel of

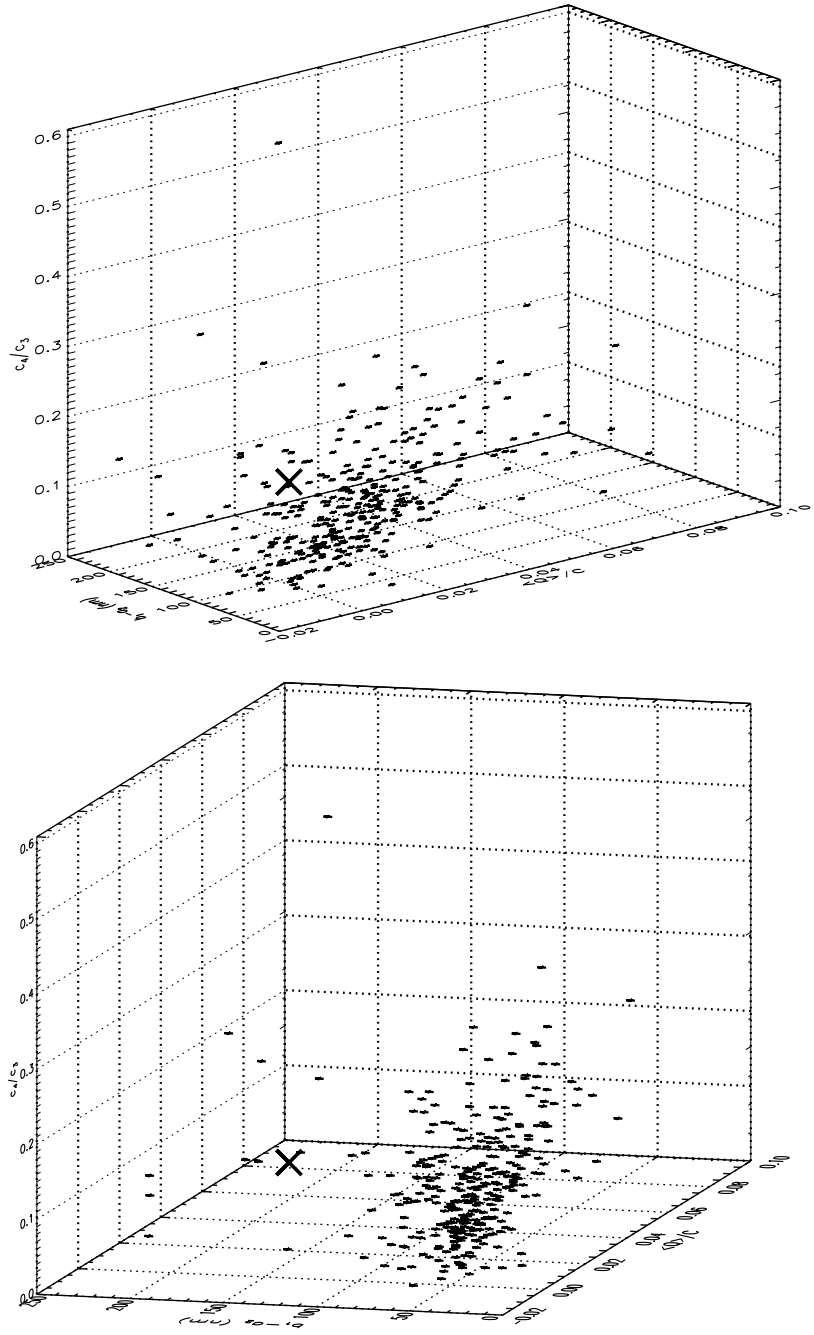

Figure 3.13: Occupation volume in the parameter space of the average PAH charge per C atom, the "missing grain" interval in the dust size distribution, and the observational ratio c_4/c_3. Values for the average ISEC are overplotted with an X.

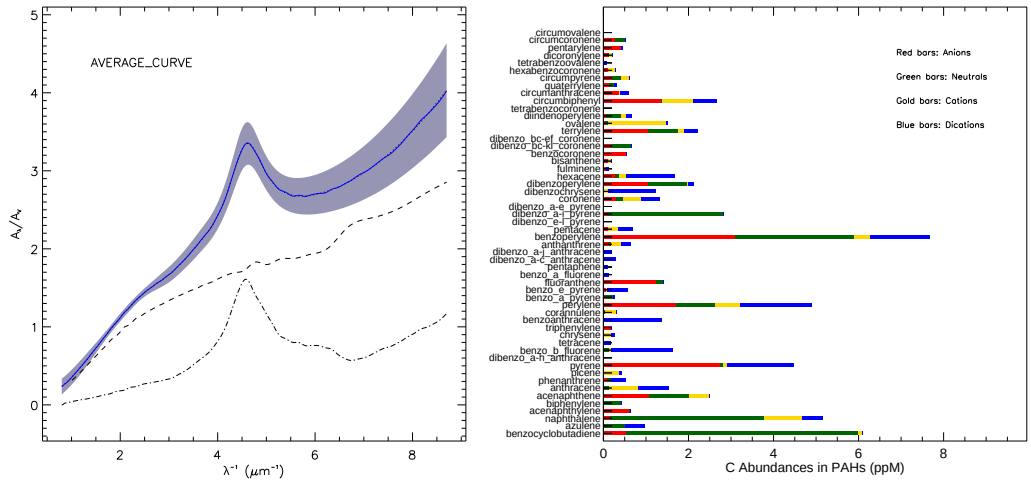

Figure 3.14: *Left panel*: Fit to the normalized extinction curve. Solid lines: fit; dashed lines: classical dust contribution; dot–dashed lines: PAHs. The lightly shaded area is the 1–σ observational error range given in Fitzpatrick and Massa (2007)). *Right panel*: histogram of Carbon distribution among synthetic PAH populations, averaged over their statistics.

figure (3.16) shows the histogram corresponding to the best fit, the right panel shows the same histogram for the "degraded" fit. The degraded fit is therefore obtained by deliberately including *only* those PAHs which were essentially absent in the best fit. In figure (3.15), with the same colour coding used for the fitted curves, we show the residuals (multiplied by 2 to make them more visible) of the two fits with respect to the observed extinction curve. It is clear that the red fit is still perfectly acceptable, despite our best efforts in deliberately sabotaging it. However, the total amount of C in PAHs and the average charge per C atom in PAHs is very nearly unchanged in the two fits, showing again that these quantities *are* well constrained by the extinction curve alone within our detailed model.

3.6 Discussion

In this work we systematically applied the $[CM]^2$ model to the 328 individual Galactic extinction curves observed by Fitzpatrick and Massa (2007). Most previous attempts to apply interstellar dust models to observations have been limited to the average Galactic ISEC or to a few individual directions. We demonstrate that our physical extinction model can successfully fit a very large sample of extinction curves without exceptions. It also brings forward the need for future modelling of interstellar matter to consider the number of free parameters as an important issue that should not to be neglected.

The results depicted in the preceding sections provide the first global characterization of the galactic extinction in terms of the physical parameters of a well–defined dust model, including a mixture of individual PAHs, described by their actual quantum properties. We found that solids and molecules are tightly coupled and both of them concur in the determination of interstellar extinction. Such conclusion is much

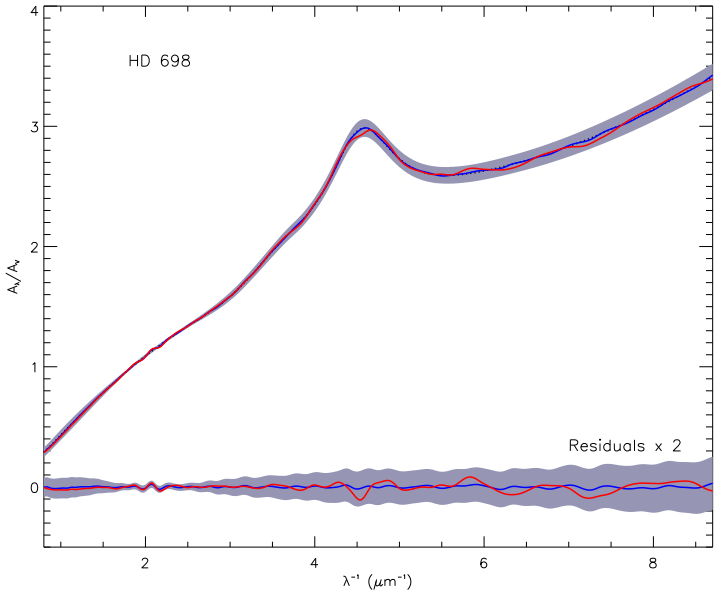

Figure 3.15: Best fit, its degradation, and residuals for the line of sight towards HD 698. Dotted lines: observational data; red lines: best fit: blue lines: degraded fits. Lightly shaded area: observational error range taken from Fitzpatrick and Massa (2007).

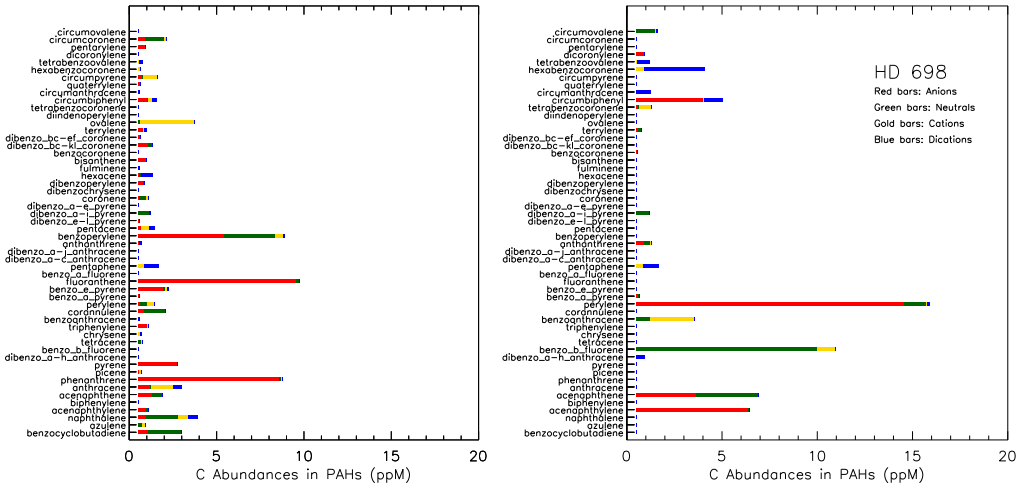

Figure 3.16: Distribution of Carbon among synthetic PAH populations for HD 698. *Left panel*: best fit; *right panel*: degraded fit (see text).

less obvious than what model assumptions would suggest. For instance, while in most of the cases dust grains provide the "perfect" baseline (in the spirit of the Fitzpatrick and Massa 2007 parametrization) for the PAH ensemble resonances, in a few "peculiar" lines of sight their extinction properties appear to hide the 217.5 nm feature.

The first and most evident result of this work is that the $[CM]^2$ model can adequately reproduce *all* the extinction curves in the Fitzpatrick and Massa (2007) sample. Such conclusion is not terribly exciting *per se*, and to some extent expected. Still, it is interesting that a physically simple model (despite the apparently large number of 225 free parameters) can match all observed variations. The physical simplicity of the model is promising for investigating how a small number of physical quantities, defining the environment, can drive the whole model to respond as a whole. This is the missing link needed to reconcile the unavoidable complexity of any phisical model with the small number (less than six) of empirical parameters necessary to account for observations(Cardelli et al. 1989, Fitzpatrick and Massa 2007, Krełowski and Strobel 2012). This will also make it possible to investigate the conditions that characterise the observational exceptions, i.e. the lines of sight which fail to be fitted by empirical parametrizations (e.g. HD 210121).

The present modelling effort already produced a number of direct and indirect results providing a starting point for future investigations. Our results can be summarized as follows.

1. The total number of C atoms locked in both solids and molecules is largely consistent with the available interstellar budget. Conversely, this model requires somewhat too much Si for a consistent fraction of the 328 observed lines of sight (see figure 3.17). The average Galactic ISEC falls close to elemental constraints. However, our use of old optical constants for dust materials (i. e., Draine 1985, Rouleau and Martin 1991, Ashok et al. 1991) probably contributes in exhausting the available atoms. Indeed, Zubko et al. (2004), using a revision of the Rouleau and Martin (1991) optical constants were able to put forward an interstellar dust model whose results are consistent with interstellar element abundances. Moreover, we emphasize that our fitting algorithm aims at the very best match with the observed ISEC, with no regard to abundance constraints, obtaining an unrealistically perfect match. It would be easy to substantially reduce the required abundance of C and Si at the price of a slightly worse fit, but still largely compatible with observations within measurement errors. As an example we consider the case of BD+56518; in the previous chapter we derived a fit much less constrained than the one derived here (but still smoothly within 1 σ); such a description led to the exploitation of 5 ppM of Si, 6 ppM of Carbon in classical grains, and 48 ppM of Carbon in PAHs. On the other hand, from the data in the online table (5) of Mulas et al. (2013), we find corresponding abundances of 34 ppM (Si), 13 ppM (C), and 127 ppM (C), respectively. In future works, we may introduce in the fit an increasing χ^2 penalty term for abundances increasingly exceeding observational constraints.

   In any case, the use of the sole average Galactic ISEC does not provide a reliable validation of dust models; in particular, chemical and physical characteristics of specific lines of sight, such as e. g., metal abundances, should be included in the endorsement process.

2. In the UV, classical dust grains contribute an almost gray baseline to the extinction for the totality of lines of sight explored in this work. Again, such result is not

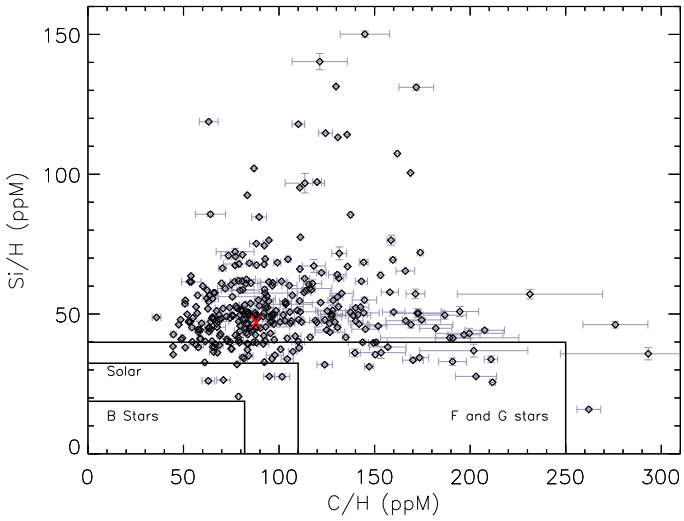

Figure 3.17: Total Si and C abundances in ppM. The red cross represents the average ISEC. Boxes refer to observational constraints: solar taken in Asplund et al. (2009), Mathis (2000) and Be, F and G stars from Zubko et al. (2004).

totally unexpected, and it reflects the *a priori* choice of the bump carriers with respect to the Fitzpatrick and Massa (2007) parametrization of ISECs. Despite the apparently large number of free parameters, the model is far from being infinitely flexible, because many of such parameters control the extinction properties of the mixture within a stiff class of morphological profiles. The visible part of any ISEC is mainly produced by the large size part of the dust distribution, while the UV rise is due to the contribution of small grains and PAHs floating on the top of the flat, saturated extinction of the large ones. In other words, dust grains are "forced" to behave in this way, in response to the shape of the convolved $\pi^\star \leftarrow \pi$ and $\sigma^\star \leftarrow \sigma$ resonances of the PAH ensemble. This implies that the description of classical dust grains is far from be unique, and is poorly constrained by the data, as long as the "correct" size distribution is employed. This is not a new concept, but it is here validated against a statistically relevant sample of lines of sight.

3. In spite of the detailed PAH chemical composition being poorly constrained by extinction data, some global properties of the molecular ensemble *are* well determined, e. g., the column density of Carbon atoms locked in PAHs, and the mean charge of the molecular mixture. By contrast, individual species are interchangeable and expendable, and no individual property is highlighted by the fitting procedure. We conclude that many loose mixtures of a relatively small number of PAHs may reproduce the features of the extinction curve in the UV, without significant losses in the accuracy of the description. Unfortunately, such conclusion opens out to the more general question of the stability of the 217.5 nm feature: why should a random assembling of different molecules provide the same extinction profile, modulo the differences in the profile width, along different lines of sight? We know that not all the linear combinations of PAHs are consistent

with the interstellar features (e. g., Malloci et al. 2007). A similar problem is posed by models considering graphite grains responsible of the 217.5 nm feature. Extinction calculations indicate that graphite particles must exist in a relatively narrow size range and be almost spherical in shape (Draine, 1988). As a consequence, the straight assumption of a set of PAHs as bump carriers appears to be at best somewhat artificial. If a set of PAHs (such as we find) were indeed to produce the observed extinction, there must be a (heretofore unknown) chemical selection mechanism at work.

4. We found that, in the framework of our model, bumpless extinction curves are not necessarily lines of sight devoid of PAHs, but rather that the $\pi^\star \leftarrow \pi$ PAH absorption can be very effectively masked by a large gap between the maximum size limit of small dust grains and the minimum size limit of large ones. Thus, the present model was here proven to be sufficient, without additional components, to fit all observed extinction curves. On the other hand, the previous discussion makes such conclusion suspicious, unless bumpless extinction curves could be defined *only* with respect to the properties of classical grains. A possible observational test would be to look for some peculiar ISEC with a "dip" in the bump regions, which would be observable if the "hole" in the dust grain size distribution and the mixture of PAHs do not perfectly cancel each other in a smooth extinction curve.

   When extinction curves are very steep (e.g, HD 62542) the weakness of the bump may be apparent, being an artefact of the normalization (Fitzpatrick, 2004). However, such suggestion may fail in explaining the weakening of the bump in the flattest (highest R_V) extinction curves, such as HD 29647. Whatever the case may be, suppression of the $\pi-$plasmon resonance in small carbon particles can be obtained by increasing the density of sp^3 bonds (e. g. Jones et al. 1990, Duley 2006a). This may suggest super–hydrogenation (Hecht, 1986) or the presence of a fraction of carbon in nanodiamonds (e. g., Rai and Rastogi 2010).

5. The numerical tendency to go below the lowest limit of 5 nm in particle size in a significant number of fitted lines of sight (and some physical sense) suggests the presence of an additional component of very small grains. Such particles might be carbon mantle fragments, possibly produced during some destructive events, or an independent population of very small carbonaceous grains (Desert et al., 1986). Such very small particles are unlikely to include silicates, since they would be stochastically heated by single photon absorption events and would produce significant emission in silicate bands, which is not observed; still, Li and Draine (2001b) argued that a small amount of very small silicatic grains might be present. In a dynamical scenario, this "mesoscopic" carbonaceous component, heated in a hydrogen plasma (e. g., shocks) may rearrange some of its carbon skeletons from sp^2 to sp^3 bondings (e. g., Landstrass and Ravi 1989, Furton and Witt 1993). Such processed particles would be partially aliphatic and therefore would have optical properties qualitatively different from a superposition of PAH cross–sections; they might provide an efficient extinction in the FUV without the bump at 217.5 nm (as implicitly suggested by the results of simplified version model). In different physical conditions, some of the very small carbonaceous grains might instead evaporate, producing PAHs, as suggested by Cesarsky et al. (2000) and supported by observational evidence in some environments (Rapacioli et al., 2005, Berné et al., 2007).

6. We highlighted that the ratio between the observed intensities of the non–linear FUV rise and of the UV bump results from the combined effect of PAH charge on PAH absorption features and from changes in the classical dust size distributions, in a complex interplay. This behaviour, together with the variations of the spectral properties of PAHs in different charge states (see figure 1 in Cecchi-Pestellini et al. 2008) naturally lead to the observed weak anti–correlation between non–linear FUV rise and of UV bump intensities.

Chapter 4

The evolving dust

4.1 Introduction

The life cycle of cosmic matter is closely related to the cycle of the ISM and of our Galaxy. During its lifetime, dust grains are affected by many processes as they go from diffuse to dense clouds or during the collapse of dense molecular clouds. These processes may destroy the grains, violently, by shattering, or more gently, by sputtering, determining e.g., their size distribution. The wide variations of ISECs in the MWG (Fitzpatrick and Massa, 2007) and other galaxies (e.g., Maíz Apellániz and Rubio 2012) may, thus, reflect the intrinsic variability expected from an ISM with a wide range in physical properties and grain–processing histories. Since such processes are random in nature, it may appear difficult to reconcile the remarkable variations of the interstellar extinction profiles within an unified scheme. Still, ISECs have been shown to be characterised by a very small number of regulatory parameters (e.g., Valencic et al. 2004).

The models originating with Jones et al. (1990) and pursued in detail by Cecchi-Pestellini and Williams (1998) and Cecchi-Pestellini et al. (2010) claim that the physical and chemical nature of grains – and in particular their optical properties – respond to the local physical conditions in the diffuse ISM and evolve in time. Carbon in the H–rich diffuse interstellar gas is deposited on silicate dust grains initially in the form of sp^3 hydrogenated amorphous carbon (see Section 1.7.2). The interstellar radiation field then progressively processes this material into a H–poor sp^2 carbon on a time scale expected to be less than or about one million years. The reverse re–hydrogenation reaction also takes place, driven by accretion of hot hydrogen atoms, so that the net rate of graphitisation results from the competition between the two opposite processes, depending on local conditions. The deposition time is on the order of a few Myr for typical number densities, while removal of the carbon by relatively low–velocity shocks is probably on the same timescale. In this scenario, therefore, the extinction caused by such grains varies with time. We aim to show that the changing nature of the ISEC may be understood, within the framework of such a model, as a manifestation of the evolution of carbon in the ISM, which in turn depends mainly on the relative abundances of sp^2 and sp^3 bonding sites (e.g., Chiar et al. 2013). Our conclusions are based on the global characterisation of the galactic extinction (although limited to just two kpc around the Sun's location in the MWG) in terms of the physical parameters of the $[CM]^2$ dust model performed by us in the previous chapter.

The interpretation of the obtained parameter values, from the fit of 328 ISECs by

means the [CM]^2 dust model, requires an underlying chemical and physical description of the properties of dust materials, and of their response to the local physical conditions along specific lines of sight. In the light of such a physical interpretation, each set of fitted parameters is the product of the history of a given dust population, and can be used to tell its tale. We here derive a model of the evolution of dust particles, and compare its predictions with the results of the previous chapter. It is well–known that changes in the optical properties of hydrogenated amorphous carbon are driven by UV irradiation and thermal annealing processes (Iida et al., 1984, Robertson, 1991). Such events occur in space mainly in response to UV radiation fields (Jones, 2012a). We model the process considering gas–phase carbon progressively deposited on silicate cores. Initially, mantles are assumed to be H–rich amorphous carbon. This assumption is the natural consequence of deposition occurring in an atomic H–environment. Simultaneous UV processing of this material forms two distinct concentric shells, connected by a fuzzy transition layer to account for carbon mantle formation by successive deposition of atoms (see Iatì et al. 2008, for details). If the annealing time–scale is much faster than deposition, or when the available gas–phase carbon is exhausted, the outer sp^3 layer becomes vanishingly thin. If, conversely, the annealing time–scale is much slower than deposition, the H–rich carbon mantle will become optically thick in the UV, so that sp^3 layers deeper than approximately 20 nm will be shielded and will not be further processed (Jones, 2012b). Although simplified, this approach allows to follow in fair detail the compositional and structural evolution of dust carbonaceous materials, and their impact on the optical properties of dust.

Recently, Jones et al. (2013) put forward a dust model in which aliphatic carbon deposition is assumed to occur in dense clouds, whereas processing occurs in diffuse clouds. Moreover, they include a population of large carbonaceous grains, initially H–rich before processing. For the thick aliphatic mantles they assume to be deposited in dense clouds, and even more so for big carbonaceous grains, self–shielding is an issue, and under their assumptions is reasonable to expect more processed material in outer layers and less processed material inside. Actually, one would expect even an onion structure, when more cycles accumulate. If it is assumed that in diffuse interstellar regions photo–processing rates are enough fast, the outer layer of freshly deposited, still unprocessed, aliphatic material would be so thin to be negligible.

In the present evolutionary model of mantle accretion and processing, which we consider to occur in the diffuse to translucent ISM (i. e. not in molecular dense clouds), we allow for an ample range of densities and radiation field intensities, and quantitatively follow the time evolution of grain mantles, using a time–dependent gas–phase chemistry model to determine the time–dependent deposition rate. This is a significant difference from Jones et al. (2013) model, in which mantle thickness and the fraction of processed vs. unprocessed carbon are not allowed to vary but stem from assumptions.

Our purpose is giving a physical interpretation of the observed visible–UV extinction curves in Fitzpatrick and Massa (2007) as fitted in the previous chapter with the [CM]^2 model. All of these lines of sight have a relatively low extinction, which is an obvious observational bias due to the availability of UV observations. This observational bias, however, translates in a physical one: each low extinction line of sight in the solar vicinity is more sensibly representable with a single set of dust model parameters. It would be conceptually wrong and physically meaningless to try to use such a simplistic representation to interpret any observations of lines of sight with a much larger extinction, unless there are strong reasons to believe that it is specifically dominated by a single, remarkably uniform set of conditions across the whole line of sight. Reality is usually

more complicated, as in heavily reddened lines of sight there is typically a superposition of numerous interstellar clouds with more or less widely different physical conditions.

4.2 The model of interstellar dust evolution

4.2.1 Outline

Initially, the silicate cores are assumed to be bare. Then, carbon is deposited kinetically from the gas with a rate depending on gas density and temperature. The resulting solid carbon layer is assumed, at the deposition, to be hydrogen–rich and sp^3 bonded. UV irradiation of the H–rich polymeric carbon will reduce the H–content and lower the bandgap energy, making the material appear more graphitic, increasing the absorption of such material in the visible, and causing luminescence in the IR. Conversely, the exposure of graphitic carbon to hot H atoms can reverse the process: the carbon becomes richer in hydrogen, the bandgap increases, the material absorbs more strongly in the UV and luminescences in the visible with high efficiency. Strong UV processing (e.g., in photon–dominated regions) and sufficiently elevated temperatures (e.g., during a shock) will remove the carbon mantles entirely in the form of carbon atoms and ions, carbon molecules and radicals and polycyclic aromatic hydrocarbons (PAHs).

Such a cycle of carbon in and out of dust is described by a set of ordinary differential equations, that follows the evolution in time of the available carbon fraction $x_{\rm C}$, the deposited polymeric sp^3 carbon fraction x_{sp^3}, and its radiation annealed sp^2 counterpart x_{sp^2}

$$\begin{cases} \dfrac{{\rm d}x_{\rm C}}{{\rm d}t} = -\left(A + k_{\rm chem}\right) x_{\rm C} \\ \dfrac{{\rm d}x_{sp^3}}{{\rm d}t} = A x_{\rm C} - t_{\rm pd}^{-1} x_{sp^3} + k_{\rm H^\star} x_{sp^2} \\ \dfrac{{\rm d}x_{sp^2}}{{\rm d}t} = t_{\rm pd}^{-1} x_{sp^3} - k_{\rm H^\star} x_{sp^2} \end{cases} \tag{4.1}$$

together with the normalisation condition $x_{\rm C} + x_{sp^3} + x_{sp^2} + x_{\rm gp} = 1$, $x_{\rm gp}$ being the fractional abundance of gas–phase carbon. The system (4.1) is coupled with an additional equation for the evolution of carbon column density of the material composing the mantle $N_{\rm C} = \delta_{\rm C} \times w$. Since both mantle density and thickness are functions of time we derive the mantle width evolution as follows

$$\begin{aligned} \frac{{\rm d}N_{\rm C}}{{\rm d}t} &= w\frac{{\rm d}\delta_{\rm C}}{{\rm d}t} + \delta_{\rm C}\frac{{\rm d}w}{{\rm d}t} = D\, x_{\rm C} \\ \frac{{\rm d}w}{{\rm d}t} &= \left(\frac{D}{\delta_{\rm C}}\right) x_{\rm C} - \left(\frac{w}{\delta_{\rm C}}\right)\frac{{\rm d}\delta_{\rm C}}{{\rm d}t} \end{aligned} \tag{4.2}$$

Equations (4.1) and (4.2) are linked to a set of chemical rate equations describing gas–phase chemistry. In equations (4.1) $A = \xi v_{\rm C}\left(\langle\sigma_d n_d\rangle/[{\rm H}]\right) n_{\rm H}$ with ξ the carbon sticking coefficient, $v_{\rm C} = \sqrt{8kT_{\rm k}/\pi m_{\rm C}}$ the C–grain relative thermal velocity, $\langle\sigma_d n_d\rangle/[{\rm H}]$ the C–dust collision rate per nucleon averaged over the dust size distribution, and $n_{\rm H}$ the total number density of H nuclei. $k_{\rm chem}$ is a cumulative chemical rate for the formation of carbon–bearing gas–phase species such as CO, $k_{\rm H^\star}$ the $sp^2 \rightarrow sp^3$ conversion rate via hot atomic H insertion in the aromatic matrix, and

$$t_{\rm pd}^{-1} = \int \sigma_{\rm pd}(\nu) I_{\rm ultraviolet}(\nu.\Omega) {\rm d}\nu\, {\rm d}\Omega \tag{4.3}$$

the photo–darkening rate, $\sigma_{\rm pd}(\nu)$ and $I_{\rm ultraviolet}$ being the photo–darkening cross–section (e.g., Mennella et al. 2001) and the interstellar UV radiation field, respectively. In the Section (1.3) we reported as the absorption coefficient changes in carbon materials exposed to irradiation. In the simplified description adopted here, in which we consider only the extreme cases of sp^3 and sp^2 material, $t_{\rm pd}$ quantitatively determines the timescale for UV irradiation to transform the former in the latter.

Finally, in equation (4.2) the coefficient $D = v_{\rm C} m_{\rm C} \mathcal{A}_{\rm C} (1 - f_{\rm PAH}) n_{\rm H}$ is the mass accretion rate over a spherical surface, derived assuming grains of different sizes to accrete mantles with the same thickness (Whittet, 2002). In this definition $\mathcal{A}_{\rm C}$ is the total carbon elemental abundance and $f_{\rm PAH}$ is the fraction of carbon in PAHs. Since the two forms of carbon, amorphous and polymeric, have different mass densities, $\delta_{sp^2} = 2.26$ g/cm^3 (graphite) and $\delta_{sp^3} = 0.901$ g/cm^3 (polyethylene), respectively, the mantle density $\delta_{\rm C}$ is time–dependent (see the second term in the rhs of equation 4.2). We do not consider PAH accretion onto dust surface, that is likely to occur but with a marginal rate with respect to atomic C collisions.

The term $k_{\rm chem}$ summarizes a simple chemical network constructed from 139 species consisting of the elements H, He, C, O, N, and S. With the exception of carbon, the concentrations of the elements relative to H, equal to 10^5 (He), 200 (O), 50 (N), and 3 (S) ppm, refer exclusively to the abundances in the gas–phase. The total concentration of C, in both gas– and solid–phases, is $\mathcal{A}_{\rm C} = 225$ ppm (Snow and Witt, 1996). Estimating the absolute abundances of the elements in the ISM is a difficult task, and here we operate a conservative choice. We note that the increase, or decrease, of the available gas–phase carbon is not linearly reflected in the mantle accretion rate, which depends on the product of $\mathcal{A}_{\rm C}$ and the carbon sticking coefficient ξ, with this latter quantity determined by the observationally inferred CO concentrations.

We select from the UDFA data file (Woodall et al., 2007) all the reactions which couple the species, for a total number of ~ 2000 reactions. The cosmic ray ionisation rate is $4 \times$ the standard UDFA value, i.e., $\zeta = 5 \times 10^{-17}$ s^{-1}. The chemical abundances have been checked for consistency, but exploited only to derive the value of the sticking coefficient consistent with the presence of the observationally determined abundance of CO in molecular clouds, $\xi \leq 0.1$. The chemical model is described elsewhere (Casu et al., 2001). It consists in a time–dependent photon–dominated region code that, for the present calculation, we integrate up to $A_V = 1$ mag, for a two–sided illuminated cloud.

Equations (4.1) and (4.2) should be supplemented with suitable terms describing mantle sputtering or evaporation in shocks or other destructive events (e.g., Jones et al. 1994). However, here we follow dust and chemistry evolution for one cycle at a time. We also do not explicitly include re–hydrogenation and set $k_{\rm H^\star} = 0$. Starting with bare silicate cores, the initial conditions at $t = 0$ are $x_{\rm C} = 1$, $x_{\rm gp} = 0$, $w = 0$, and $x_{sp^3} = x_{sp^2} = 0$. Destructive events are taken into account by abruptly removing part of the mantle, leaving a remnant with an arbitrary sp^2/sp^3 ratio, and resuming the evolution from these new initial conditions.

4.2.2 Properties of the solutions

Equations (4.1) and (4.2) can be recast more compactly. First we decouple gas–phase chemistry from carbon accretion on dust surfaces by subtracting from the total carbon abundance the gas–phase component, and setting $k_{\rm chem} = 0$. Then, rescaling the integration variable to ${\rm d}s = T_{\rm k}^{1/2} n_{\rm H} {\rm d}t$, and incorporating into the newly defined carbon

elemental abundance $\hat{\mathcal{A}}_{\rm C}$ the factor $(1 - f_{\rm PAH})$ we obtain

$$\begin{cases} \dfrac{{\rm d}x_{\rm C}}{{\rm d}s} = -\hat{A}x_{\rm C} \\ \dfrac{{\rm d}x_{sp^3}}{{\rm d}s} = \hat{A}x_{\rm C} - s_{\rm pd}^{-1}x_{sp^3} \\ \dfrac{{\rm d}x_{sp^2}}{{\rm d}s} = s_{\rm pd}^{-1}x_{sp^3} \\ \dfrac{{\rm d}w}{{\rm d}s} = \left(\dfrac{\hat{D}}{\delta_{\rm C}}\right)x_{\rm C} - \left(\dfrac{w}{\delta_{\rm C}}\right)\dfrac{{\rm d}\delta_{\rm C}}{{\rm d}s} \end{cases} \tag{4.4}$$

where $x_{\rm C} + x_{sp^3} + x_{sp^2} = 1$, $\hat{A} = (8k/\pi m_{\rm C})^{1/2}\left(\langle\sigma_d n_d\rangle/[{\rm H}]\right)$, $\hat{D} = (8km_{\rm C}/\pi)^{1/2}\hat{\mathcal{A}}_{\rm C}$, and $s_{\rm pd} = (T_{\rm k}^{1/2}n_{\rm H}/\chi)t_{\rm pd}$ is the rescaled photo–darkening time, with χ the increase of the interstellar UV radiation field $I_{\rm ultraviolet}$ with respect to the interstellar standard value. We have, thus, a one–parameter system of differential equations, which can be easily integrated numerically. Solutions starting from the same initial conditions, but with different $s_{\rm pd}$ values, have no other points in common but the starting point and the asymptotic limit ($s \to \infty$).

This is apparent from figure (4.1), which shows in each panel the evolutionary tracks resulting from a set of initial conditions. We plot the quantity $f_{sp^2} = \delta_{sp^2}x_{sp^2}/(\delta_{sp^2}x_{sp^2} + \delta_{sp^3}x_{sp^3})$, a function of the parameters of the present evolutionary model, to make possible a direct comparison with the results of the ISEC fitting procedure (see Chapter 3). We chose five initial conditions, and for each one we produced curves corresponding to a grid of sensible values of the only free parameter $s_{\rm pd}$. From the evolutionary point of view, the curves in left top panel of figure (4.1) represent the initial evolution from pristine, naked silicate grains, i. e. the very first cycle in the life of an interstellar grain. The other cases represent the evolution of grain mantles restarting after a mantle–shattering event. In such a case, a small layer of residual mantle is left, which may have been rehydrogenated to some extent by impinging hot H atoms in the same event. In the plot, we also show the iso$-s$ curves, relating different evolutionary tracks at the same values of the evolution parameter s. Curves in the same panel never intersect, and are thus invertible for given initial conditions. Inverting them a (scaled) evolutionary time, $s_{\rm ev}$, is derived from the knowledge of e.g., x_{sp^2} and w for any value of $s_{\rm pd}$.

We consider $\hat{\mathcal{A}}_{\rm C}$ to be constant along different lines of sight. This is not a strong approximation as $\hat{\mathcal{A}}_{\rm C}$ may vary a factor of $2 - 3$ in the local ISM (e.g., Zubko et al. 2004), and the mantle accretion rate, $\hat{D}$, depends linearly by this factor. With such assumption, the initial conditions in cases of partial removal of carbon mantles are easily constructed just deriving the fractional amount of carbon in the mantle leftover, x_w, and setting $x_{\rm C} = 1 - x_w$.

We remark that equations (4.4) are, strictly speaking, part of a much larger system of differential equations, which includes also the time–dependent chemical evolution model to which they are coupled. This is the reason why evolutionary tracks computed the same value of $s_{\rm pd}$, but with different initial conditions (i. e. curves of the same color in different panels of figure 4.1) may intersect (and indeed some do). This does not contrast with the unicity of the solutions of a set of differential equations, because what intersects are not distinct, complete many–dimensional solutions of the whole system (which indeed either never intersect or are entirely coincident), but rather their projections onto the much smaller $w - f_{sp^2}$ plane.

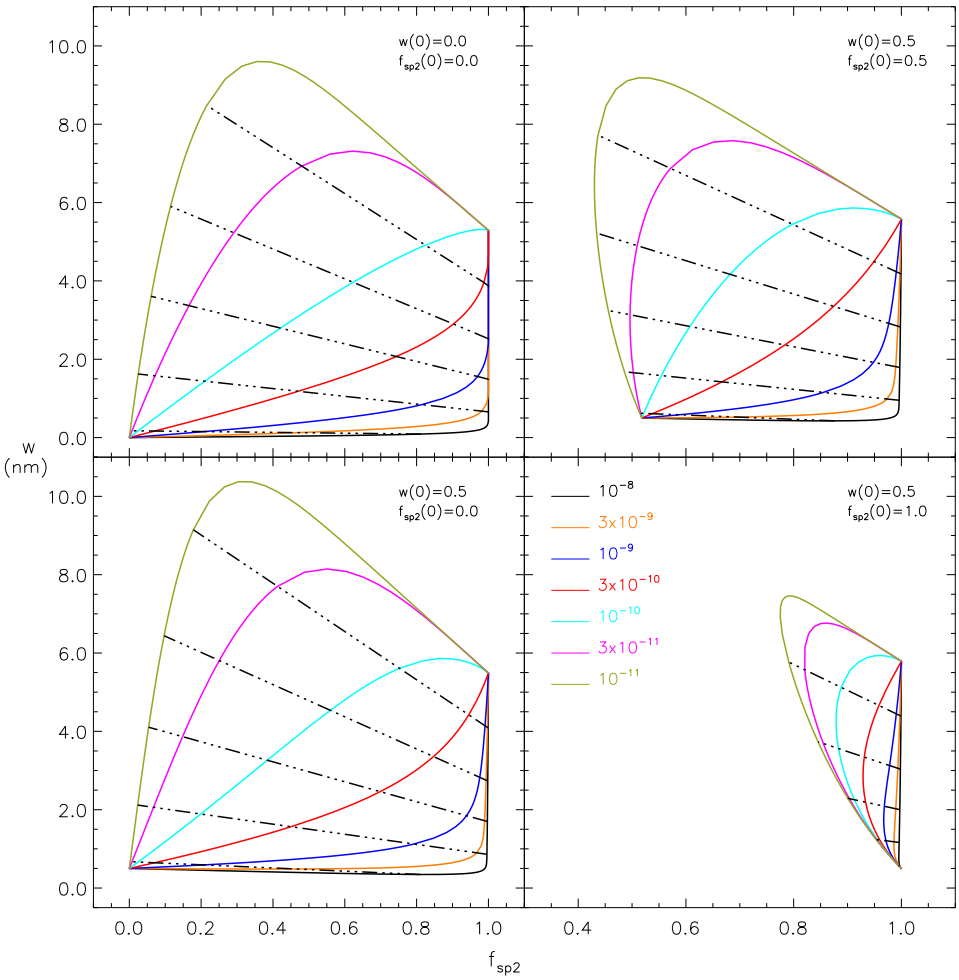

Figure 4.1: Theoretical distribution of mantle thickness w and normalized sp^2 mantle carbon fraction, $f_{sp^2} = \delta_{sp^2} x_{sp^2} / (\delta_{sp^2} x_{sp^2} + \delta_{sp^3} x_{sp^3})$. Evolutionary tracks are shown as solid lines starting from different initial conditions (see Eq. 4.4). (a): $(f_{sp^2}, w) = (0, 0)$; (b): (0,0.5); (c): (0.5,0.5); (d): (1,0.5). Each curve is labelled by the value of the rescaled photo–darkening rate $s_{\rm pd}^{-1}$ in cm^3 K$^{-1/2}$ y^{-1}. Dashed lines trace the iso–s curves.

Finally, we estimate the asymptotic mantle thickness for a line of sight from the approximate analytic solutions derived in the appendix B, equations (B.1), with $x_{\mathrm{C}} \sim 0$

$$w \sim \frac{\hat{\mathcal{A}}_{\mathrm{C}}}{\langle \sigma_d n_d \rangle / [\mathrm{H}]} \times \left(\frac{\delta_{\mathrm{C}}}{m_{\mathrm{C}}} \right)^{-1} = 0.54 \times \left(\frac{\hat{\mathcal{A}}_{\mathrm{C}}/\mathrm{ppm}}{R_V} \right) \mathrm{nm} \tag{4.5}$$

where we substitute $\langle \sigma_d n_d \rangle / [\mathrm{H}] \sim R_V / 6.4 \times 10^{21}$ cm^2, and $\delta_{\mathrm{C}} = \delta_{sp^2}$. Using $R_V = 3.1$ and $\hat{\mathcal{A}}_{\mathrm{C}} = 20$ ppm (the value for the average galactic ISEC deduced by online table 4 of Mulas et al. 2013) we find $w \sim 4$ nm (see figure 4.1).

4.3 Observational data

In the previous chapter we performed fits of 328 ISECs, parametrized by Fitzpatrick and Massa (2007), with our [CM]^2 model in the simplified and detailed version. As showed in the Section (3.5.2) the two versions, despite the apparent similarity, are qualitatively different in the molecular representation. So, while both the simplified and the detailed [CM]^2 model fit equally well all ISECs, the molecular component of extinction has somewhat different degrees of freedom (reflecting different underlying physical assumptions), resulting also in different parameters for the classical component.

Fig. 4.2 displays w versus f_{sp^2}, derived by online tables of Mulas et al. (2013) for the Fitzpatrick and Massa (2007) extinction curve sample. The left panel shows the results for the simplified [CM]^2 model, the right panel for the detailed one. The difference between the left and right panels of figure (4.2) is remarkable: the left panel shows markedly more scatter in particular in the left part of the plot where the evolutionary effects have more impact on the $f_{sp^2} - w$ distribution, while data points in the right panel appear to be more tightly constrained in a well–defined relatively small part of the $w - f_{sp^2}$ space. This difference stems from assuming, in the right panel, the molecular component to absorb light as a collection of aromatic moieties, whereas in the left panel the $\pi^\star \leftarrow \pi$ and $\sigma^\star \leftarrow \sigma$ resonances are allowed to vary independently.

While we fitted the extinction models solely on visible and UV extinction curves, the resulting models also yield the predicted extinction in the IR, including the so–called aliphatic C–H stretch feature around 3.4 μm. Since the extinction in the IR is much smaller than that in the UV, the UV extinction curve and the 3.4 μm feature are almost never observed for the same line of sight: lines of sight with a good measurement of the 3.4 μm feature are hardly observable in the UV, and the 3.4 μm feature is hardly detectable in lines of sight with a well–determined UV extinction curve. We could find only one case among the lines of sight with extinction curves given by Fitzpatrick and Massa (2007), namely HD 204827, in which the aliphatic C–H stretch was detected. Figure (4.3) shows the observations from Valencic et al. (2003), with superimposed the extinction spectrum predicted by our extinction model, fitted on the UV. Despite the very coarse sampling of the feature in the modelled extinction, dictated by the tabulated optical constants used in our work, model and observations are in acceptable agreement. To ease visual comparison, on the same figure we also show superimposed the 3.4 μm feature measured on a laboratory sample by Mennella (2010), which best matches the interstellar feature. Perusing our fitted extinction curves, we find that the ratio equivalent width on $\mathrm{A_V}$ of the modelled 3.4 μm feature goes from zero to $5.2 \cdot 10^{-4}$ μm mag^{-1}. If we use the laboratory profile to convert from equivalent width to maximum optical depth, this corresponds to $\tau_{\max} \simeq 4 \cdot 10^{-3} \mathrm{mag}^{-1} \mathrm{A_V}$, encompassing the average interstellar value of $\sim 3.6 \cdot 10^{-3} \mathrm{mag}^{-1} \mathrm{A_V}$ given by Gao et al. (2010).

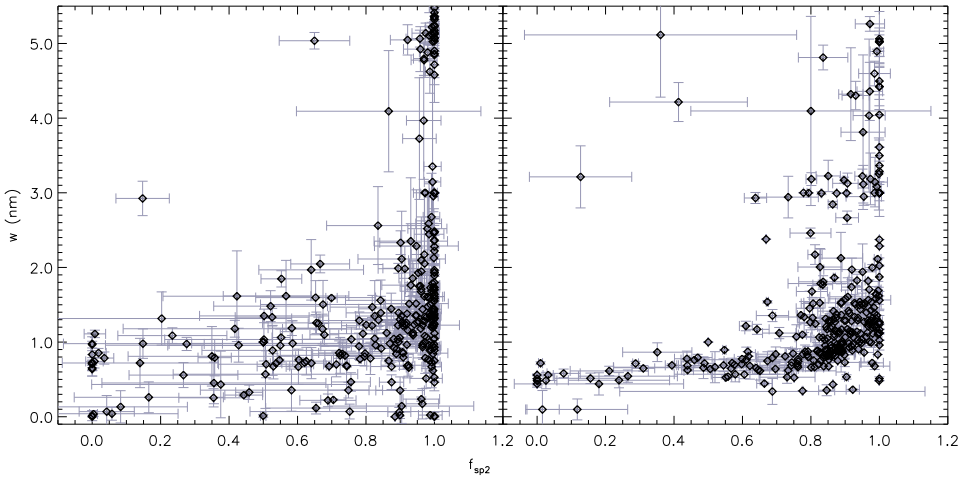

Figure 4.2: Observationally derived distribution of mantle thickness w and normalized sp^2 mantle carbon fraction, $\diamond$, with relative errors, for the simplified (left panel) and detailed (right panel) $[CM]^2$ models (see Chapter 3).

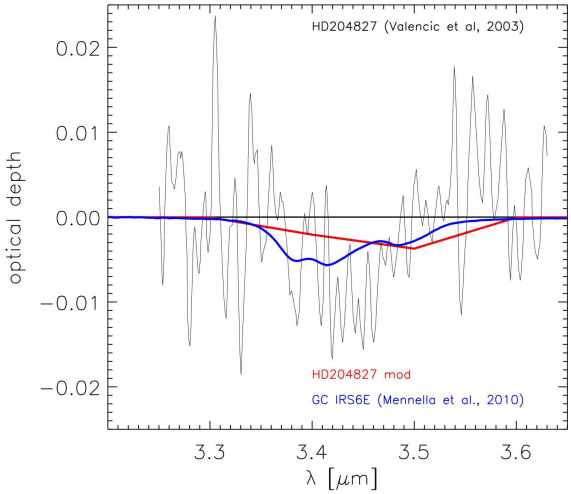

Figure 4.3: Optical depth of HD204827 (Valencic et al., 2003), with superimposed the extinction spectrum predicted by our extinction model (red line) and a laboratory spectrum (Mennella, 2010) known to provide an excellent fit to the band observed in GC IRS6E (Pendleton et al., 1994). The laboratory spectrum (blue line) was scaled to have the same integrated absorbance of the extinction model. The zero line is shown for easier comparison.

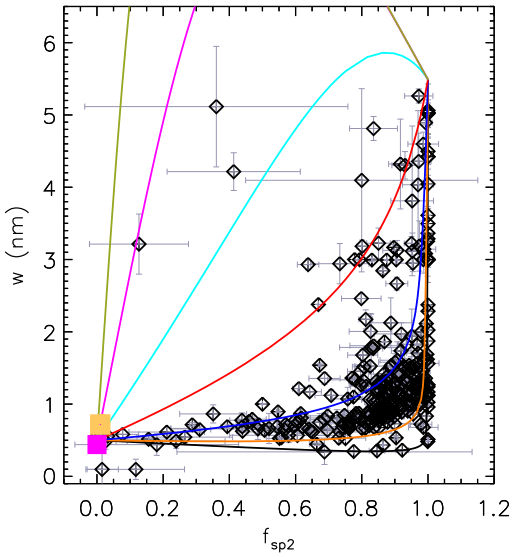

Figure 4.4: Comparison between observationally inferred ($\diamond$) and modelled $w - f_{sp^2}$ couples (solid lines). Evolutionary tracks start from the initial conditions $(f_{sp^2}, w) = (0, 0.5)$. Lines with different colors refer to different values of the rescaled photo–darkening rate (see figure 4.1). The magenta square is the line of sight towards HD62542, and the yellow the one towards HD204827.

4.4 Discussion

The observational results shown in the preceding sections have been obtained using a model consisting of a spherical void plus three concentric shells: silicate + hydrocarbon sp^2 + hydrocarbon sp^3. The relative fractions of these components and the thickness of the total carbon mantle are let to vary freely in response to the specifics of the fitting technique. The relative fractions of sp^2 and sp^3 bonding sites and the mantle thickness are also described by the evolutionary model summarised in system (4.4). Thus, it is possible to relate homologous, physically meaningful quantities derived from completely separate analyses. Such comparison is shown in figure (4.4), where we report the evolutionary tracks starting from the initial conditions $(f_{sp^2}, w) = (0, 0.5)$.

Data points obtained from the observations appear to follow rather closely the evolutionary tracks representing the evolution of carbonaceous mantles restarting from a thin leftover from a previous cycle, fully rehydrogenated. The vast majority of ISECs in figure (4.4) are neatly bracketed by evolutionary tracks within a small range of values of the $s_{\rm pd}$ parameter, which happens to cover exactly the typical values assumed for the prevailing conditions in the diffuse ISM. In particular, only two lines of sight appear to be unaccounted by the choice of the initial conditions $(f_{sp^2}, w) = (0, 0.5)$. This suggests that typical recycling times in the ISM should be shorter than carbon mantle lifetimes. Lines of sight observationally known to traverse recently shocked interstellar material (e.g., by an expanding SN shell) are expected to line up on the left side, i. e. carbonaceous mantles should be highly hydrogenated. This appears indeed to be the case for HD62542 (Cardelli et al., 1990) and HD204827 (Valencic et al., 2003, 2004), which are

shown in figure (4.4) by magenta and yellow squares, respectively. Interestingly, the 3.4 μm feature indicating a C–H rich grain mantle have been observed towards HD 204827 (Valencic et al., 2003). Both lines of sight have a steep UV rise, and a weak bump.

The parameters resulting from fitting ISECs with the detailed $[\mathrm{CM}]^2$ model therefore turn out to be strikingly consistent with our evolutionary picture. We can think of no conceivable reason for the fitting procedure in the Chapter (3) to produce such a distribution of points in the $w - f_{sp^2}$ plane as a random artefact, so we conclude it must be a real physical effect. Conversely, the simplified $[\mathrm{CM}]^2$ model shows a much weaker consistency with some kind of function relation between w and f_{sp^2}. This means that the observed pattern comes out only as a result of assuming the molecular component to absorb light as a collection of aromatic manifolds. If the $\pi^* \leftarrow \pi$ and $\sigma^* \leftarrow \sigma$ resonances are allowed to vary independently, this deconstructs the physical coherence of the extinction model with respect to the evolution of dust grain mantles. This is consistent with the recent findings of Li and Draine (2012) and Yang et al. (2013) that carbonaceous nanoparticles small enough to be stochastically heated to emit in the mid IR must be almost entirely aromatic, with at most a very small aliphatic component.

In the framework of our evolutionary model, given an observational point in the $w - f_{sp^2}$ plane, we can invert the evolutionary curve it lies on, to derive the corresponding s_{pd} and s_{ev}, the evolution parameter. We can thereafter build an histogram of the distribution of s_{ev} values, which is shown in figure (4.4). This was obtained using the data points from the detailed $[\mathrm{CM}]^2$ model and inverting the evolutionary curves restarting from $w = 0.5$ nm and $f_sp^2 = 0$, which were shown above to be most consistent with the assumed evolutionary model. This figure shows a broad maximum at $s_{\mathrm{ev}} \sim 10^9$ cm^{-3} K$^{1/2}$ y. Assuming typical interstellar values for density, $n_{\mathrm{H}} \sim 100\,\mathrm{cm}^{-3}$, and kinetic temperature, $T_k \sim 100\,\mathrm{K}$, we find that the observed evolutionary ages of carbonaceous mantles peak at times of about few millions years. The resulting photo–darkening time (corresponding to the maximum density of data points in figure 4.4) results $t_{\mathrm{pd}} \sim 0.3 - 1 \times 10^6/\chi$ y, in good agreement with the results of laboratory experiments on amorphous carbon (e.g., Iida et al. 1984, Mennella et al. 2001). We note that the timescales over which dust evolves in clouds are comparable to the probable ages of clouds themselves. For either shorter or longer timescales, the extinction should vary in a predictable way. Hence, through the study of interstellar extinction we may in principle be able to identify the evolutionary history of the diffuse clouds in the ISM.

Lastly, we relate R_V, the ratio of total-to-selective extinction, to the evolutionary stage of carbon dust, as traced by the ratio between the evolutionary and photo–darkening times $s_{\mathrm{ev}}/s_{\mathrm{pd}} = \chi t/t_{\mathrm{pd}}$ (figure 4.4). The plot evidences the existence of two, roughly distinct, regimes in which $s_{\mathrm{ev}}/s_{\mathrm{pd}} \leq 10$ and $s_{\mathrm{ev}}/s_{\mathrm{pd}} \geq 100$. In figure (4.4) we did not report those lines of sight with (scaled) photo–darkening time $s_{\mathrm{pd}} \leq 10^7/\chi$ cm^{-3} K$^{1/2}$ y (and thus their $s_{\mathrm{ev}}/s_{\mathrm{pd}}$ are larger than 100). For these lines (approximately 20 in number) the values of $f_{sp^2} \sim 1$, and thus a precise assignment of s_{pd} is prevented, only an upper limit can be given. This happens because of the asymptotic behaviour of the evolutionary tracks, which all tend to become very close to the $f_{sp^2} = 1$ line in the $w - f_{sp^2}$ plane (see figure 4.1).

In the region $s_{\mathrm{ev}}/s_{\mathrm{pd}} \leq 10$, where the most part of the lines of sight reside, the observationally derived R_V estimates tend to crowd about the fiducial value $R_V = 3$, when $t \approx t_{\mathrm{pd}}/\chi$. On the contrary, for evolutionary times much larger than t_{pd}/χ, R_V values are dispersed and erratic. The same occurs to the values of mantle thicknesses that are scattered, but generally larger than 1 nm. ISECs (in the light of the present

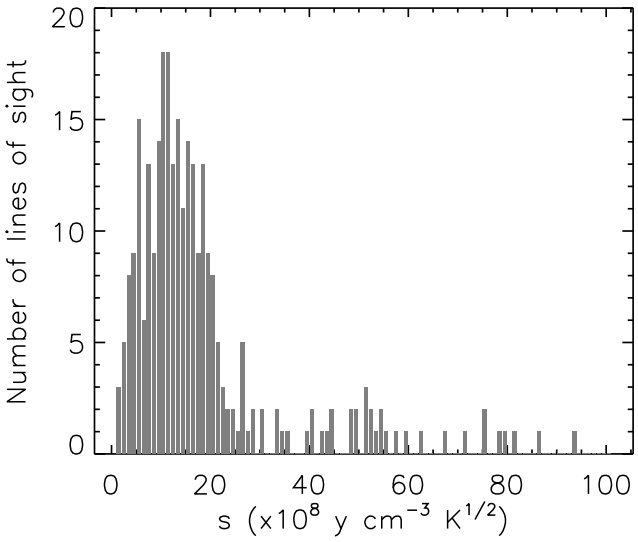

Figure 4.5: Distribution of the galactic ISECs from Fitzpatrick and Massa (2007) sample, as a function of the evolutionary indicator $s_{\rm ev}$.

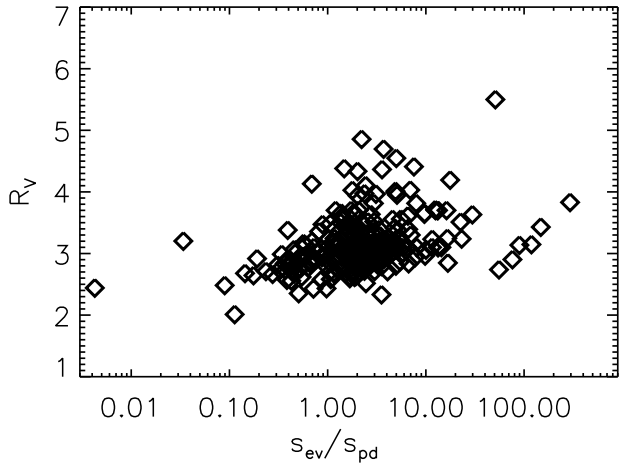

Figure 4.6: Relation between R_V and the carbon processing stage $s_{\rm ev}/s_{\rm pd}$.

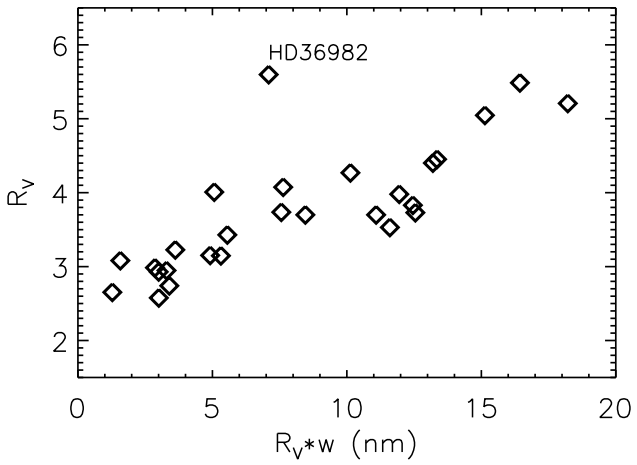

Figure 4.7: Relation between R_V and the carbon mantle thickness w for highly evolved ISECs, $s_{\rm ev}/s_{\rm pd} \geq 100$.

model) are time–dependent because of two factors: the gradual accumulation of carbon atoms on dust grains, and the photo–darkening of the resulting hydrocarbon mantle. As the mantle chemical composition reaches its final stage, the evolution of dust is driven by mantle accretion only, in which all grain sizes are modified simultaneously. Indeed, such a process appears to be imprinted in the ISECs for which $s_{\rm ev}/s_{\rm pd} \geq 100$ (figure 4.7): R_V and the mantle thickness w are well related with a moderate dispersion given by the effect of different size distributions. For such lines of sight, graphitisation is driven by UV photolysis, but even other mechanisms such as e.g., thermal annealing may contribute to increase of concentration of sp^2 bonding sites.

The line of sight HD36982 is the one showing the largest departures from a linear relation $w - R_V$. HD36982 is a sightline in which the relative amount of C and Si in grains is reduced compared to the galactic averaged value. Barbaro et al. (2004) selected a sample of 41 lines of sight (including HD36982) showing such a deficiency of metals incorporated in dust, 9 of which were part of the Fitzpatrick and Massa (2007) sample: 6 out 9 of these ISECs show a ratio $s_{\rm ev}/s_{\rm pd} \geq 100$, while for one (HD37061) such ratio is slightly larger than 10.

4.5 Conclusions and future works

With the results of this work exposed in the present and previous chapters we show the potentialities of our approach, but we did not fully exploit them here: multi dimensional correlations involving simultaneously several parameters and observed quantities will require appropriate multi–variate statistical analysis to be unravelled.

Such side analysis is not only of statistical nature. The remarkable agreement between observationally derived dust characteristics with their corresponding synthetic properties shed light on the nature of cosmic dust as described, despite the complex chemical structure, by a very limited number of regulatory parameters. Cardelli et al.

(1989) found that the shape of UV extinction curves correlates with the parameter $R_V = A_V/E(B-V)$, providing a link between one measure of dust grain environment and the wavelength dependence of the extinction. Thus, if the value of R_V can be determined from optical and IR photometry, then the properties of the entire UV – IR extinction curve can be predicted. However, while such a representation is very successful at describing ISECs as functions of few parameters, said parameters are not physically meaningful per se, but are complicated, largely unknown functions of the real physical quantities describing the interstellar material producing the extinction. The important question is how the variation of the extinction curve, and its topological uniformity, translates into the physical properties of dust grains. IR data suggest that the composition and the structure of carbonaceous dust vary within the ISM and that these variations involve changes in the relative abundance of sp^2 and sp^3 hybridised bonded components (e.g., Pendleton and Allamandola 2002, Chiar et al. 2013).

Similar variations are observed in laboratory samples of hydrogenated amorphous carbon (e.g., Duley and Hu 2012), due to changes in composition driven by factors such as hydrogen content, temperature, and UV photolysis. Such changes can be described through a photo–darkening time, a change of the absorption edge which corresponds to a decrease of the optical gap, in agreement with the general result that hydrogen favours the sp^3 carbon hybridisation and reduces the degree of aromatic sp^2 clusters in hydrogenated carbons (Robertson, 1991). The characterisation of dust extinction in terms of such chemical evolutionary factors is, of course, superposed to other, mainly dynamical, processes, such as grain size modulation in shocks. If the size distribution of grains were to be changed, then the extinction profile would also change. Still, the dispersion due to evolutionary regional factors is significant compared to that in the observational data (Cecchi-Pestellini et al., 2010).

In this chapter we put forward an evolutionary dust model, which was kept as simple as possible while still representing fairly accurately the processes described above, as they are expected to occur in the diffuse ISM. The only free parameters of this model are essentially the rescaled photo–darkening time and the initial conditions, leaving very little room to adjust the model to match observational data, as those obtained from the previous chapter. The distribution of observed ISECs in the $w - f_{sp^2}$ plane delineate a coherent evolutionary scenario for the galactic dust. One free parameter, $s_{\rm pd}$, determines the evolutionary track with rescaled time $s_{\rm ev}$ of carbonaceous dust mantles. Conversely, fitting any ISEC with the $[\mathrm{CM}]^2$ model observationally determines the mantle chemical composition and thickness. In general, the agreement is extremely convincing, enabling us to draw some conclusions on the life cycle and properties of interstellar dust. In the framework of the $[\mathrm{CM}]^2$ model, comparison of the observationally determined data with evolutionary tracks shows that

1. the establishment of a coherent evolutionary scenario for carbon dust requires a population of aromatic feature carriers;

2. most of the ISECs in the Fitzpatrick and Massa (2007) sample correspond to dust mantles that restarted growing after being almost completely removed, with the leftover fully rehydrogenated, by e.g., occasional shocks;

3. most ISECs are on tracks with $3\times10^8 < s_{\rm pd} < 10^9$ cm^{-3} K$^{1/2}$ y, where fluctuations (within a factor of 3) are induced by regional differences in the strength of the interstellar UV radiation field (gas density and temperature are incorporated in the evolutionary variable s);

4. the evolutionary "age" of ISECs peaks at times of few Myr, assuming typical diffuse interstellar conditions, comparable to the probable average age of diffuse clouds, on the basis of statistical considerations;

5. $R_V \sim 3$ is reached when $s_{\rm ev} \approx s_{\rm pd}$; this result suggests that, in average, most lines of sight are let free to "radiatively" evolve for $t \sim 0.3 - 1 \times 10^6 \, (100\,{\rm cm}^{-3}/n_{\rm H}) \, (100\,{\rm K}/T_{\rm k})^{1/2}$ y.

6. about 10% of lines of sight are associated to photo–darkening times shorter than the average galactic value, suggesting the presence of very strong UV fields, and other forms of $sp^3 \rightarrow sp^2$ annealing.

Although we did not address the topic in this chapter, the present results might have implications on the global histories of dust grains. During their lifetime, dust grains cycle through several diffuse/dense phases (e.g., Li and Greenberg 1997). Assuming a total lifetime for a dust grain to be approximately few hundreds of Myr (Serra Díaz-Cano and Jones, 2008), about the average age of a giant molecular cloud (Blitz and Williams, 1999), and considering the latter to undergo a number of dense phases of the order of ten (Sánchez D. and Parravano, 1999), each with a lifespan of few free fall times, we derive a dust residence time in each phase of a few tens of Myr. During a dense phase, dust grains are covered by an icy coating of volatiles, which protect the underlying carbon mantles, thereby "freezing" their chemical composition. Little refractory material is expected to form from icy mantles and remain attached to the mantle when the the ice evaporates. Before and during the subsequent diffuse regime (which is the only one in which the UV extinction can be currently measured), the emerging dust collections may be subjected to shocks or, to a minor extent, left relatively undisturbed. Thus, the observationally–inferred results shown in figure (4.2), may incorporate the imprinting of "long–lived" dust grains, sparsely populating the right portion of the diagram depicted in figure (4.4).

Variations in interstellar ISECs along different lines of sight in the MWG, and from one galaxy to another, are routinely interpreted as arising from changes in the relative abundances of the components that contribute to the extinction. In this work we show that these variations can be related to differences in the local physical conditions through an evolutionary process in the interstellar gas. Then ISECs could be a very useful tool in defining those physical conditions in the MWG or in other galaxies. A natural extension of this work will be its validation in environments markedly different from the ISM of the solar neighbourhood: physical situations in which the life cycle of the ISM is known to be very different either globally, e.g. much more frequent shocks in starburst galaxies, or locally, because of independent observational constraints on individual lines of sight. Indeed our aim is certainly to extend our analysis with the $[{\rm CM}]^2$ model to external galaxies starting from its closest neighbours, the MCs.

Since the UV extinction curve alone underconstrains some parameters, to improve the knowledge of dust grains would be useful to apply the $[{\rm CM}]^2$ model with further additional physics, or additional observational constraints (as the introduction in the fit of an increasing χ^2 penalty term for abundances increasingly exceeding observational constraints mentioned in the point 1 in the Section 3.6), or both, to shrink the parameter space, and the number of independent free parameters. The most obvious piece of complementary information would be to constrain the PAH mixture to simultaneously fit the extinction curve and the observed Aromatic Infrared Bands (AIBs) in emission for the same line of sight, for those few cases in which both are available. It has been

proven that the mid–IR AIB spectra can be fitted by mixtures of PAHs (Boersma et al., 2013), we here proved that PAH mixtures can fit any extinction curve, it remains to be proven whether the two observational features can be *simultaneously* fitted by *the same* PAH mixture for the same line of sight. This would also provide the most direct observational test for the need of a different population of particles contributing to the far–UV non–linear rise without contributing to the bump (see point 4 in the Section 3.6) or lack thereof.

We might also include some ionisation equilibrium condition for PAHs, instead of treating all ionisation states as independent parameters as we did in the chapter (3). This would obviously have a huge effect, adding only a handful of free parameters (at most electron density, kinetic temperature, UV radiation density) to remove $\sim$150. However, this would make physical sense *only* for lines of sight whose extinction is produced by relatively homogeneous interstellar material, which is not the common case. Observations of common tracers of interstellar material, e. g., the neutral sodium lines, almost always show a complicated structure of many intervening clouds with different radial velocities and velocity dispersions, hinting at different physical conditions among them. In such cases, trying to enforce a unique ionisation equilibrium for all PAHs along the line of sight would just be a meaningless exercise, which we hereby avoided. Again, we do plan to select a small subset of lines of sight which are observationally known to be dominated by a single, relatively homogeneous interstellar cloud (or a small number of well defined ones) and for them redo the fit with the detailed model, with the added constraint of ionisation equilibrium of PAHs (or a different one for each observed component).

Appendix A

The inverse problem

The problem of retrieving interstellar dust properties from an extinction curve falls within the general class of inverse problems that do not have a direct solution (such as to describe a dragon from its tracks, Bohren and R. 1983). In this Appendix, we briefly outline the formalism to handle non–linear inverse problems. Interested readers are referred for details to the exhaustive treatments of Twomey (1977) and Rodgers (2000).

The retrieval procedure is based on the fitting of the observational data with a suitable forward model. We deal with a number $\mathcal{L}$ of unknown quantities (e. g. void fraction, mantle thickness, $\cdots$) represented by a state vector $a \in \mathbb{R}^{\mathcal{L}}$ and a number $\mathcal{M}$ of data described by the vector $N_{\rm obs} \in \mathbb{R}^{\mathcal{M}}$, containing the extinction observed at different wave numbers. A forward model $F(n, a)$ describes the observations through a set of $\mathcal{N}$ fixed model parameters (the vector $n \in \mathbb{R}^{\mathcal{N}}$) and $\mathcal{L}$ adjustable parameters, providing a link between the observation vector and the state vector

$$N_{\rm obs} = F(n, a) + \epsilon \tag{A.1}$$

In the following we will omit n, since by definition it is a set of fixed model parameters. If one considers a small neighbourhood of some reference state vector a_0, the retrieval problem can be linearised, and equation (A.1) can be expressed as

$$R^i = \sum_l \left(\frac{\partial F^i}{\partial a^l} \right)_{\vec{a}_0} (a^l - a_0^l) + \epsilon^i \sim \sum_l K_l^i (a^l - a_0^l) \tag{A.2}$$

or more concisely, in matrix form

$$R = \mathbf{K}(a - a_0) + \epsilon \sim \mathbf{K}(a - a_0)$$

where $R = N_{\rm obs} - F(a_0)$ is the vector of the residuals with dimension $\mathcal{M}$. Its elements are equal to the difference between the observations and the corresponding simulation calculated using the reference state vector a_0. $\mathbf{K}$ is the Jacobian matrix of F with respect to the $\mathcal{L}$ adjustable parameters, having $\mathcal{M}$ rows and $\mathcal{L}$ columns. The goal of the retrieval operation is the determination of the difference vector $a - a_0$ in order to improve the previous estimate a_0. The problem relies on the construction of a solution matrix $\mathbf{G}$ (having $\mathcal{L}$ rows and $\mathcal{M}$ columns) that, applied to the vector $R = N_{\rm obs} - F(a_0)$, provides $a - a_0$. The retrieval procedure consists in the search of the parameters that produce the best simulation of the observations, by means of the minimisation of the

χ^2 merit function

$$\begin{aligned}\chi^2 &= \sum_{i,j}(V^{-1})_{ij}(N^i_{\rm obs}-F^i(a))(N^j_{\rm obs}-F^j(\vec{a}))\\ &\simeq \sum_{i,j}(V^{-1})_{ij}[R^i-\sum_l K^i_l(a^l-a^l_0)][R^j-\sum_l K^j_l(a^l-a^l_0)] \qquad \text{(A.3)}\end{aligned}$$

again, more concisely:

$$\begin{aligned}\chi^2 &= [N_{\rm obs}-F(a)]^T\mathbf{V}^{-1}[N_{\rm obs}-F(a)]\\ &\simeq [R-\mathbf{K}(a-a_0)]^T\mathbf{V}^{-1}[R-\mathbf{K}(a-a_0)]\end{aligned}$$

where the superscript T indicates the transpose and the weight $\mathbf{V}$ is a square matrix of dimension $\mathcal{M}$, the variance–covariance matrix (VCM) associated to the vector $N_{\rm obs}$ and hence R (Rodgers, 2000). When no further correction is to be applied to the state vector, $a-a_0$ becomes very nearly a null vector, and equation (A.3) reads as

$$\chi^2 = R^T\mathbf{V}^{-1}R \qquad \text{(A.4)}$$

In general the observations do not depend linearly on the unknown parameters a. As a consequence equation (A.4) is not a quadratic function of the unknowns. However, for a sufficiently close to a reference vector a_0 we may assume that the χ^2 function is well approximated by its Taylor expansion in a_0, truncated at second order, namely

$$\begin{aligned}\chi^2(a) &= \chi^2(a_0)+\sum_l\left(\frac{\partial\chi^2}{\partial a^l}\right)_{a_0}(a^l-a^l_0)+\frac{1}{2}\sum_{l,m}\left(\frac{\partial^2\chi^2}{\partial a^l\partial a^m}\right)_{a_0}(a^l-a^l_0)(a^m-a^m_0)\\ &= \chi^2(a_0)+(\nabla\chi^2)^T_{a_0}(a-a_0)+\frac{1}{2}(a-a_0)^T(\nabla^2\chi^2)_{a_0}(a-a_0) \qquad \text{(A.5)}\end{aligned}$$

where ∇ and ∇^2 indicate the gradient and the Hessian matrix, respectively. Writing the gradient and the Hessian matrices of $F(n,a)$ explicitly, we obtain

$$\begin{aligned}\chi^2(a) &= \chi^2(a_0)-2\sum_{i,j,l}(V^{-1})_{ij}\left(\frac{\partial F^i}{\partial a^l}\right)_{a_0}(N^j_{\rm obs}-F^j(a_0))(a^l-a^l_0)\\ &\quad+\sum_{i,j,l,m}(V^{-1})_{ij}\left[\left(\frac{\partial F^i}{\partial a^l}\right)_{a_0}\left(\frac{\partial F^j}{\partial a^m}\right)_{a_0}-\left(\frac{\partial^2 F^i}{\partial a^l\partial a^m}\right)_{a_0}(N^j_{\rm obs}-F^j(a_0))\right](a^l-a^l_0)(a^m-a^m_0)\\ &= \chi^2(a_0)-2\sum_{i,j,l}(V^{-1})_{ij}K^i_lR^j(a^l-a^l_0)\\ &\quad+\sum_{i,j,l,m}(V^{-1})_{ij}\left[K^i_lK^j_m-H^i_{lm}R^j\right](a^l-a^l_0)(a^m-a^m_0)\\ &= \chi^2(a_0)-2\left(\mathbf{K}^T\mathbf{V}^{-1}R\right)^T(a-a_0)+(a-a_0)^T\mathbf{K}^T\mathbf{V}^{-1}\mathbf{K}(a-a_0)\\ &\quad-\sum_{i,j,l,m}(V^{-1})_{ij}H^i_{lm}R^j(a^l-a^l_0)(a^m-a^m_0) \qquad \text{(A.6)}\end{aligned}$$

Neglecting the term with the second derivatives of $F(a)$, i. e. H^i_{lm}, in eq.(A.6), the value of $a-a_0$ that minimizes the χ^2 function is the Gauss–Newton solution (e. g., Gill et al. 1981)

$$a = a_0+\mathbf{A}^{-1}\mathbf{K}^T\mathbf{V}^{-1}R \qquad \text{(A.7)}$$

where $\mathbf{A} = \mathbf{K}^T\mathbf{V}^{-1}\mathbf{K}$. The solution matrix of the inverse problem is thus

$$\mathbf{G} = \mathbf{A}^{-1}\mathbf{K}^T\mathbf{V}^{-1} \tag{A.8}$$

The improved estimate, equation (A.7), can be used as a new assumed state vector for a further iteration of the retrieval process. The iteration is successful, i. e. $\chi^2(a) < \chi^2(a_0)$, only if non–linearities are not too large (hence justifying the neglect of the second derivative term above).

The Levemberg–Marquardt method introduces a modification to the iterative procedure outlined above, by substituting the matrix $\mathbf{A}$ with a matrix $\hat{\mathbf{A}}$ defined according to the following rule

$$\begin{aligned} \hat{\mathbf{A}}_{ij} &= \mathbf{K}^T\mathbf{V}^{-1}\mathbf{K} \qquad \text{for } i \neq j \\ \hat{\mathbf{A}}_{ij} &= \mathbf{K}^T\mathbf{V}^{-1}\mathbf{K}(1+\lambda) \quad \text{for } i = j \end{aligned} \tag{A.9}$$

where λ is a damping parameter that increases the value of the diagonal elements. The modification enables a faster convergence and is recommended in the case of strongly non–linear problems. The factor λ is initialized to a user–defined value, and, during the retrieval iterations, it is increased or decreased depending on whether the χ^2 function increases or decreases. For very small values of λ, $\hat{\mathbf{A}} \simeq \mathbf{A}$, hence going back to the simple linearised method outlined above; for large λ values, conversely, successive iterations go in the direction of the steepest descent of χ^2, with smaller and smaller steps for larger and larger λ. While $\hat{\mathbf{A}}$ is guaranteed to be nonsingular, it may be very nearly singular, if the residual changes very little in some direction of a space. In that case, $\mathbf{G}$ becomes numerically unstable, and tends to produce unrealistic (extremely large) shifts in those directions of a, thereby producing unphysical solutions. To overcome this problem, we use the Singular Value Decomposition to invert $\hat{\mathbf{A}}$, and set to zero all "singular" values which are too low, which are exactly those directions in which the residual is almost constant. This stabilises the procedure.

In the case of diagonal VCM, $(\mathbf{V}^{-1})_{ij} = \sigma_i^{-1}\delta_{ij}$, the χ^2 prescription becomes

$$\chi^2(a) = \sum_i \left(\frac{N^i_{\text{obs}} - F^i(a)}{\sigma_i} \right)^2 \tag{A.10}$$

where σ_i is the variance of the i-th data point. In this case, $\mathbf{V_a} = \alpha^{-1}$ with $\alpha_{ij} = 1/2\,\partial^2\chi^2/\partial a_i \partial a_j$ (e. g., Press et al. 1992).

Appendix B

Analytic approximations

The equation coefficients in system (4.4) are weakly dependent on time, through the quantities $\langle \sigma_d n_d \rangle / [\mathrm{H}]$, derived integrating over the dust size distribution, as this changes in time during mantle accretion, and the mantle density δ_{C}. Setting both quantities to constant values we obtain the approximate analytic solutions corresponding to initially bare silicate cores

$$\begin{cases} x_{\mathrm{C}}(s) = \exp\left(-\hat{A} \times s\right) \\ x_{sp^3}(s) = \dfrac{\hat{A}}{\left(s_{\mathrm{pd}}^{-1} - \hat{A}\right)} \times \left[x_{\mathrm{C}}(s) - \exp(-s_{\mathrm{pd}}^{-1} \times s)\right] \\ w = \dfrac{\hat{D}}{\hat{A}\delta_{\mathrm{C}}} \left[1 - x_{\mathrm{C}}(s)\right] \end{cases} \tag{B.1}$$

For $s \to \infty$ equations (B.1) give $x_{\mathrm{C}} \to 0$, $x_{sp^3} \to 0$, $x_{sp^2} \to 1$, and $w \to \hat{D}/(\hat{A}\delta_{\mathrm{C}})$. Finally, when $s_{\mathrm{pd}} \to \infty$, $x_{sp^2} \to 0$ and $x_{sp^3} \sim 1 - x_{\mathrm{C}}$. Curves (B.1) with $s = \text{const.}$ are straight lines parallel to the $x_{sp^2}-$axis. Such simple behaviour is not shared by exact numerical solutions, i. e. iso–s curves are not straight lines when the analytical approximation ceases to be valid (see figure 4.1).

Bibliography

Ábrahám, P., Juhász, A., Dullemond, C. P., Kóspál, Á., van Boekel, R., Bouwman, J., Henning, T., Moór, A., Mosoni, L., Sicilia-Aguilar, A., and Sipos, N. (2009). Episodic formation of cometary material in the outburst of a young Sun-like star. *Nature*, 459:224–226.

Allamandola, L. J., Tielens, A. G. G. M., and Barker, J. R. (1985). Polycyclic aromatic hydrocarbons and the unidentified infrared emission bands - Auto exhaust along the Milky Way. *ApJ*, 290:L25–L28.

Allamandola, L. J., Tielens, A. G. G. M., and Barker, J. R. (1989). Interstellar polycyclic aromatic hydrocarbons - The infrared emission bands, the excitation/emission mechanism, and the astrophysical implications. *The Astrophysical Journal Supplement Series*, 71:733–775.

Anders, E. and Grevesse, N. (1989). Abundances of the elements - Meteoritic and solar. *Geochim. Cosmochim. Acta*, 53:197–214.

Asano, R. S., Takeuchi, T. T., Hirashita, H., and Inoue, A. K. (2013). Dust formation history of galaxies: A critical role of metallicity for the dust mass growth by accreting materials in the interstellar medium. *Earth, Planets, and Space*, 65:213–222.

Ashok, N. H., Varaprasad, P. L. H., and Birch, J. R. (1991). Polyethylene $(C_2H_4)_N$. In Academic Press, Boston, editor, *Handbook of Optical Constants of Solids.*, volume 2, page 957.

Asplund, M., Grevesse, N., Sauval, A. J., and Scott, P. (2009). The Chemical Composition of the Sun. *ARA&A*, 47:481–522.

Barbaro, G., Geminale, A., Mazzei, P., and Congiu, E. (2004). Anomalous dust-to-gas ratios in the Galaxy. *MNRAS*, 353:760–768.

Bernard, J. P., Reach, W. T., Paradis, D., and al. (2008). Spitzer Survey of the Large Magellanic Cloud, Surveying the Agents of a Galaxy's Evolution (sage). IV. Dust Properties in the Interstellar Medium. *AJ*, 136:919–945.

Berné, O., Joblin, C., Deville, Y., Smith, J. D., Rapacioli, M., Bernard, J. P., Thomas, J., Reach, W., and Abergel, A. (2007). Analysis of the emission of very small dust particles from Spitzer spectro-imagery data using blind signal separation methods. *A & A*, 469:575–586.

Bianchi, L., Clayton, G. C., Bohlin, R. C., Hutchings, J. B., and Massey, P. (1996). Ultraviolet Extinction by Interstellar Dust in External Galaxies: M31. *ApJ*, 471:203.

Blair, W. P. and Kirshner, R. P. (1985). Improved optical spectrophotometry of supernova remnants in M33. *ApJ*, 289:582–597.

Blitz, L. and Williams, J. P. (1999). Molecular Clouds. In Lada, C. J. and Kylafis, N. D., editors, *NATO ASIC Proc. 540: The Origin of Stars and Planetary Systems*, page 3.

Boersma, C., Allamandola, L. J., Bauschlicher, C., Ricca, A., Mattioda, A., Cami, J., Peeters, E., Sanchez, F., Puerta, G., and Hudgins, D. M. (2013). The NASA Ames PAH IR Spectroscopic Database V 2.0 - Spectroscopic Fitting Tools and More. In *American Astronomical Society Meeting Abstracts*, volume 221 of *American Astronomical Society Meeting Abstracts*, page 440.09.

Bohren, C. F. and R., H. D. (1983). *Absorption and Scattering of Light by Small Particles*. New York: Wiley.

Borghese, F., Denti, P., Sajia, R., Toscano, G., and Sindoni, O. I. (1987). Extinction coefficients for a random dispersion of small stratified spheres and a random dispersion of their binary aggregates. *J. Opt. Soc. Am. A*, 4:1984.

Bouchet, P., Lequeux, J., Maurice, E., Prevot, L., and Prevot-Burnichon, M. L. (1985). The visible and infrared extinction law and the gas-to-dust ratio in the Small Magellanic Cloud. *A&A*, 149:330–336.

Bradley, J. P., Keller, L. P., Snow, T. P., Hanner, M. S., Flynn, G. J., Gezo, J. C., Clemett, S. J., Brownlee, D. E., and Bowey, J. E. (1999). An infrared spectral match between GEMS and interstellar grains. *Science*, 285:1716–1718.

Byleveld, S. E., Melrose, D. B., and Cram, L. E. (1993). Coulomb Interactions Between Cosmic-Rays and Charged Dust Grains. *Proceedings of the Astronomical Society of Australia*, 10:218.

Calzetti, D. (2001). The Dust Opacity of Star-forming Galaxies. *The Publications of the Astronomical Society of the Pacific*, 113:1449–1485.

Calzetti, D., Bohlin, R. C., Kinney, A. L., Storchi-Bergmann, T., and Heckman, T. M. (1995). The heating of dust in starburst galaxies: The contribution of the nonionizing radiation. *ApJ*, 443:136–151.

Cardelli, J. A., Clayton, G. C., and Mathis, J. S. (1989). The relationship between infrared, optical, and ultraviolet extinction. *ApJ*, 345:245–256.

Cardelli, J. A., Edgar, R. J., Savage, B. D., and Suntzeff, N. B. (1990). Molecules toward HD 62542 - A high-density, peculiar extinction sight line in the GUM nebula complex. *ApJ*, 362:551–562.

Cartledge, S. I. B., Clayton, G. C., Gordon, K. D., Rachford, B. L., Draine, B. T., Martin, P. G., Mathis, J. S., Misselt, K. A., Sofia, U. J., Whittet, D. C. B., and Wolff, M. J. (2005). FUSE Measurements of Far-Ultraviolet Extinction. II. Magellanic Cloud Sight Lines. *ApJ*, 630:355–367.

Cartledge, S. I. B., Lauroesch, J. T., Meyer, D. M., and Sofia, U. J. (2004). The Homogeneity of Interstellar Oxygen in the Galactic Disk. *ApJ*, 613:1037–1048.

Cartledge, S. I. B., Lauroesch, J. T., Meyer, D. M., and Sofia, U. J. (2006). The Homogeneity of Interstellar Elemental Abundances in the Galactic Disk. *ApJ*, 641:327–346.

Casu, S., Cecchi-Pestellini, C., and Aiello, S. (2001). Dust-induced chemical differentiation in dense regions. *MNRAS*, 325:826–834.

Cecchi-Pestellini, C., Cacciola, A., Iatì, M. A., Saija, R., Borghese, F., Denti, P., Giusto, A., and Williams, D. A. (2010). Stratified dust grains in the interstellar medium - II. Time-dependent interstellar extinction. *MNRAS*, 408:535–541.

Cecchi-Pestellini, C., Malloci, G., Mulas, G., Joblin, C., and Williams, D. A. (2008). The role of the charge state of PAHs in ultraviolet extinction. *A & A*, 486:L25–L29.

Cecchi-Pestellini, C. and Williams, D. A. (1998). Evolving interstellar extinction. *MNRAS*, 296:414–418.

Cesarsky, D., Lequeux, J., Ryter, C., and Gérin, M. (2000). ISO observations of the reflection nebula Ced 201: evolution of carbonaceous dust. *A & A*, 354:L87–L91.

Chen, S. L., Li, A., and Wei, D. M. (2006). Dust Extinction of Gamma-Ray Burst Host Galaxies: Identification of Two Classes? *ApJ*, 647:L13–L16.

Chiar, J. E., Tielens, A. G. G. M., Adamson, A. J., and Ricca, A. (2013). The Structure, Origin, and Evolution of Interstellar Hydrocarbon Grains. *ApJ*, 770:78.

Chokshi, A., Tielens, A. G. G. M., and Hollenbach, D. (1993). Dust coagulation. *ApJ*, 407:806–819.

Clayton, G. C., Gordon, K. D., Salama, F., Allamandola, L. J., Martin, P. G., Snow, T. P., Whittet, D. C. B., Witt, A. N., and Wolff, M. J. (2003). The Role of Polycyclic Aromatic Hydrocarbons in Ultraviolet Extinction. I. Probing Small Molecular Polycyclic Aromatic Hydrocarbons. *ApJ*, 592:947–952.

de Vaucouleurs, G. and Buta, R. (1983). The galactic extinction of extragalactic objects. I - The csc B law and the extinction coefficient. *AJ*, 88:939–961.

Desert, F. X., Boulanger, F., Leger, A., Puget, J. L., and Sellgren, K. (1986). Nature of very small grains - PAH molecules or silicates? *A & A*, 159:328–330.

Dominik, C. and Tielens, A. G. G. M. (1997). The Physics of Dust Coagulation and the Structure of Dust Aggregates in Space. *ApJ*, 480:647.

Draine, B. T. (1985). Tabulated optical properties of graphite and silicate grains. *ApJS*, 57:587–594.

Draine, B. T. (1988). The discrete-dipole approximation and its application to interstellar graphite grains. *ApJ*, 333:848–872.

Draine, B. T. (1990). Evolution of interstellar dust. In Blitz, L., editor, *The Evolution of the Interstellar Medium*, volume 12 of *Astronomical Society of the Pacific Conference Series*, pages 193–205.

Draine, B. T. (2003). Interstellar Dust Grains. *Annu. Rev. Astron. Astrophys.*, 41:241–289.

Draine, B. T. and Fraisse, A. A. (2009). Polarized Far-Infrared and Submillimeter Emission from Interstellar Dust. *ApJ*, 696:1–11.

Draine, B. T. and Lazarian, A. (1998). Diffuse Galactic Emission from Spinning Dust Grains. *ApJ*, 494:L19.

Draine, B. T. and Lee, H. M. (1984). Optical properties of interstellar graphite and silicate grains. *ApJ*, 285:89–108.

Draine, B. T. and Li, A. (2007). Infrared Emission from Interstellar Dust. IV. The Silicate-Graphite-PAH Model in the Post-Spitzer Era. *ApJ*, 657:810–837.

Draine, B. T. and Salpeter, E. E. (1979a). Destruction mechanisms for interstellar dust. *ApJ*, 231:438–455.

Draine, B. T. and Salpeter, E. E. (1979b). On the physics of dust grains in hot gas. *ApJ*, 231:77–94.

Draine, B. T. and Tan, J. C. (2003). The Scattered X-Ray Halo around Nova Cygni 1992: Testing a Model for Interstellar Dust. *ApJ*, 594:347–362.

Duley, W. W. (2006a). A Plasmon Resonance in Dehydrogenated Coronene ($C_{24}H_x$) and Its Cations and the Origin of the Interstellar Extinction Band at 217.5 Nanometers. *ApJ*, 639:L59–L62.

Duley, W. W. (2006b). Dehydrogenated Cations of Coronene, $C_{24}H^+{}_x$: The Source of Many Diffuse Interstellar Bands. *ApJ*, 643:L21–L24.

Duley, W. W. and Hu, A. (2012). The 217.5 nm Band, Infrared Absorption, and Infrared Emission Features in Hydrogenated Amorphous Carbon Nanoparticles. *ApJ*, 761:115.

Duley, W. W. and Williams, D. A. (1993). The formation of H2 on interstellar dust. *MNRAS*, 260:37–42.

Duley, W. W. and Williams, D. A. (2011). Excitation of the Aromatic Infrared Emission Bands: Chemical Energy in Hydrogenated Amorphous Carbon Particles? *ApJ*, 737:L44.

Dwek, E. (1998). The Evolution of the Elemental Abundances in the Gas and Dust Phases of the Galaxy. *ApJ*, 501:643.

Dwek, E. (2001). The Role of Dust in Producing the Cosmic Infrared Background. *ArXiv Astrophysics e-prints*.

Edvardsson, B., Andersen, J., Gustafsson, B., Lambert, D. L., Nissen, P. E., and Tomkin, J. (1993). The Chemical Evolution of the Galactic Disk - Part One - Analysis and Results. *A & A*, 275:101.

Fitzpatrick, E. L. (1986). An average interstellar extinction curve for the Large Magellanic Cloud. *AJ*, 92:1068–1073.

Fitzpatrick, E. L. (2004). Interstellar Extinction in the Milky Way Galaxy. In Witt, A. N., Clayton, G. C., and Draine, B. T., editors, *Astrophysics of Dust*, volume 309 of *Astronomical Society of the Pacific Conference Series*, page 33.

Fitzpatrick, E. L. and Massa, D. (2007). An Analysis of the Shapes of Interstellar Extinction Curves. V. The IR-through-UV Curve Morphology. *ApJ*, 663:320–341.

Fitzpatrick, E. L. and Massa, D. (2009). An Analysis of the Shapes of Interstellar Extinction Curves. VI. The Near-IR Extinction Law. *ApJ*, 699:1209–1222.

Fruchter, A., Krolik, J. H., and Rhoads, J. E. (2001). X-Ray Destruction of Dust along the Line of Sight to γ-Ray Bursts. *ApJ*, 563:597–610.

Furton, D. G. and Witt, A. N. (1993). Activation of extended red emission photoluminescence in carbon solids by exposure to atomic hydrogen and UV radiation. *ApJ*, 415:L51–L54.

Gall, C., Hjorth, J., and Andersen, A. C. (2011). Production of dust by massive stars at high redshift. *A & A Review*, 19:43.

Gao, J., Jiang, B. W., and Li, A. (2010). Toward understanding the 3.4 μm and 9.7 μm extinction feature variations from the local diffuse interstellar medium to the Galactic center. *Earth, Planets, and Space*, 62:63–67.

Gill, P. E., Murray, W., and Wright, M. H. (1981). *Practical Optimization*. San Diego, CA: Academic.

Goebel, J. H. (1983). Observation of ice mantles toward HD 29647. *ApJ*, 268:L41–L45.

Gordon, K. D., Calzetti, D., and Witt, A. N. (1997). Dust in Starburst Galaxies. *ApJ*, 487:625.

Gredel, R., van Dishoeck, E. F., and Black, J. H. (1993). The abundance of CH(+) in translucent molecular clouds - Further tests of shock models. *A & A*, 269:477–495.

Greenberg, J. M. (1973). Chemical and Physical Properties of Interstellar Dust. In Gordon, M. A. and Snyder, L. E., editors, *Molecules in the Galactic Environment*, page 93.

Greenberg, J. M. (1974). The Interstellar Depletion Mystery, or where have all those Atoms Gone? *ApJ*, 189:L81.

Greenberg, J. M. (1984). The structure and evolution of interstellar grains. *Scientific American*, 250:124–133.

Greenberg, J. M. and Hong, S.-S. (1974). The chemical composition and distribution of interstellar grains. In Kerr, F. J. and Simonson, S. C., editors, *Galactic Radio Astronomy*, volume 60 of *IAU Symposium*, pages 155–177.

Greenberg, J. M. and Hong, S. S. (1976). Cosmic abundances and interstellar grains, or where have all those atoms gone? *News Letter of the Astronomical Society of New York*, 1:78.

Greenberg, J. M. and Shen, C. (1999). Cosmic Dust in the 21st Century. *Astrophysics Space Science*, 269:33–55.

Greif, T. H. and Bromm, V. (2006). Two populations of metal-free stars in the early Universe. *MNRAS*, 373:128–138.

Grevesse, N., Sauval, A. J., and Blomme, R. (1994). Solar Abundances of C; N; O. In Rabin, D. M., Jefferies, J. T., and Lindsey, C., editors, *Infrared Solar Physics*, volume 154 of *IAU Symposium*, page 539.

Gudennavar, S. B., Bubbly, S. G., Preethi, K., and Murthy, J. (2012). A Compilation of Interstellar Column Densities. *ApJS*, 199:8.

Guhathakurta, P. and Draine, B. T. (1989). Temperature fluctuations in interstellar grains. I - Computational method and sublimation of small grains. *ApJ*, 345:230–244.

Hecht, J. H. (1986). A physical model for the 2175 A interstellar extinction feature. *ApJ*, 305:817–822.

Hempel, M. and Holweger, H. (2003). Abundance analysis of late B stars. Evidence for diffusion and against weak stellar winds. *A & A*, 408:1065–1076.

Hopkins, P. F., Strauss, M. A., Hall, P. B., Richards, G. T., Cooper, A. S., Schneider, D. P., Vanden Berk, D. E., Jester, S., Brinkmann, J., and Szokoly, G. P. (2004). Dust Reddening in Sloan Digital Sky Survey Quasars. *AJ*, 128:1112–1123.

Iatì, M. A., Cecchi-Pestellini, C., Cacciola, A., Saija, R., Denti, P., and Borghese, F. (2011). Stratified dust grains in the interstellar medium. III: Infrared cross-sections. *JQSRT*, 112:1898.

Iatì, M. A., Cecchi-Pestellini, C., Williams, D. A., Borghese, F., Denti, P., Saija, R., and Aiello, S. (2001). Porous interstellar grains. *MNRAS*, 322:749–756.

Iatì, M. A., Saija, R., Borghese, F., Denti, P., Cecchi-Pestellini, C., and Williams, D. A. (2008). Stratified dust grains in the interstellar medium - I. An accurate computational method for calculating their optical properties. *MNRAS*, 384:591–598.

Iida, S., Ohtaki, T., and Seki, T. (1984). Photodarkening and photobleaching in a-C:H films. volume 120 of *AIP Conference Proceedings*, page 258.

Islam, F., Cecchi-Pestellini, C., Viti, S., and Casu, S. (2010). Formation Pumping of Molecular Hydrogen in Dark Clouds. *ApJ*, 725:1111–1123.

Jackson, J. D. (1975). *Classical electrodynamics*. John Wiley & Sons, New York.

Jenkins, E. B. (2009). A Unified Representation of Gas-Phase Element Depletions in the Interstellar Medium. *ApJ*, 700:1299–1348.

Jiang, L., Fan, X., Hines, D. C., and al. (2006). Probing the Evolution of Infrared Properties of z ˜ 6 Quasars: Spitzer Observations. *AJ*, 132:2127–2134.

Joblin, C., Leger, A., and Martin, P. (1992). Contribution of polycyclic aromatic hydrocarbon molecules to the interstellar extinction curve. *ApJ*, 393:L79–L82.

Jones, A. (2009). The role of dust in the interstellar medium: dust sources and dust evolution. In Pagani, L. and Gerin, M., editors, *EAS Publications Series*, volume 34 of *EAS Publications Series*, pages 107–118.

Jones, A. and Tielens, A. (1994). Interstellar dust : physical processes. In Montmerle, T., Lada, C. J., Mirabel, I. F., and Tran Thanh Van, J., editors, *The Cold Universe*, page 35.

Jones, A. P. (2004). Dust Destruction Processes. In Witt, A. N., Clayton, G. C., and Draine, B. T., editors, *Astrophysics of Dust*, volume 309 of *Astronomical Society of the Pacific Conference Series*, page 347.

Jones, A. P. (2012a). Variations on a theme - the evolution of hydrocarbon solids. I. Compositional and spectral modelling - the eRCN and DG models. *A & A*, 540:A1.

Jones, A. P. (2012b). Variations on a theme - the evolution of hydrocarbon solids. II. Optical property modelling - the optEC$_{(s)}$ model. *A & A*, 540:A2.

Jones, A. P., Duley, W. W., and Williams, D. A. (1990). The structure and evolution of hydrogenated amorphous carbon grains and mantles in the interstellar medium. *QJRAS*, 31:567–582.

Jones, A. P., Fanciullo, L., Köhler, M., Verstraete, L., Guillet, V., Bocchio, M., and Ysard, N. (2013). The evolution of amorphous hydrocarbons in the ISM: dust modelling from a new vantage point. *A & A*, 558:A62.

Jones, A. P., Tielens, A. G. G. M., and Hollenbach, D. J. (1996). Grain Shattering in Shocks: The Interstellar Grain Size Distribution. *ApJ*, 469:740.

Jones, A. P., Tielens, A. G. G. M., Hollenbach, D. J., and McKee, C. F. (1994). Grain destruction in shocks in the interstellar medium. *ApJ*, 433:797–810.

Kennicutt, Jr., R. C., Bresolin, F., Bomans, D. J., Bothun, G. D., and Thompson, I. B. (1995). Large scale structure of the ionized gas in the magellanic clouds. *AJ*, 109:594–604.

Krełowski, J. and Strobel, A. (2012). Limited diversity of the interstellar extinction law. *Astronomische Nachrichten*, 333:60–70.

Landstrass, M. I. and Ravi, K. V. (1989). Resistivity of chemical vapor deposited diamond films. *Appl. Phys. Lett.*, 55.

Laor, A. and Draine, B. T. (1993). Spectroscopic constraints on the properties of dust in active galactic nuclei. *ApJ*, 402:441–468.

Leger, A. and Puget, J. L. (1984). Identification of the 'unidentified' IR emission features of interstellar dust? *A & A*, 137:L5–L8.

Li, A. (2009). Astrophysics: Cosmic crystals caught in the act. *Nature*, 459:173–176.

Li, A. and Draine, B. T. (2001a). Infrared Emission from Interstellar Dust. II. The Diffuse Interstellar Medium. *ApJ*, 554:778–802.

Li, A. and Draine, B. T. (2001b). On Ultrasmall Silicate Grains in the Diffuse Interstellar Medium. *ApJ*, 550:L213–L217.

Li, A. and Draine, B. T. (2002). Are Silicon Nanoparticles an Interstellar Dust Component? *ApJ*, 564:803–812.

Li, A. and Draine, B. T. (2012). The Carriers of the Interstellar Unidentified Infrared Emission Features: Aromatic or Aliphatic? *ApJ*, 760:L35.

Li, A. and Greenberg, J. M. (1997). A unified model of interstellar dust. *A & A*, 323:566–584.

Liszt, H. S., Pety, J., and Lucas, R. (2008). Limits on chemical complexity in diffuse clouds: search for CH{3} and HC{5}N absorption. *A & A*, 486:493–496.

Maiolino, R., Schneider, R., Oliva, E., Bianchi, S., Ferrara, A., Mannucci, F., Pedani, M., and Roca Sogorb, M. (2004). A supernova origin for dust in a high-redshift quasar. *Nature*, 431:533–535.

Maíz Apellániz, J. and Rubio, M. (2012). Ultraviolet extinction toward a quiescent molecular cloud in the Small Magellanic Cloud. *A & A*, 541:A54.

Malloci, G., Joblin, C., and Mulas, G. (2007). On-line database of the spectral properties of polycyclic aromatic hydrocarbons. *Chemical Physics*, 332:353–359.

Malloci, G., Mulas, G., Cecchi-Pestellini, C., and Joblin, C. (2008). Dehydrogenated polycyclic aromatic hydrocarbons and UV bump. *A & A*, 489:1183–1187.

Malloci, G., Mulas, G., and Joblin, C. (2004). Electronic absorption spectra of PAHs up to vacuum UV. Towards a detailed model of interstellar PAH photophysics. *A & A*, 426:105–117.

Martinazzo, R. and Tantardini, G. F. (2006). Quantum study of Eley-Rideal reaction and collision induced desorption of hydrogen atoms on a graphite surface. II. H-physisorbed case . *J. Chem. Phys.*, 124:124703.

Mathis, J. S. (1995). Temperature Fluctuations in Nebulae (Invited paper). In Pena, M. and Kurtz, S., editors, *Revista Mexicana de Astronomia y Astrofisica Conference Series*, volume 3 of *Revista Mexicana de Astronomia y Astrofisica, vol. 27*, page 207.

Mathis, J. S. (1996). Dust Models with Tight Abundance Constraints. *ApJ*, 472:643.

Mathis, J. S. (2000). Properties of interstellar dust. *J. Geophys. Res.*, 105:10269–10278.

Mathis, J. S., Rumpl, W., and Nordsieck, K. H. (1977). The size distribution of interstellar grains. *ApJ*, 217:425–433.

Matsuura, M., Dwek, E., Meixner, M., and al. (2011). Herschel Detects a Massive Dust Reservoir in Supernova 1987A. *Science*, 333:1258–.

McKee, C. (1989). Dust Destruction in the Interstellar Medium. In Allamandola, L. J. and Tielens, A. G. G. M., editors, *Interstellar Dust*, volume 135 of *IAU Symposium*, page 431.

McKee, C. F. (2011). Let There Be Dust. *Science*, 333:1227–.

Mennella, V. (2010). H Atom Irradiation of Carbon Grains under Simulated Dense Interstellar Medium Conditions: The Evolution of Organics from Diffuse Interstellar Clouds to the Solar System. *ApJ*, 718:867–875.

Mennella, V., Muñoz Caro, G. M., Ruiterkamp, R., Schutte, W. A., Greenberg, J. M., Brucato, J. R., and Colangeli, L. (2001). UV photodestruction of CH bonds and the evolution of the 3.4 mu m feature carrier. II. The case of hydrogenated carbon grains. *A & A*, 367:355–361.

Meyer, D. M., Cardelli, J. A., and Sofia, U. J. (1997). The Abundance of Interstellar Nitrogen. *ApJ*, 490:L103.

Mie, G. (1908). Beitrage zur optik trüber medien speziel kolloidaler metallösungen. *Ann.Phys.*, 25:377.

Miller, A., Lauroesch, J. T., Sofia, U. J., Cartledge, S. I. B., and Meyer, D. M. (2007). Interstellar Iron and Silicon Depletions in Translucent Sight Lines. *ApJ*, 659:441–446.

Mishchenko, M. I. and Travis, L. D. (1994). Light scattering by polydisperse, rotationally symmetric nonspherical particles: linear polarization. *J. Quant. Spectrosc. Radiat. Transfer*, 51:759–778.

Mishchenko, M. I., Wielaard, D. J., and Carlson, B. E. (1997). T-Matrix computations of zenith-enhanced lidar backscatter from horizontally oriented ice plates. *Geophys. Res. Let.*, 24:771–774.

Misselt, K. A., Clayton, G. C., and Gordon, K. D. (1999). A Reanalysis of the Ultraviolet Extinction from Interstellar Dust in the Large Magellanic Cloud. *ApJ*, 515:128–139.

Muñoz Caro, G. M., Jiménez-Escobar, A., Martín-Gago, J. Á., Rogero, C., Atienza, C., Puertas, S., Sobrado, J. M., and Torres-Redondo, J. (2010). New results on thermal and photodesorption of CO ice using the novel InterStellar Astrochemistry Chamber (ISAC). *A & A*, 522:A108.

Mulas, G., Zonca, A., Casu, S., and Cecchi-Pestellini, C. (2013). Modeling Galactic Extinction with Dust and "Real" Polycyclic Aromatic Hydrocarbons. *ApJS*, 207:7.

Murphy, M. T. and Liske, J. (2004). Dust-reddening and gravitational lensing of SDSS QSOs due to foreground damped Lyman α systems. *MNRAS*, 354:L31–L36.

Nelson, A. E., Zaritsky, D., and Cutri, R. M. (1998). A Direct Detection of Dust in the Outer Disks of Nearby Galaxies. *AJ*, 115:2273–2284.

Nieva, M.-F. and Przybilla, N. (2012). Present-day cosmic abundances. A comprehensive study of nearby early B-type stars and implications for stellar and Galactic evolution and interstellar dust models. *A & A*, 539:A143.

Nieva, M.-F. and Simón-Díaz, S. (2011). The chemical composition of the Orion star forming region. III. C, N, Ne, Mg, and Fe abundances in B-type stars revisited. *A& A*, 532:A2.

Noll, S. and Pierini, D. (2005). Dust properties of UV bright galaxies at z ˜ 2. *A & A*, 444:137–155.

Noll, S., Pierini, D., Pannella, M., and Savaglio, S. (2007). Presence of dust with a UV bump in massive, star-forming galaxies at $1 < z < 2.5$. *A & A*, 472:455–469.

Öberg, K. I., Boogert, A. C. A., Pontoppidan, K. M., van den Broek, S., van Dishoeck, E. F., Bottinelli, S., Blake, G. A., and Evans, II, N. J. (2011). The Spitzer Ice Legacy: Ice Evolution from Cores to Protostars. *ApJ*, 740:109.

Paradis, D., Paladini, R., Noriega-Crespo, A., Lagache, G., Kawamura, A., Onishi, T., and Fukui, Y. (2011). Spitzer Characterization of Dust in the Ionized Medium of the Large Magellanic Cloud. *ApJ*, 735:6.

Parneix, P. and Brechignac, P. (1998). Molecular dynamics simulation of the H_2 recombination on a graphite surface. *A & A*, 334:363–375.

Pei, Y. C., Fall, S. M., and Bechtold, J. (1991). Confirmation of dust in damped Lyman-alpha systems. *ApJ*, 378:6–16.

Pendleton, Y. J. and Allamandola, L. J. (2002). The Organic Refractory Material in the Diffuse Interstellar Medium: Mid-Infrared Spectroscopic Constraints. *APJS*, 138:75–98.

Pendleton, Y. J., Sandford, S. A., Allamandola, L. J., Tielens, A. G. G. M., and Sellgren, K. (1994). Near-infrared absorption spectroscopy of interstellar hydrocarbon grains. *ApJ*, 437:683–696.

Penprase, B. E. (1992). Photometric and spectroscopic analysis of high Galactic latitude molecular clouds. I - Distances and extinctions of stars toward 25 selected regions. *The Astrophysical Journal Supplement Series*, 83:273–309.

Press, W. H., Teukolsky, S. A., Wetterling, W. T., and Flannery, B. P. (1992). *Numerical Recipes*. Cambridge: Cambridge Univ. Press.

Radovich, M., Kahanpää, J., and Lemke, D. (2001). Far-infrared mapping of the starburst galaxy NGC 253 with ISOPHOT. *A & A*, 377:73–83.

Rai, R. K. and Rastogi, S. (2010). The scattering and extinction properties of nanodiamonds. *MNRAS*, 401:2722–2728.

Rapacioli, M., Joblin, C., and Boissel, P. (2005). Spectroscopy of polycyclic aromatic hydrocarbons and very small grains in photodissociation regions. *A & A*, 429:193–204.

Roberts, J. F., Rawlings, J. M. C., Viti, S., and Williams, D. A. (2007). Desorption from interstellar ices. *MNRAS*, 382:733–742.

Robertson, J. (1991). Hard amorphous (diamond–like) carbons. *Prog. Solid State Chem.*, 21:199.

Robitaille, T. P. and Whitney, B. A. (2010). The Present-Day Star Formation Rate of the Milky Way Determined from Spitzer-Detected Young Stellar Objects. *ApJ*, 710:L11–L15.

Roche, P. F. (1988). Dust in and towards the Galactic Centre. In Bailey, M. E. and Williams, D. A., editors, *Dust in the Universe*, pages 415–433.

Rodgers, C. D. (2000). *Inverse Methods for Atmospheric Sounding*. Singapore: World Scientific.

Rose, M. E. (1957). *Elementary theory of angular momentum*. John Wiley & Sons, New York.

Rouleau, F. and Martin, P. G. (1991). Shape and clustering effects on the optical properties of amorphous carbon. *ApJ*, 377:526–540.

Sánchez D., N. M. and Parravano, A. (1999). Hierarchical Model for the Evolution of Cloud Complexes. *ApJ*, 510:795–805.

Sandstrom, K. M., Bolatto, A. D., Bot, C., and al. (2012). The Spitzer Spectroscopic Survey of the Small Magellanic Cloud (S^4MC): Probing the Physical State of Polycyclic Aromatic Hydrocarbons in a Low-metallicity Environment. *ApJ*, 744:20.

Sellgren, K. (1984). The near-infrared continuum emission of visual reflection nebulae. *ApJ*, 277:623–633.

Serra Díaz-Cano, L. and Jones, A. P. (2008). Carbonaceous dust in interstellar shock waves: hydrogenated amorphous carbon (a-C:H) vs. graphite. *A & A*, 492:127–133.

Shu, F. H., Shang, H., and Lee, T. (1996). Toward an Astrophysical Theory of Chondrites. *Science*, 271:1545–1552.

Simón-Díaz, S. and Stasińska, G. (2011). The chemical composition of the Orion star forming region. II. Stars, gas, and dust: the abundance discrepancy conundrum. *A & A*, 526:A48.

Sizun, M., Bachellerie, D., Aguillon, F., and Sidis, V. (2010). Investigation of ZPE and temperature effects on the Eley-Rideal recombination of hydrogen atoms on graphene using a multidimensional graphene-H-H potential. *Chem. Phys. Lett.*, 498:32–37.

Snow, T. P. and McCall, B. J. (2006). Diffuse Atomic and Molecular Clouds. *A & A*, 44:367–414.

Snow, T. P. and Witt, A. N. (1995). The Interstellar Carbon Budget and the Role of Carbon in Dust and Large Molecules. *Science*, 270:1455–1460.

Snow, T. P. and Witt, A. N. (1996). Interstellar Depletions Updated: Where All the Atoms Went. *ApJ*, 468:L65.

Sofia, U. J. (2004). Interstellar Abundances and Depletions. In Witt, A. N., Clayton, G. C., and Draine, B. T., editors, *Astrophysics of Dust*, volume 309 of *Astronomical Society of the Pacific Conference Series*, page 393.

Sofia, U. J. and Meyer, D. M. (2001). Interstellar Abundance Standards Revisited. *ApJ*, 554:L221–L224.

Sofia, U. J., Parvathi, V. S., Babu, B. R. S., and Murthy, J. (2011). Determining Interstellar Carbon Abundances from Strong-line Transitions. *AJ*, 141:22.

Soifer, B. T., Neugebauer, G., and Houck, J. R. (1987). The IRAS view of the extragalactic sky. *Ann. Review of A & A*, 25:187–230.

Steglich, M., Bouwman, J., Huisken, F., and Henning, T. (2011). Can Neutral and Ionized Polycyclic Aromatic Hydrocarbons Be Carriers of the Ultraviolet Extinction Bump and the Diffuse Interstellar Bands? *ApJ*, 742:2.

Tielens, A. G. G. M. (2013). The molecular universe. *Reviews of Modern Physics*, 85:1021–1081.

Tomkin, J., Woolf, V. M., Lambert, D. L., and Lemke, M. (1995). Carbon in Field F and G Disk Dwarfs. *AJ*, 109:2204.

Twomey, S. (1977). *Introduction to the Mathematics of the Inversion in Remote Sensing and Indirect Measurements*. New York: Elsevier.

Valencic, L. A., Clayton, G. C., and Gordon, K. D. (2004). Ultraviolet Extinction Properties in the Milky Way. *ApJ*, 616:912–924.

Valencic, L. A., Clayton, G. C., Gordon, K. D., and Smith, T. L. (2003). Small Magellanic Cloud-Type Interstellar Dust in the Milky Way. *ApJ*, 598:369–374.

Valencic, L. A. and Smith, R. K. (2013). Interstellar Abundances toward X Per, Revisited. *ApJ*, 770:22.

van de Hulst, H. C. (1949). *The solid particles in interstellar space.* Utrecht, Drukkerij Schotanus & Jens, 1949.

van de Hulst, H. C. (1957). *Light Scattering by Small Particles.*

van Dishoeck, E. F. (2008). Organic matter in space - An overview. In Kwok, S. and Sanford, S., editors, *IAU Symposium*, volume 251 of *IAU Symposium*, pages 3–16.

Voshchinnikov, N. V. and Henning, T. (2008). Is the silicate emission feature only influenced by grain size? *A & A*, 483:L9–L12.

Waterman, P. C. (1971). Symmetry, unitarity, and geometry in electromagnetic scattering. *Phys. Rev. D*, 3:825–839.

Waxman, E. and Draine, B. T. (2000). Dust Sublimation by Gamma-ray Bursts and Its Implications. *ApJ*, 537:796–802.

Weingartner, J. C. and Draine, B. T. (1999). Interstellar Depletion onto Very Small Dust Grains. *ApJ*, 517:292–298.

Weingartner, J. C. and Draine, B. T. (2001). Dust Grain-Size Distributions and Extinction in the Milky Way, Large Magellanic Cloud, and Small Magellanic Cloud. *ApJ*, 548:296–309.

Welty, D. E., Lauroesch, J. T., Blades, J. C., Hobbs, L. M., and York, D. G. (2001). Unusual Depletions toward the SMC Star SK 155-Differences in Dust Composition in the SMC Interstellar Medium? *ApJ*, 554:L75–L79.

Westley, M. S., Baragiola, R. A., Johnson, R. E., and Baratta, G. A. (1995a). Photodesorption from low-temperature water ice in interstellar and circumsolar grains. *Nature*, 373:405–407.

Westley, M. S., Baragiola, R. A., Johnson, R. E., and Baratta, G. A. (1995b). Ultraviolet photodesorption from water ice. *Planet. Space Sci.*, 43:1311–1315.

Whitford, A. E. (1948). An Extension of the Interstellar Absorption-Curve. *ApJ*, 107:102.

Whittet, D. C. B. (2002). *Dust in the galactic environment (Second edition).* IOP Publishing Bristol and Philadelphia.

Whittet, D. C. B. (2010). Oxygen Depletion in the Interstellar Medium: Implications for Grain Models and the Distribution of Elemental Oxygen. *ApJ*, 710:1009–1016.

Whittet, D. C. B., Shenoy, S. S., Clayton, G. C., and Gordon, K. D. (2004). The Ultraviolet Extinction Curve of Intraclump Dust in Taurus (TMC-1): Constraints on the 2175 Å Bump Absorber. *ApJ*, 602:291–297.

Williams, D. A. (2000). Ashes to ashes, dust to dust. *Astronomy and Geophysics*, 41(3):030000–+.

Witt, A. N. and Gordon, K. D. (2000). Multiple Scattering in Clumpy Media. II. Galactic Environments. *ApJ*, 528:799–816.

Woodall, J., Agúndez, M., Markwick-Kemper, A. J., and Millar, T. J. (2007). The UMIST database for astrochemistry 2006. *A & A*, 466:1197–1204.

Wooden, D. H. (2008). Cometary Refractory Grains: Interstellar and Nebular Sources. *Space Sci. Rev.*, 138:75–108.

Wyatt, P. (1962). Scattering of electromagnetic plane waves from inhomogeneous spherically symmetric objects. *Physical Review*, 127:1837–1843.

Xilouris, E. M., Byun, Y. I., Kylafis, N. D., Paleologou, E. V., and Papamastorakis, J. (1999). Are spiral galaxies optically thin or thick? *A & A*, 344:868–878.

Yang, X. J., Glaser, R., Li, A., and Zhong, J. X. (2013). The Carriers of the Interstellar Unidentified Infrared Emission Features: Constraints from the Interstellar C-H Stretching Features at 3.2-3.5 Micrometers. *ApJ*, 776:110.

York, D. G., Khare, P., Vanden Berk, D., and al. (2006). Average extinction curves and relative abundances for quasi-stellar object absorption-line systems at $1 \leq z_{abs} < 2$. *MNRAS*, 367:945–978.

Zubko, V., Dwek, E., and Arendt, R. G. (2004). Interstellar Dust Models Consistent with Extinction, Emission, and Abundance Constraints. *The Astrophysical Journal Supplement Series*, 152:211–249.

Acknowledgements

First of all I want to thank my supervisor Prof. Cesare Cecchi-Pestellini for his guidance during these three years and allowing me to work on this interesting argument. I thank so much Giacomo Mulas and Silvia Casu for the help and precious advices that they have given to me.

I thank all my office mates at the University and Observatory of Cagliari, particularly Francesco for all the useful computational discussions. Special thanks to my family for giving an important contribution to reach this goal and to Ivana for supporting me at odd times.

I gratefully acknowledge the Sardinia Regional Government for the financial support of my PhD scholarship (P.O.R. Sardegna F.S.E. Operational Programme of the Autonomous Region of Sardinia (Italy), European Social Fund 2007-2013- Axis IV Human Resources, Objective l.3, Line of Activity l.3.1.).